

FLEXIBLE NANO-MEMORY DEVICE BY ZINC OXIDE NANOROD ARRAYS

by

CHAOLONG TANG

JINHUI SONG COMMITTEE CHAIR

SUBHADRA GUPTA

LIN LI

JIALAI WANG

DANEESH SIMIEN

A DISSERTATION

Submitted in partial fulfillment of the requirements  
for the degree of Doctor of Philosophy  
in the Department of Metallurgical and Materials Engineering  
in the Graduate School of  
The University of Alabama

TUSCALOOSA, ALABAMA

2016

Copyright Chaolong Tang 2016  
ALL RIGHTS RESERVED

## ABSTRACT

Memory is one of the key techniques for information technology. It is highly desired to have memory device with flexible characteristic for special applications. The challenges for archiving flexible memory are not only restrained by current materials but also existing memory mechanism, while nanomaterials exhibit size dependent properties that are different from their bulk form, discovering in new materials and architectures design as well as novel working principle provides an alternative approach to meet the objectives.

In this dissertation, a comprehensive study on developing flexible nano-memory device from fundamental semiconducting nanomaterial to device's architecture design and performance is presented. With the strong basis support, the as-fabricated flexible nano-memory device exhibits extraordinary memory characteristics and excellent flexibility.

First, controllable synthesis of zinc oxide (ZnO) nanorod/nanowire (NR/NW) is the prerequisite to provide desired nanomaterials and nanostructures, the effect from substrate roughness is the key to grow well-aligned three-dimensional (3D) ZnO nanostructures for fabricating patterned nano-memory.

Second, because the performance of device is closely related to the material's property, electrical property of one-dimensional (1D) ZnO nanomaterial by experimental and theoretical approaches have been characterized. The results reveal that the electrical resistance has nonlinear length dependence in the single crystal ZnO microbelt/nanobelt (MB/NB), which is significantly different with the bulk counterpart. Finite element simulation can identify the crystallography of the anisotropic semiconducting nanomaterial.

Third, when nanomaterials with a height-diameter ratio in-between zero-dimensional (0D) and 1D, its photoelectric properties will not follow the traditional Ohm's law because of the additional nanoconfinement from the third dimension. Photoelectric property change in half-dimensional (0.5D) ZnO nanomaterials as a function of illumination light intensity and materials geometry has been systematically studied. A new proposed model could more accurately predict the photoelectric characteristics of 0.5D semiconducting nanomaterials.

Last, based on fundamental synthesis and properties characterization above, a new flexible nano-memory device based on ZnO NW arrays is fabricated. Benefited from 3D nanostructures and the unique polar charges screening effect induced electric hysteresis loop memory mechanism, the nano-memory device has outstanding performances in unit down to nanoscale, operation speed up to gigahertz, as well as excellent flexibility.

## DEDICATION

This dissertation is dedicated to my family and friends who support me through my Ph.D. study.

## LIST OF ABBREVIATIONS AND SYMBOLS

ZnO	Zinc oxide
NW	Nanowire
MW	Microwire
NR	Nanorod
MB	Nanobelt
NB	Nanobelt
NT	Nanotube
0D	Zero-dimensional
1D	One-dimensional
0.5D	Half-dimensional
3D	Three-dimensional
AFM	Atomic force microscopy
SEM	Scanning electron microscopy
FESEM	Field emission scanning electron microscope
TEM	Transmitting electron microscopy
HRTEM	High-resolution transmission electron microscopy
SAED	Selected area electron diffraction
C-AFM	Conductive atomic force microscopy
SKPM	Scanning kelvin probe microscopy
CVD	Chemical vapor deposition

FEM	Finite element method
I-V	Current-voltage
ECD	Electrical current density
FDTD	Finite-difference time-domain
HRS	High resistance state
LRS	Low resistance state

## ACKNOWLEDGEMENTS

First, I would like to express my deepest gratitude to my advisor, Dr. Jinhui Song, for his full support, careful guidance and continuous encouragement throughout my graduate studies. I have been amazingly fortunate to be his student and learn so much from him, not only the way to do research, but also the positive attitude to face difficulties in life. His unique perspective on research and sharp insight inspire me to be a professional researcher, his strong will always teaches me to be brave and confident. I do appreciate everything he has done for helping me.

I would also like to thank all of my committee members, Dr. Subhadra Gupta, Dr. Lin Li, Dr. Jialai Wang, Dr. Daneesh Simien, for their time, kind help and all effort for my academic research and dissertation.

I am grateful to all current and prior members in our group: Mr. Chengming Jiang, Mr. Jijie Huang, Dr. Li Sun, Dr. Danfeng Du, Dr. Wenqiang Lu, Mrs. Qihong Wang and Mr. Feng Wang for their help in my research.

I am thankful to the Central Analytical Facility (CAF) staff including Mr. Johnny Goodwin, Mr. Rich Martens and Mr. Robot Holler, for providing the training and giving assistance, and the members of Micro-Fabrication Facility: Dr. Subhadra Gupta and Dr. Alton Highsmith for their help in microfabrication support.

I am also thankful to the all Department of Metallurgical and Materials engineering (MTE) faculty and staff for their help in my research and teaching work, and I would like express the same gratitude to Center for Materials for Information Technology (MINT) for their support in my research.

I would like to acknowledge the financial support from The University of Alabama startup, UA RGC fund of 14484-214281-200 and teaching assistantship from Department of Metallurgical and Materials Engineering.

Last, I am also indebted to my family and friends, who give me tremendous love, encouragement and support in every aspect.

## CONTENTS

ABSTRACT.....	ii
DEDICATION.....	iv
LIST OF ABBREVIATIONS AND SYMBOLS.....	v
ACKNOWLEDGEMENTS.....	vii
LIST OF TABLES.....	xiii
LIST OF FIGURES.....	xiv
CHAPTER 1 INTRODUCTION.....	1
1.1. Motivation.....	1
1.2. Introduction of memory device.....	2
1.3. Basis of ZnO.....	3
1.4. Properties of 1D ZnO nanomaterials.....	5
1.4.1. Optical property.....	5
1.4.2. Basic electrical property.....	6
1.4.3. Common synthesis methodologies.....	7
1.5. Challenge to flexible nano-memory device.....	8
1.5.1. Controllable synthesis.....	8
1.5.2. Electrical properties characterization.....	9
1.5.3. Flexible nano-memory device.....	9
CHAPTER 2 THE ROLE OF SUBSTRATE ROUGHNESS ON ZINC OXIDE NANOWIRE ARRAYS GROWTH BY HYDROTHERMAL APPROACH.....	11
2.1. Introduction.....	11
2.2. Experimental.....	12

2.2.1.	Substrates etching and synthesis of NWs .....	12
2.2.2.	Characterization .....	12
2.3.	Results and discussion .....	13
2.3.1.	Substrates AFM measurement .....	13
2.3.2.	Surface morphology of ZnO NWs.....	14
2.3.3.	Morphology and orientation of ZnO NWs evolution .....	14
2.3.4.	Statistics data analysis.....	15
2.3.5.	Theoretical interpretation.....	17
2.3.6.	Verification experiment .....	19
2.4.	Conclusions.....	19
<b>CHAPTER 3 NONLINEAR LENGTH DEPENDENT ELECTRICAL RESISTANCE OF SINGLE CRYSTAL ZINC OXIDE MICRO/NANOBELT.....</b>		<b>21</b>
3.1.	Introduction.....	21
3.2.	Experiment setting.....	23
3.3.	Results and discussion .....	24
3.3.1.	Crystal structure characterization .....	24
3.3.2.	C-AFM data acquisition.....	25
3.3.3.	Resistance determining .....	27
3.3.4.	Main conduction planes transportation mechanism.....	29
3.3.5.	Verified experiment .....	32
3.3.6.	Additional measurements on other sample with the same growth direction .....	33
3.3.7.	Measurements on ZnO MW/NWs along [0001] growth direction .....	34
3.4.	Conclusions.....	35
<b>CHAPTER 4 PHYSICAL MODEL CONSTRUCTION FOR ELECTRICAL ANISOTROPY OF SINGLE CRYSTAL ZINC OXIDE MICRO/NANOBELT USING FEM .....</b>		<b>36</b>

4.1.	Introduction.....	36
4.2.	Experimental section.....	37
4.3.	Model setup.....	38
4.4.	Results and discussion .....	40
4.4.1.	Electrical isotropy simulation .....	40
4.4.2.	Electrical anisotropy simulation .....	40
4.4.3.	Case study .....	42
4.5.	Conclusions.....	43
CHAPTER 5 PHOTOELECTRIC PROPERTY MODULATION BY NANOCONFINEMENT IN THE LONGITUDE DIRECTION OF SHORT SEMICONDUCTING NANORODS .....		45
5.1.	Introduction.....	45
5.2.	Experimental section.....	46
5.2.1.	Synthesis of 0D, 0.5D and 1D ZnO nanomaterials.....	46
5.2.2.	Characterization of 0D, 0.5D, and 1D nanomaterials.....	47
5.2.3.	Photoelectric property measurements with C-AFM .....	47
5.2.4.	Photoelectric property measurements with SKPM.....	47
5.3.	Results and discussion .....	48
5.3.1.	Measurement setup and materials characterization .....	48
5.3.2.	C-AFM direct I-V acquisition.....	49
5.3.3.	SKPM surface potential mapping .....	52
5.3.4.	Theoretical model propose and interpretation .....	54
5.4.	Conclusions.....	57
CHAPTER 6 PERFORMANCE ENHANCED FLEXIBLE NANO-MEMORY DEVICE .....		59
6.1.	Introduction.....	59
6.2.	Device fabrication .....	60

6.3.	Results and discussion .....	61
6.3.1.	Morphology characterization .....	61
6.3.2.	Memory characteristics .....	62
6.3.3.	Bending test .....	65
6.3.4.	Performance enhanced mechanism.....	66
6.4.	Conclusions.....	69
CHAPTER 7 CONCLUSIONS AND FUTURE WORK.....		70
7.1.	Conclusions.....	70
7.2.	Future work.....	71
REFERENCES .....		73

## LIST OF TABLES

Table 1.1 Physical properties of intrinsic ZnO .....	4
Table 2.1 Substrate Parameters and NW Statistic .....	16

## LIST OF FIGURES

Figure 1.1. (a) Schematic structure of a memory device fabricated using a single ZnO NW/MW. (b) Schematic diagram of a ZnO wire along c-axes direction with polar surfaces on ((0001) surfaces terminated with $Zn^{2+}$ and $O^{2-}$ ions, respectively (c) Typical multicycle I-V curves of the ZnO NW/MW device under an applied sinusoidal voltage signal with amplitude of 1 V at frequency of 100 Hz. Hysteresis loops appear in the forward bias. <sup>7</sup> .....	2
Figure 1.2. (a) Basic structure of flash memory. <sup>8</sup> (b-c) Typical configuration of hard disk drive and magnetic hysteresis loop. <sup>9</sup> .....	3
Figure 1.3. (a) Room temperature photoluminescence spectrum of ZnO NWs. <sup>14</sup> (b) scheme of a NW as a resonance cavity with two naturally faceted hexagonal end faces acting as reflecting mirrors. <sup>15</sup> (c) demonstration of ZnO lasers at room temperature. <sup>16</sup> .....	5
Figure 1.4. (a) Linear current–voltage measurement of a ZnO NW based Ohmic contact (b) diode like current–voltage measurement of a ZnO NW based Schottky contact. <sup>17</sup> .....	6
Figure 1.5. (a) CVD grown ZnO NWs. (b.) Wet chemical grown ZnO NWs.(c) Electrodeposition grown ZnO NWs.(d)Pulse laser deposition grown ZnO NWs. ....	7
Figure 2.1. AFM measurement for six substrates with different roughness (a) $32.0 \text{ nm} \pm 1.6\text{nm}$ , (b) $66.3 \pm 3.3 \text{ nm}$ , (c) $103.9 \pm 5.2 \text{ nm}$ , (d) $221.0 \pm 11.0 \text{ nm}$ , (e) $238.1 \pm 12.0 \text{ nm}$ , and (f) $256.0 \pm 12.8 \text{ nm}$ . ....	13
Figure 2.2. SEM images of the as-grown NW array on substrates presented in Figure 2.1, accordingly. ....	14
Figure 2.3. Schematic diagram demonstrating how morphology and orientation of ZnO NWs evolve with substrate roughness from flat to coarse. ....	15
Figure 2.4. Statistics result of (a) Substrate roughness, (b) Average diameter of NWs, (c) Number density of NWs and (d) Relationship between substrate roughness and induced NW averaged diameter and NW number density. ....	16
Figure 2.5. Verification experiment result. (a) AFM image for the substrate roughness measurement. (b) As-grown NW array characterized by SEM. ....	19
Figure 3.1. The schematic diagram of ZnO MB/NB measurement setting up using C-AFM (the inset photo is the optical image when the AFM tip performs the measurement). ....	23
Figure 3.2. (a) Field emission SEM image of ZnO MB/NB device revealing the flat top surface of the belt laying on nonconductive flat substrate. (b) The part of belt was chosen	

to do TEM measurement (c) HRTEM image of ZnO MB/NB on the area indicated in Figure 3.2(b) (Inserted figure is the diffraction pattern of the sample showing the growth direction is  $[01\bar{1}0]$ ). .....24

Figure 3.3. (a) Topography image obtained through scanning AFM in tapping mode. AFM tip presses the positions, schematically marked by green crosses to acquire I-V curves for different length of the same ZnO MB/NB included between AFM tip and silver electrode. (b) AFM 3D topography of the ZnO MB/NB device revealing the flat surfaces. (c) I-V curves of ZnO MB/NB with different lengths connected in the measuring circuit. Inset is the equivalent circuit of the measurement. ....26

Figure 3.4. The measured resistances of the ZnO MB/NB with different lengths were connected in the measuring circuit. Red curve and black squares are the fitted curve and experimental results of the resistances verses ZnO MB/NB length, respectively. Inset is the scheme of the measurement. ....28

Figure 3.5. The schematic model of the electron transport channel change in the ZnO MB/NB with the length change of the belt between the two electrodes. Stripes are the favorite conducting planes, along which the electrons have much faster moving speed under electric field. (a) Large volume of the conduction planes connected with the electrodes when short length of the ZnO MB/NB is connected within the measuring circuit. (b) Reduced volume of the conduction planes connected with the electrodes when longer length of the ZnO MB/NB is connected within the measuring circuit. (c) All the conduction planes loose contact with the electrodes when the length of the ZnO MB/NB is larger enough, resulting in a sharp increase of the resistance. ....31

Figure 3.6. Crystal structure of the ZnO MB/NB with main conduction planes. ....32

Figure 3.7. I-V curves of ZnO MB/NB measured near the cut off length  $d_0$  ( $d_0 \approx 17.7 \mu\text{m}$ ) from the fixing end, displaying a fast drop of the conductance. ....33

Figure 3.8. C-AFM measurement of ZnO MB/NB.(a) Topography of ZnO MB/NB acquired by AFM in tapping mode;(b) I-V curves of ZnO MB/NB with different lengths connected in the measuring circuit.(c) The measured resistances of the ZnO MB/NB with different lengths were connected in the measuring circuit. ....34

Figure 3.9. C-AFM measurement of ZnO MW/NW.(a) Topography of ZnO MW/NW acquired by AFM in tapping mode; (b) I-V curves of ZnO MW/NW with different lengths connected in the measuring circuit.(c) The measured resistances of the ZnO MW/NW with different lengths were connected in the measuring circuit. ....34

Figure 4.1. (a) C-AFM setup for measuring electrical property of anisotropic ZnO MB/NB with different length connected in the circuit, inserted is the SEM image of ZnO MB/NB with one end covered by silver electrode. (b) The representative I-V characteristic by C-AFM acquisition indicated in Figure 4.1(a). (c) The corresponding length dependent nonlinear electrical resistance of ZnO MB/NB. ....38

Figure 4.2. (a) The scheme of simulation is composed by a ZnO MB/NB grounded and

fixed at its bottom end and along y axis, biased electric potential applied at both ends. (b) The meshed MB/NB model built by Hypermesh software according to the conditions presented in Figure 4.2(a). (c) ECD distribution along y axis for an isotropic ZnO MB/NB in simulation. ....39

Figure 4.3. (a) ECD distribution along y axis for anisotropic ZnO MB/NB. (b) The principle model describing favorite conducting planes of the electron transport channel with larger moving current density has an angle  $\theta$  with electric field along y axis (potential applied on the ZnO MB/NB across top and bottom ends). (c) The corresponding nonlinear length dependent resistance plot. ....42

Figure 4.4. (a) Schematic situation of the conducting planes rotates ( $\pi/2 - \theta$ ) and becomes along z axis while keeping the same applied potential on the both ends. (b) ECD distribution for anisotropic ZnO MB/NB model built in Figure 4.3 after ( $\pi/2 - \theta$ ) rotation along z axis. (c) The corresponding linear length independent resistance plot from simulation. ....43

Figure 5.1. (a) Schematic diagram of C-AFM setup for measuring photoelectric property of ZnO nanomaterials. (b) Low magnification TEM and HRTEM images of the as-synthesized ZnO NRs. (c)-(h) SEM images of ZnO nanomaterials within constant diameter of 100 nm but varied height ranging from 1D to 0D (insets are the corresponding AFM topographies, scale bars are 200 nm). ....49

Figure 5.2. (a) I-V curves of a 0.5D ZnO NR acquired by C-AFM in dark and under light illumination (inserted emission spectrum shows the wavelength of the monochromatic light source used in the measurements and inserted SEM image is the selected ZnO NR with the scale bar of 100 nm). (b) I-V curves for the same NR tested in Figure 5.2(a) upon five different light illumination intensities. (c) Quantitative plot of ZnO nanomaterial photoresponse with height (the third dimensional confinement) upon four different light illuminations acquired by C-AFM. (d) The measured corresponding 3D contour plot of the photo-induced electron density as a function of ZnO nanomaterial height and light illumination intensity. (e) Under 10 V bias, the photoresponse versus illuminating light intensity for a randomly selected 0.5D ZnO nanomaterial showing the photoresponse increases with light intensity till to saturation (scale bar of the inset SEM image is 100 nm). (f) The plots of the saturated photoresponse (left) of ZnO nanomaterial changes with height ranging from 0D to 1D and the corresponding light intensity at current saturation (right). ....51

Figure 5.3. (a) AFM topography of a sample with vertical ZnO nanomaterials ranging from 0D to 1D scanned in non-contact mode. (b)-(c) The corresponding surface potential 2D mappings for vertical ZnO nanomaterials shown in Figure 5.3(a) under light and in dark conditions by SKPM measurement. (d) Scan line profiles for the same sample position from Figure 5.3(a)-3(c) (green line), showing the potential difference of the same ZnO nanomaterial in dark and under illumination. (e) The surface potential plot of ZnO nanomaterials changes with height ranging from 0D to 1D in dark and under light

illumination. (f) The 3D contour plot of the measured photo-induced electron density from surface as a function of ZnO nanomaterial height and light illumination intensity. ....54

Figure 5.4. (a) FDTD simulation of free electron distribution inside a 0.5D ZnO nanomaterial upon light illumination of 20 mW/cm<sup>2</sup> based on classical theory. (b) The corresponding 3D contour plot of photo-induced electron density as a function of the light illumination intensity and the ZnO nanomaterial height based on classical theory. (c) The calculated corresponding 3D contour plot of the photo-induced electron density from surface as a function of ZnO nanomaterial height and light illumination intensity. (d) FDTD simulated free electron distribution of a 0.5D ZnO nanomaterial under light illumination of 20 mW/cm<sup>2</sup> by the new model with quantum corrections. (e) The calculated corresponding 3D contour plot of photo-induced electron density of ZnO nanomaterial as a function of light illumination intensity and the material height by the new model with quantum corrections. (f) The calculated corresponding 3D contour plot of photo-induced electron density from surface of ZnO nanomaterial as a function of light intensity and the material height by the new model. ....57

Figure 6.1. (a) Schematic diagram of the architecture design of the flexible nano-memory device. (b) The illustration of the device under compressive bending. (c) The illustration of the device under tensile bending. ....61

Figure 6.2. (a) SEM images of the ZnO NR arrays grown on the flexible substrate (right lower inset is the optical image). (b) SEM images of the top morphology of the as-fabricated device. (c) Optical image of gold topped nano-memory device (scale bar is 5 μm). ....62

Figure.6.3. Memory characteristics of the flexible nano-memory device. (a) Typical I-V curve of the device plotted on a semilogarithmic scale. (b) The band diagram of the nano-memory unit showing an asymmetric Schottky-semiconductor- Ohmic contact. (c) Write-read-erase cycles of the nano-memory device. The top and bottom curves are the applied voltage and the corresponding current response, respectively. The ON-state ('write') has been induced by -5 V, while the OFF-state ('erase') has been reinstated by 5 V. Between switching the states ('read') have been probed by device current under 2 V. (d) Endurance characteristics of the nano-memory device during 100 repeated cycles with the readout voltage is 2 V. (e) Time retention test of the nano-memory device on the plastic substrate. (f) Cumulative probability of current state distributions from 50 different units. ....64

Figure 6.4 (a) Photograph of the device in bending and unbending states on a bending stage machine. (b) "ON" and "OFF" state currents as a function of curvature radius. The data is collected from I-V curves performed at each curvature radius. (c) "ON" and "OFF" currents as a function of bending cycles. Bending radius of 10 mm is utilized. The data is collected from I-V curves performed at each bending cycles. ....66

Figure 6.5. (a) Crystal structure of wurtzite ZnO. The top end with Zn<sup>2+</sup> ion layer attracting free electrons. Lower part is the digital circuit of flexible nano-memory unit. (b) Illustration of device under bending and related volumetric strain distribution of the device by COMSOL Multiphysics. (c) schematic diagram of device after bending, causing a slight

increase of electric field in nano-memory unit by COMSOL Multiphysics simulation after bend. (d) Calculation of corresponding I-V curves before and after bending, showing a little bit larger hysteresis loop after bend. ....68

## CHAPTER 1 INTRODUCTION

### 1.1. Motivation

As all known, data storage is an important and decisive element for information technology. We always want to store our information like music, documents or any other data in a large storage medium like hard disk drive, flash drive with very fast storing speed. In addition, those memory devices are desired to be as small as possible. However, though storage devices have greatly evolved for few decades, they are still behind people desire. This reality may be mainly caused by lacking breakthroughs both in finding new materials and in designing novel storing architectures.

With the advent of nanotechnology and nanomaterials for several decades, people now are able to design new electronic devices with enhanced performance via the novel properties of nanomaterials, stemming from the extraordinary large surface area-to-volume ratios and quantum effect.<sup>1-4</sup> Nevertheless, there have very few reports on memory devices development using this new technique recently.<sup>5,6</sup> Herein, it is urgent and important to develop nano-memory devices with high performance based on this sense.

Our previous publication Song *et al.*<sup>7</sup> revealed that a nonsymmetrical, Schottky-Ohmic contacted ZnO NW/MW can serve as a memristor if the channel length is short and the applied frequency is high (see Figure 1.1(a)). The electrical hysteresis loop as shown in Figure 1.1(c) arises from screening model of the polar charges at the two ends of the ZnO NW (see Figure 1.1(b)). This novel phenomenon indicates a new nanoscale memory technique that could have high dense memory capacity and fast writing/erasing data storage speed.

Since this is only a tentative experiment and discovery of new phenomenon, study of building semiconducting NR arrays to construct applicable nanoscale memory device is highly anticipated. Thus, it is desired to systematically study 1D ZnO nanomaterials first, which will be the main component of nano-memory device, and then to build high performance nanoscale memory device using vertical ZnO NR as the 3D memory unit with very-high density and ultra-fast operating speed. More than that, it is also highly desired to have memory device with flexible characteristic for special applications like robots, implantable intellectual system, biosensing system, etc. It is possible that flexible memory could be realized by unique nanodevices based on nanomaterials and architectures design as well as novel working principle.

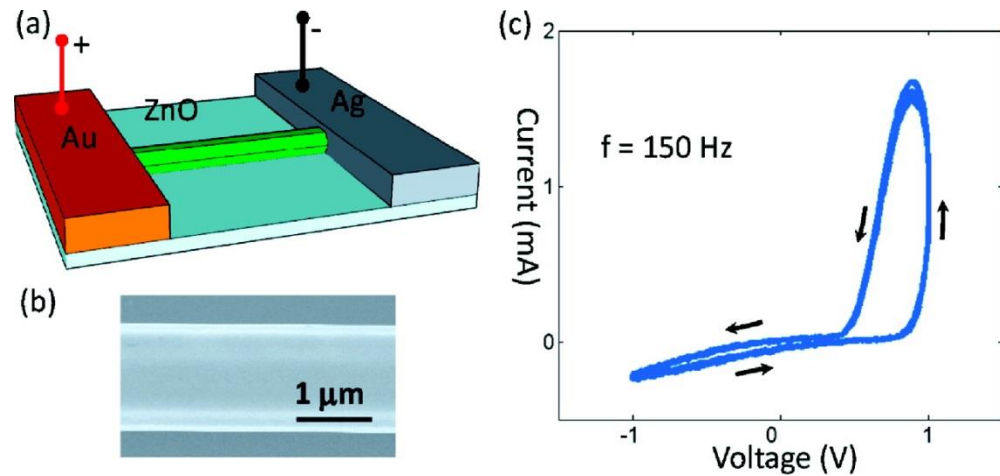


**Figure 1.1.** (a) Schematic structure of a memory device fabricated using a single ZnO NW/MW. (b) Schematic diagram of a ZnO wire along c-axes direction with polar surfaces on ((0001) surfaces terminated with Zn<sup>2+</sup> and O<sup>2-</sup> ions, respectively (c) Typical multicycle I-V curves of the ZnO NW/MW device under an applied sinusoidal voltage signal with amplitude of 1 V at frequency of 100 Hz. Hysteresis loops appear in the forward bias.<sup>7</sup>

## 1.2. Introduction of memory device

General speaking, memory device is referred to a computer components or recording media related technical storage device to retain digital data. Currently, the most commonly used data storage technologies are semiconductor, magnetic, and optical. To be specific, flash memory is an example of non-volatile semiconductor based memory device that has a semiconductor chip

containing millions of the tiny transistors or capacitors. Its basic structure is shown in Figure 1.4(a); another example of main memory device is hard disk drive (see Figure 1.4(b)) which uses different patterns of magnetization on a magnetically coated surface to store information, the typical behavior of this magnetic material is hysteresis loop as shown in Figure 1.4(c).

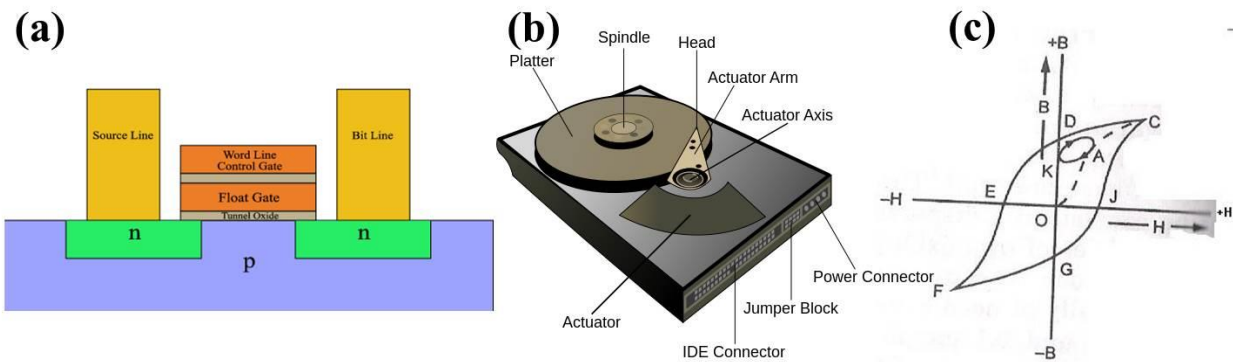


**Figure 1.2.** (a) Basic structure of flash memory.<sup>8</sup> (b-c) Typical configuration of hard disk drive and magnetic hysteresis loop.<sup>9</sup>

### 1.3. Basis of ZnO

As a direct wide bandgap semiconductor material, ZnO is well known for its applications in semiconducting industry and academic research for its nanostructures. The typical crystal structure of ZnO is hexagonal wurtzite which is the most stable structure in ambient. The hexagonal structure of ZnO has a space group of  $P6_3mc$  with the lattice constants  $a=0.325$  nm and  $c=0.52$  nm. ZnO is a strong piezoelectric material from its polar property, resulting from Zn and O atoms which have opposite charges in the different stacking plane. Usually, the total charge of the bulk ZnO is neutralized but the top layer of ZnO surface could be singly uncoupled and hence has electrical charge.

**Table 1.1** Physical properties of intrinsic ZnO

Property	Value
Lattice parameters (T=300 K)	
$a_0$	0.32495 nm
$c_0$	0.52069 nm
Density	5.606 g/cm <sup>3</sup>
Stable phase at 300 K	Wurtzite
Melting point	2248 K
Relative dielectric constant	8.656
Refractive index	2.008, 2.029
Gap energy	3.4 eV, direct
Intrinsic carrier concentration	$<10^6 \text{ cm}^{-3}$
Exciton binding energy	60 meV
Electron effective mass	0.24
Electron mobility( T= 300 K)	200 cm <sup>2</sup> /V s
Hole effective mass	0.59
Hole mobility (T= 300 K)	5-50 cm <sup>2</sup> /V s

Table 1.1 summarized the basic physical properties of ZnO.<sup>10</sup> The intrinsic ZnO is an n-type semiconductor with a direct band gap of 3.37 eV, carrier concentration is less than  $10^6 \text{ cm}^{-3}$ . Besides, the electronic structure of ZnO is very important for its mechanical, electrical, and optical properties. As can be seen in Table1, the electron effective mass is 0.24 and mobility at room temperature is 200 cm<sup>2</sup>/V s, hole effective mass is 0.59 and hole mobility at room

temperature is  $5\text{-}50\text{ cm}^2/\text{V s}$ . These properties are helpful to semiconductor device fabrication and can be explained by semiconductor physics.

#### 1.4. Properties of 1D ZnO nanomaterials

##### 1.4.1. Optical property

As showing in Figure 1.3(a), there are usually two emission bands for the photoluminescence spectrum of ZnO if excited by a UV laser at room temperature. One is the dominant UV emission peak at around 380 nm, coming from the near-band-edge emission through exciton-exciton collision processes.<sup>11</sup> The other is in at about 500 nm, which is attributed to the electron-hole recombination at a deep level caused by intrinsic point defects and surface defects.<sup>12</sup> Furthermore, an unexpected emission at around 760 nm is presumably from the second order feature of UV band-edge emission.<sup>13</sup>

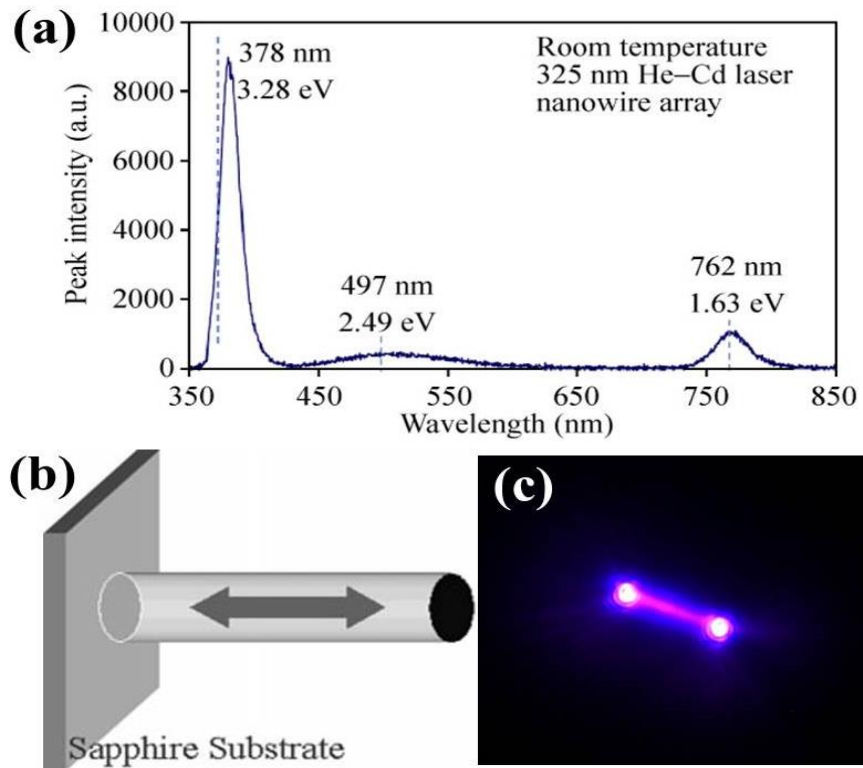


**Figure 1.3.** (a) Room temperature photoluminescence spectrum of ZnO NWs.<sup>14</sup> (b) scheme of a NW as a resonance cavity with two naturally faceted hexagonal end faces acting as reflecting mirrors.<sup>15</sup> (c) demonstration of ZnO lasers at room temperature.<sup>16</sup>

While ZnO has a large exciton binding energy of 60 meV which can provide an efficient excitonic recombination for lasing, and each single NW in NW arrays has two end facets with high reflective to form a Fabry-Perot cavity (see Figure 1.3(b), thus ZnO NW arrays are good materials for the fabrication of room temperature lasers as shown in Figure1.3(c).

#### 1.4.2. Basic electrical property

As we know, the intrinsic 1D ZnO nanomaterial is natural n type semiconductor, when it is contacted with metal electrodes; either Ohmic contact or Schottky contact will be formed. The Ohmic contact is a non-rectifying junction, which means it has a linear I-V curve as showing in Figure 1.4(a). while a Schottky contact means having a large barrier height which is the difference of metal work function and electron affinity, and it shows diode like rectifying I-V curve as shown in Figure 1.4(b).<sup>17</sup> However, for example, sometimes the contact between Au (5.1 eV) and ZnO (4.5 eV) is supposed to be Schottky contact but it is Ohmic due to the imperfect defect states at interface in fabrication. Moreover, Field effect transistors based on a single ZnO NW<sup>18</sup> or ZnO NW thin films<sup>19</sup> have been fabricated for use in optically transparent mechanically flexible electronics.<sup>20</sup>

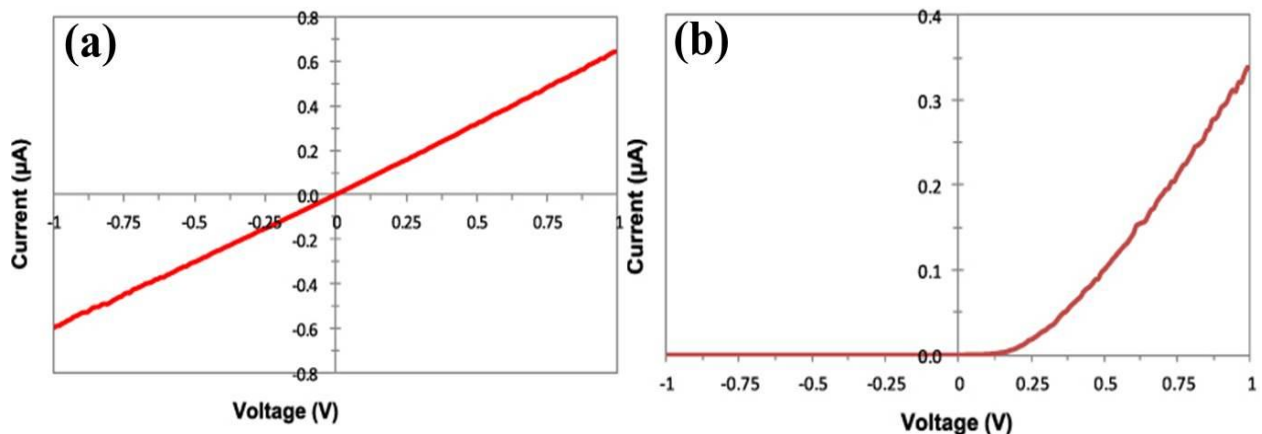


**Figure 1.4.** (a) Linear current–voltage measurement of a ZnO NW based Ohmic contact (b) diode like current–voltage measurement of a ZnO NW based Schottky contact.<sup>17</sup>

### 1.4.3. Common synthesis methodologies

From the first day of appearing nanomaterials, people are dedicating in nanomaterials and nanostructures synthesis via a variety of approaches.<sup>21, 22</sup> As to 1D semiconducting ZnO nanomaterial, researchers have developed many kinds of methods to obtain their desired products.<sup>23, 24</sup> Typically, all methodologies can be classified as physical method and chemical method, and latter is often used in large-scale synthesis and very popular nowadays. There are two main techniques to synthesize 1D ZnO nanostructures: physical method and chemical method. In detail, a wide range of synthesis approaches have been developed to grow 1D ZnO nanomaterials, such as CVD<sup>25</sup> (see Figure 1.5(a)), wet chemical methods<sup>26</sup>, electrodeposition<sup>27</sup> (see Figure 1.5(b)), physical vapor deposition<sup>28</sup>, molecular beam epitaxy<sup>29</sup>, pulsed laser deposition<sup>30</sup> (see Figure 1.5(d)). Among those techniques, physical methods usually require high

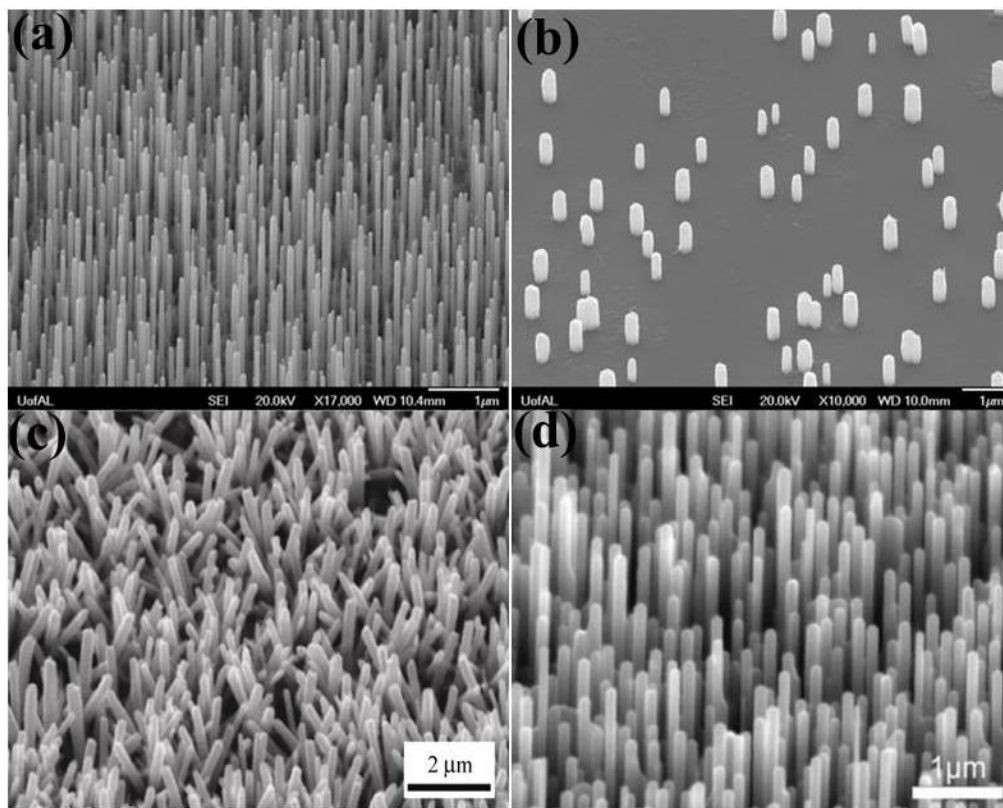


**Figure 1.5.** (a) CVD grown ZnO NWs. (b.) Wet chemical grown ZnO NWs.(c) Electrodeposition grown ZnO NWs.(d)Pulse laser deposition grown ZnO NWs.

temperature, but can provide relatively high crystal quality; chemical methods especially wet chemical method are very attractive for its low cost, green synthesis, relatively low temperature, easy operation and large scale yield products. Most important, it is controllable by tuning growth parameters to obtain desired morphologies and properties of the final products, which is becoming the first choice technique in 1D ZnO nanomaterials growth. Herein, synthesis strategy in this work is wet chemical methods.

#### 1.5. Challenge to flexible nano-memory device

The objective is to elucidate a novel technique termed flexible nano-memory device which is based on 1D ZnO NR arrays with excellent performance in high dense memory capacity, fast reading/writing storage speed and ultra-flexibility. Although we have some understanding about synthesis strategies and fundamental properties of 1D semiconducting ZnO nanomaterials, possible memory mechanism, some basic knowledge from materials to fabricate the device are still unclear.

##### 1.5.1. Controllable synthesis

By taking advantage of chemical method, we use wet chemical synthesis to synthesize the component nanomaterials for nano-memory device. Although this is a well-developed technique and many parameters such as growth temperature, precursor concentration, solution PH value and substrate to control growth 1D ZnO nanomaterials have been well researched<sup>31-33</sup>, the effect from substrate roughness is still unknown. The controllable synthesis required to reveal the influence from this key factor to grow well aligned 1D ZnO nanostructures, which is the prerequisite for creating high performance devices.

### 1.5.2. Electrical properties characterization

It is well known that the resistance of a bulk semiconductor material is linearly dependent on its length according to Ohm's law, but some recent works reveal that nanostructured materials may not obey this classic rule.<sup>34, 35</sup> For example, A. N. Andriotis *et al.*<sup>34</sup> revealed that the nonlinear length dependence of electrical transport in single-walled carbon NTs was abnormal, which is an intrinsic feature of the carbon NTs. As to the anisotropic 1D ZnO nanomaterials, there is no research describing the similar investigation from its intrinsic feature. Undoubtedly, obtaining the basic conductive property of the functional single crystal semiconducting nanomaterials is the essential basis for further functional nanodevice design and improving its performance.<sup>14, 36</sup> As to proposed nano-memory device, its performance is mainly depending on I-V switch characterization, well known the basic electrical anisotropy can predict and manipulate the performance.

Besides, our recent publication demonstrated that when nanomaterials with a height-diameter ratio in between 0D and 1D, its photoelectric properties do not follow the traditional ohm's law because of the additional nanoconfinement from the third dimension.<sup>37</sup> The proposed nano-memory device needed to understand both the size induced effect and illumination light intensity influence on wet chemical grown 1D ZnO nanostructure and related physical properties changes.

### 1.5.3. Flexible nano-memory device

Because the final objective is to develop novel flexible nano-memory device, it must be possessing high dense storage capacity, ultra-fast operation speed and persistent flexibility. The unique 3D nanostructures design will enable the smallest physical storage unit comparing to current planar techniques in industry. our recently work revealed a memory mechanism that 1D ZnO nanomaterial with polar charges can induce electric hysteresis loop and Schottky contacts

has the response frequency up to gigahertz in theory, and the publications induced the feasibility of fabricating electronic devices on flexible substrates.<sup>7</sup> However, with the full support of all these possible prerequisite studies there are still several issues needed to be solved including what size of 1D ZnO nanomaterials can produce good hysteresis loop, how to make patterned 1D ZnO nanomaterials on flexible substrate, how to characterize the flexible nano-memory device's performance to demonstrate its excellence, etc. Relied on the prerequisite research and challenge analysis above, it is promising that novel flexible nano-memory device can be fabricated with superior performances and advantages comparing to the current technology.

## CHAPTER 2 THE ROLE OF SUBSTRATE ROUGHNESS ON ZINC OXIDE NANOWIRE ARRAYS GROWTH BY HYDROTHERMAL APPROACH

### 2.1. Introduction

Over decades, ZnO nanomaterial has attracted intensive research interest due to its unique mechanical, electrical, chemical and optical properties.<sup>3, 38-41</sup> As a wide band gap semiconductor, ZnO has various forms in nanostructures like nanoparticles<sup>42</sup>, nanoplatelets<sup>43</sup>, NRs<sup>44</sup>, NWs<sup>45</sup>, NTs<sup>46</sup>, peculiar nanocastles<sup>47</sup>, nanoforests<sup>48</sup>, and more, among which ZnO NWs attract special attentions in optoelectronics, sensor applications, and nanogenerators.<sup>7, 49, 50</sup> Since ZnO NWs can be grown on different substrates, such as inorganic<sup>51</sup>, organic<sup>52</sup>, crystalline<sup>53</sup> and organometallic<sup>54</sup> by physical vapor deposition<sup>55</sup>, CVD<sup>56</sup>, hydrothermal deposition<sup>57</sup>, pulse laser deposition<sup>58</sup>, and so on. Many unique properties and applications of ZnO NWs depend on the NW diameter, number density or total grown area. It is much more desirable to well control the size, orientation, and density of the NWs for device application. There are some studies on controllable synthesis of ZnO NWs. For instance, the average diameter of ZnO NWs grown by CVD method can be controlled by changing the oxygen flow rate and hence the Zn vapor supersaturation.<sup>59, 60</sup> Yang *et al.* found that ZnO NWs' position, orientation, diameter, and density could be controlled by epitaxial substrate, the positions of the NWs can be controlled by the initial positions of Au catalyst and the NW areal density can be controlled by modifying the thickness of Au catalyst.<sup>15</sup> Song *et al.* found that both the partial pressure of O<sub>2</sub> and total system pressure had distinct effects on the final morphologies of ZnO nanostructures.<sup>61</sup> There are some literatures reporting the study of catalyst effects.<sup>62-64</sup> As to substrate roughness effects on ZnO

NW arrays growth, there are few literatures reported. However, ZnO NWs growth heavily depends on substrate roughness and such kind of nanostructures also have extensive application in nanodevice fabrication.<sup>65, 66</sup> Besides, comparing with other common used synthesis methods, hydrothermal approach takes advantages of lower temperature, easier operation, lower cost, larger-scale production and more controllability.<sup>67</sup> Thus, it is urgent and extremely important to understand how substrate roughness in hydrothermal synthesis correlates to the ZnO NWs growth results. In this chapter, we report a detailed investigation on how the diameter and number density of ZnO NW array grown by hydrothermal approach vary with substrate roughness. This work was published in *Acta Metallurgica Sinica (English Letters)* 2016, 29, 237-242.<sup>68</sup>

## 2.2. Experimental

### 2.2.1. Substrates etching and synthesis of NWs

Six identical silicon substrates were etched by a mixture solution of 0.4M sodium hydroxide and 26.3 mL Isopropyl alcohol at 80 °C for different time.<sup>69</sup> Small pyramids were formed on the silicon surface as a result of anisotropy of wet chemical etching process.<sup>70</sup> Following the general procedure to grow ZnO NWs on the as-etched silicon substrates via hydrothermal method<sup>71</sup>, a 5 nm thick ZnO seed layer was firstly sputtered on all six substrates under the same conditions. 0.05M hexamethylenetetramine solution was mixed with 0.05M Zinc nitrate hexahydrate in solution at ratio of 1:1 in a beaker. Then seed layer surfaces of substrates were floated facing down on the 85 °C liquid solution for 45 minutes.

### 2.2.2. Characterization

We measured the surface roughness of the as-etched substrates before ZnO NWs growth by using AFM (Park Systems XE-70) in non-contact mode. AFM cantilever is ANSCM-PA

(Appnano) with resonance frequency of 300 kHz. FESEM (JEOL 7000) was employed to characterize the morphology of the as-grown ZnO NWs.

## 2.3. Results and discussion

### 2.3.1. Substrates AFM measurement

The morphologies of the six substrates with different roughness are shown in Figure 2.1. The average roughness of the six substrate surfaces is measured to be (a)  $32.0 \text{ nm} \pm 1.6 \text{ nm}$ , (b)  $66.3 \pm 3.3 \text{ nm}$ , (c)  $103.9 \pm 5.2 \text{ nm}$ , (d)  $221.0 \pm 11.0 \text{ nm}$ , (e)  $238.1 \pm 12.0 \text{ nm}$ , and (f)  $256.0 \pm 12.8 \text{ nm}$ , respectively. Substrate roughness was obtained by three times measurements on every substrate with randomly selected area of  $30 \text{ }\mu\text{m} \times 30 \text{ }\mu\text{m}$  and the statistical measurement significantly reduced error caused by the none perfect sample uniformity. An extremely thin ZnO seed layer was deposited on all etched substrates for facilitating ZnO NWs growth<sup>59</sup>; other the other hand, since our etched samples have relatively high roughness from about 32 nm to 256 nm compared to 5 nm thickness ZnO thin film coverage, the influence from this intermediate can be reasonably ignored.

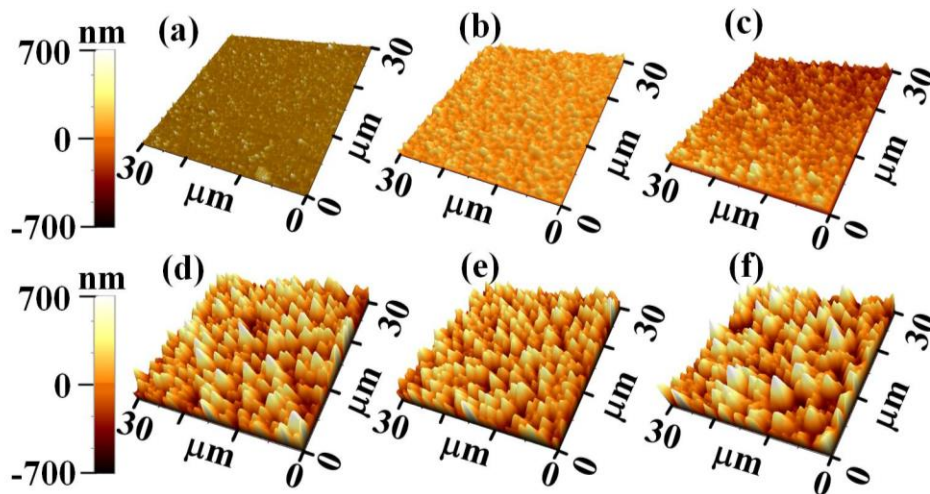


**Figure 2.1.** AFM measurement for six substrates with different roughness (a)  $32.0 \text{ nm} \pm 1.6 \text{ nm}$ , (b)  $66.3 \pm 3.3 \text{ nm}$ , (c)  $103.9 \pm 5.2 \text{ nm}$ , (d)  $221.0 \pm 11.0 \text{ nm}$ , (e)  $238.1 \pm 12.0 \text{ nm}$ , and (f)  $256.0 \pm 12.8 \text{ nm}$ .

### 2.3.2. Surface morphology of ZnO NWs

Figure 2.2 shows the surface morphology of all six samples in an area of  $1,500\text{ nm} \times 1,135\text{ nm}$ , exhibiting the clear hexagonal shape of ZnO NWs with wurtzite structure and demonstrating a variation of the morphology upon increasing substrate roughness also.

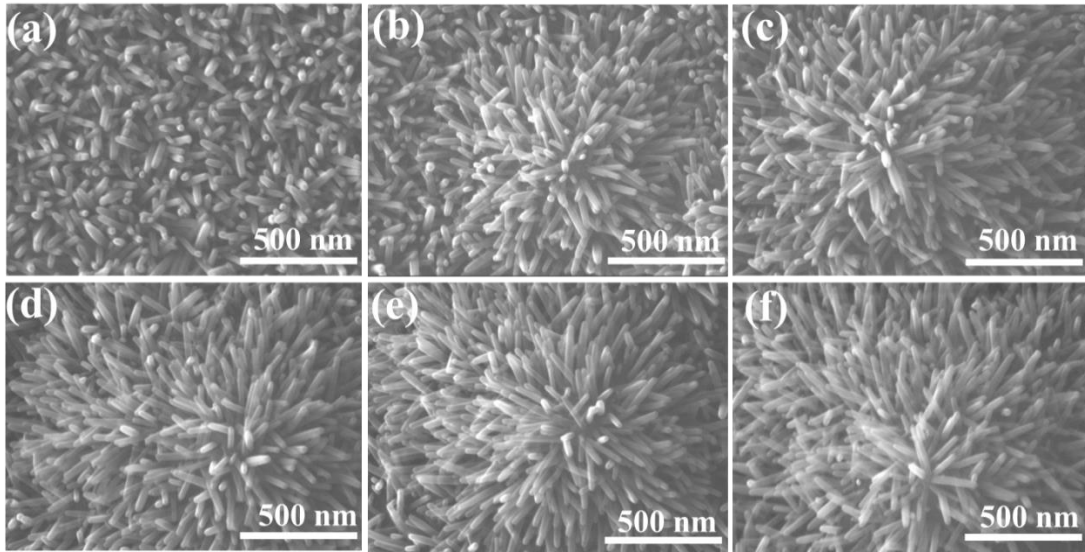


**Figure 2.2.** SEM images of the as-grown NW array on substrates presented in Figure 2.1, accordingly.

### 2.3.3. Morphology and orientation of ZnO NWs evolution

The interpretative schematic diagram in Figure 2.3 demonstrates the growth evolution- how the morphology and orientation of NWs changes with increasing substrate roughness. It can be observed that morphology of NWs varies distinctly from almost vertical alignment to flower-like along with the roughness increase. In addition, despite of the difference of substrate roughness, all individual NWs are approximately perpendicular to the surface of substrate rather than in vertical direction.

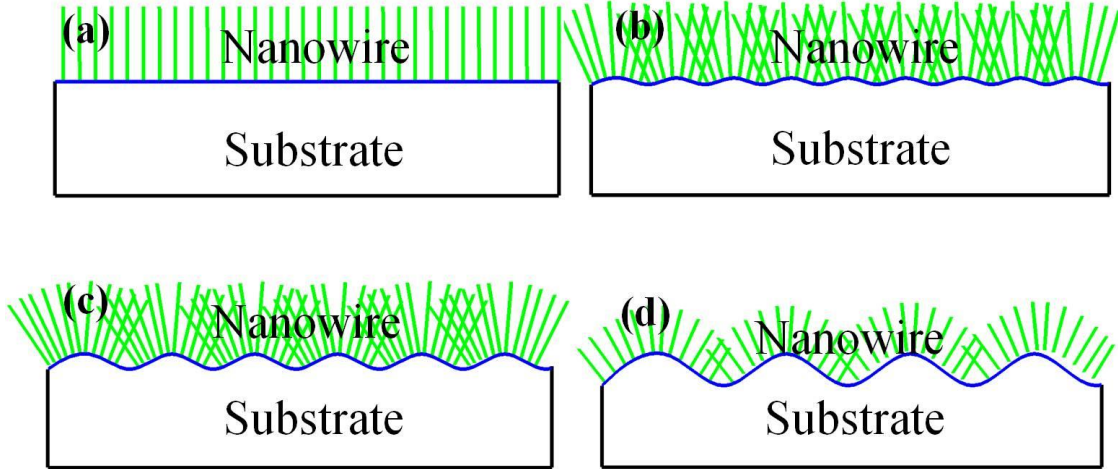


**Figure 2.3.** Schematic diagram demonstrating how morphology and orientation of ZnO NWs evolve with substrate roughness from flat to coarse.

#### 2.3.4. Statistics data analysis

In order to statistically analyze the average diameter of NWs and number density of NWs, we used the statistical software named Nano measurer with high accuracy to analyze all six samples based on their top view SEM images with the same magnification and pixel size. Figure 2.4(a) plots the roughness distribution among those samples. It can be seen that the average diameter with standard deviation about 13% decreased slightly with the increase of substrate roughness, so did the number density of NWs with standard deviation about 6%, which is the number of NWs in the specific area as shown in Figure 2.2. The average diameter of NWs for six samples varied from 29.1 nm to 32.8 nm and the number density ranged between 290.3 per  $\mu\text{m}^2$  and 352.3 per  $\mu\text{m}^2$  as shown in Figure 2.4(b) and 4(c). Moreover, as shown in Figure 2.4(d), both NW averaged diameter and NW number density decrease with the growing roughness. All statistics data are summarized in Table 2.1.

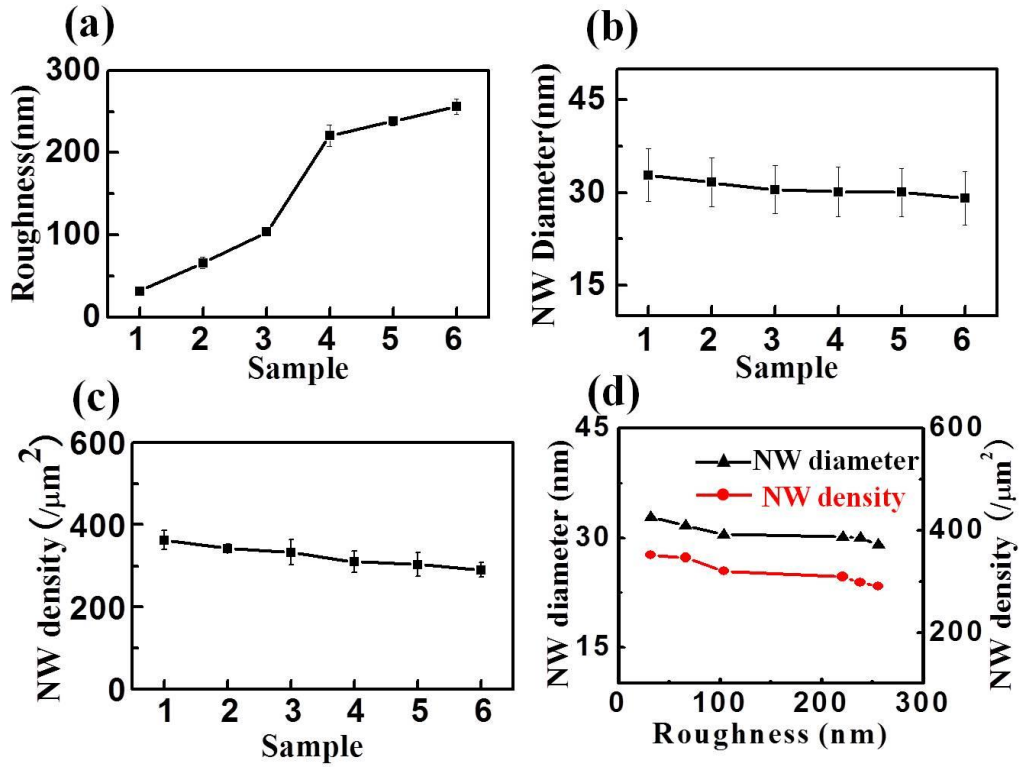


**Figure 2.4.** Statistics result of (a) Substrate roughness, (b) Average diameter of NWs, (c) Number density of NWs and (d) Relationship between substrate roughness and induced NW averaged diameter and NW number density.

**Table 2.1** Substrate Parameters and NW Statistic Results

Sample	Substrate	NW Average	NW Number Density
	Roughness (nm)	Diameter (nm)	(/ $\mu\text{m}^2$ )
1	32.0	32.8	352.3
2	66.3	31.6	346.7
3	103.9	30.5	320.4
4	221.0	30.1	309.0
5	238.1	30.0	298.3
6	256.0	29.1	290.3

### 2.3.5. Theoretical interpretation

In order to explain the experimental result, the classic nucleation theory was developed to study the relationship between substrate roughness and average diameter, number density of the NWs. Referring to Wenzel model<sup>72</sup>, we can define the roughness factor  $r$  as the ratio of the surface area  $S_r$  of a factual rough substrate to a smooth substrate with surface area  $S_0$  based on the fact that the surface area  $S_r$  of a factual rough substrate increases with its surface roughness value. So the roughness factor  $r$  of a factual substrate surface can be written as:

$$r = S_r/S_0 \quad (2.1)$$

Furthermore, since the intrinsic contact angle  $\theta$  is designated by the wetting angle of solution on the smooth surface, wetting angle  $\theta^*$  of rough interface can be expressed as<sup>73</sup>

$$\cos \theta^* = \frac{r(\sigma_{CL} - \sigma_{CS})}{\sigma_{SL}} = r \cos \theta \quad (2.2)$$

Where,  $\sigma_{CL}$ ,  $\sigma_{CS}$  and  $\sigma_{SL}$  are the specific crystal/liquid interface energy, crystal/substrate interface energy, and substrate/liquid interface energy, respectively.

According to Equation (2.2), wetting angle of rough surface will decrease along with the increasing roughness factor if the initial contact angle on flat substrate is less than  $90^\circ$ . While in real chemical reaction, the initial nucleation happens on interface of solution droplet and substrate, and the water contact angle was measured to be about  $38^\circ$  on freshly sputtered ZnO seed layers on Si substrate.<sup>74</sup> Thus, we can reasonably assume an expression of surface free energy with roughness factor by using classic Young's equation<sup>75</sup>

$$\Delta\gamma_s = \gamma_{SV} - \gamma_{SL} = \gamma_{LV} \cos \theta^* = \gamma_{LV} r \cos \theta \quad (2.3)$$

Here  $\gamma_{SV}$ ,  $\gamma_{SL}$ , and  $\gamma_{LV}$  indicate the solid-vapor, the solid-liquid, and the liquid-vapor interfaces energy, respectively.

According to nucleation theory, nucleation density has the following equation<sup>76</sup>

$$N = A \exp(-\Delta G^*/RT) \quad (2.4)$$

where  $N$  is nucleation density,  $\Delta G^*$  is activation energy of nucleation, which contains volume free energy  $\Delta G_V$  and surface free energy  $\Delta G_S$  or  $\Delta \gamma_s$ ,  $T$  is growth temperature, and  $A$  is a constant. Therefore, we can combine equation (2.3) and (2.4) together and achieve an expression of nucleation density which is linked to surface roughness or surface free energy as:

$$N = A \exp(-\Delta G^*/RT) = A \exp[-(\Delta G_V + \Delta \gamma_s)/RT] = A \exp[-(\Delta G_V + \gamma_{LV} r \cos \theta)/RT] \quad (2.5)$$

It is noticeable that increased roughness factor  $r$  will firstly increase the Gibbs free energy change ( $\Delta G^*$ ) by increasing free surface energy and then decrease the probability of nucleation sites density, which results in diminishing of NW number density. From the statistical analysis of the ZnO NWs sample synthesized with different substrate roughness (See Table 2.1), when substrate roughness linearly increased from 32.0 nm to 256 nm, NW number density accordingly decreased from 352.3 ( / $\mu\text{m}^2$  ) to 290.3( / $\mu\text{m}^2$  ), which is in accordance with equation (2.5). Meanwhile, based on literature that quantitatively describes controllable diameter of ZnO NW growth from classical nucleation theory, the diameter of ZnO NW in this experiment can be written as<sup>59</sup>

$$d = \frac{-4\gamma_{LV} \sin \theta^*}{\Delta G_V} = \frac{-4\gamma_{LV}}{\Delta G_V} [1 - (r \cos \theta)^2]^{\frac{1}{2}} \quad (2.6)$$

Although the sizes of ZnO NW synthesized by wet chemical method are strongly dependent on  $[\text{Zn}^{2+}]$  concentration<sup>77</sup>, the effect from substrate roughness is still distinguishable. From equation (6), we can infer that the diameter of ZnO NW will be slightly and reversely proportional to the substrate roughness, which matches well with our experimental observations that sizes of ZnO

NWs drop from about 33 nm down to about 29 nm proportionally with the increase of substrate roughness.

### 2.3.6. Verification experiment

Finally, the control experiments were carried out to verify the statistic result and the deduced mechanism. Figure 2.5(a) is the 3D morphology of AFM measurement on the new etched substrate, displaying the substrate roughness is 221.0 nm. Figure 2.5(b) shows the SEM image of the ZnO NWs grown on this substrate. Through statistical analysis, the NW number density is 310.8 ( $/\mu\text{m}^2$ ) and the averaged diameter is 30.1 nm, correspondingly, which closes to its expected position in the linear lines of statistic data in Figure 2.4. Thus, it is possible to control the density and diameter through adjusting substrate roughness.

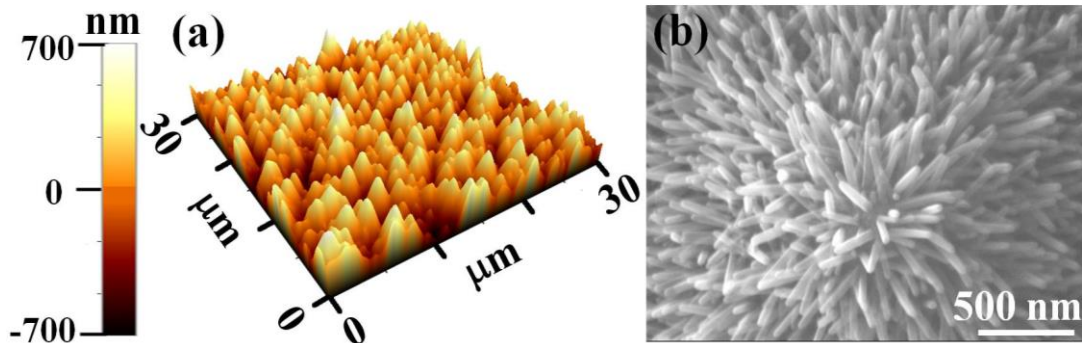


**Figure 2.5.** Verification experiment result. (a) AFM image for the substrate roughness measurement. (b) As-grown NW array characterized by SEM.

### 2.4. Conclusions

This work systematically investigated substrate roughness effect on the morphology of ZnO NW arrays grown via hydrothermal method. Six etched silicon substrates with different roughness were purposely prepared for growing ZnO NW arrays. The substrate roughness and the as-grown NW samples were characterized by AFM and SEM, correspondingly. Statistical analysis on the data shows that average NW diameter and number density of ZnO NW arrays are

inverse proportional to the increase of substrate roughness. In order to interpret this result, two equations to describe number density-roughness, average diameter-roughness based on classic theory of nucleation and the Gibbs adsorption equation were successfully deduced, respectively. The verifying experiments demonstrated the accuracy of deduced mechanism involving substrate roughness in NW nucleation growth. Those revealed findings are important for understanding the key role of substrate roughness in NW growth and to further help to well control the growth of ZnO NWs for high performance nanodevices.

## CHAPTER 3 NONLINEAR LENGTH DEPENDENT ELECTRICAL RESISTANCE OF SINGLE CRYSTAL ZINC OXIDE MICRO/NANOBELT

### 3.1. Introduction

As the wide and direct band gap ( $E_g = 3.35$  eV) semiconductor, one-dimensional ZnO MWs/NWs and MBs/NBs have been widely used to fabricate electrical devices like nanogenerators, field effect transistors, gated diodes, gas sensing devices, and memory storage device, etc.<sup>78-83</sup> Apparently, these applications severely rely on the fundamental electrical properties of the build blocks in microscales and nanoscales<sup>84-87</sup>, which is extremely important for both understanding the basic properties for materials in that size and improving the design and efficiency of the devices composed of them. It is well known that the resistance of bulk semiconductor material is linearly dependent on its length according Ohm's law, but some recent works reveal that nanostructured materials may not obey this classic rule. For example, Antonis N. Andriotis *et al.*<sup>34</sup> revealed that the length dependence of electrical transport in single-wall carbon NTs was abnormal. The nonlinear resistance as a function of the NT length obtained in their calculations and experimental findings confirmed it was an intrinsic feature of the carbon NTs. As to the ZnO NWs, there is no publication to describe corresponding investigation in depth. Almost all the related publications focused on the I-V characteristics of semiconductor nanostructures instead of the deep mechanism on the length dependence.<sup>88, 89</sup> Undoubtedly, Obtaining the basic conductive property of the functional single crystal semiconducting NW/NB is the essential basis for further functional nanodevice design and improving its performance.<sup>14, 36</sup>

In short, it is highly interesting and necessary to investigate whether the exceptional intrinsic electrical property lies in the 1D single crystal semiconducting ZnO micro/nanostructures.

Up to present, people have measured the electrical resistance and resistivity of single semiconductor NW/NB by using TEM-scanning tunneling microscope<sup>87</sup>, four terminal methods<sup>35</sup>, and probe station combined with I-V measurement system<sup>88</sup>, etc. All of them require using the complicated microelectronic manufacture techniques and specially designed equipment to perform the measurement. Recently, with the development of multifunctional AFM, it is more convenient to perform in situ measurement of electrical<sup>90</sup>, magnetic<sup>91</sup>, and piezoelectric<sup>92</sup> properties of nanomaterials in the atmosphere environment. Li *et al.*<sup>93</sup> reported that the transverse I-V characteristic of ZnO MB was carried out under elastic loads by using Pt-coated AFM tip and that the transverse electrical conductivity varied with different mechanical elastic loads from AFM tip was stemmed from the electron depletion zone induced by local piezoelectric effect on the ZnO single crystal belt.

In this chapter, we report the length dependent electrical resistance property characterization of a single crystal ZnO MB/NB using C-AFM technique and the proposed mechanism based on the crystal structure analysis. The quantitative characterization on the relationship between resistance and MB/NB length was acquired by measuring the resistance of the belt between conductive AFM tip and the fixing electrode. The measured result reveals that the electrical resistance of ZnO MB/NB is exponential to its length rather than the linear dependence as Ohm's law predicated. The proposed mechanism and further confirmative measurements verify that the nonlinear resistance-length curve of ZnO MB/NB is associated with anisotropic electron speed in the different crystal lattice planes stacked inside the single crystal belt. This work was published in *Phys. Chem. Chem. Phys.* 2013, 15, 8222-8227.<sup>3</sup>

### 3.2. Experiment setting

The experiment setup is schematically shown in Figure 3.1. An intrinsic silicon wafer was first coated with a thin layer of silicon oxide as insulating layer and one end of the single crystal ZnO MB/NB synthesized by CVD approach<sup>28,94</sup> then was mounted on the substrate with silver paste, which also served as an electrode for next step electrical characterization. The Pt coated conductive AFM tip, which also acted as another electrode, scanned the MB/NB surface in tapping mode to obtain the topography image to locate the MB/NB and then to acquire I-V curves at different length as the points indicated in Figure 3.1. The inset shows the optical microscopy image of the measurement process captured when conductive AFM tip acquired the I-V curve on the ZnO MB/NB. The crystal structure of the ZnO MB/NB was examined by a JEOL 7000 SEM at 20 kV high accelerating voltage. The TEM image of a single ZnO MB/NB was recorded on a TECNAI F20 with an accelerating voltage of 200 kV.

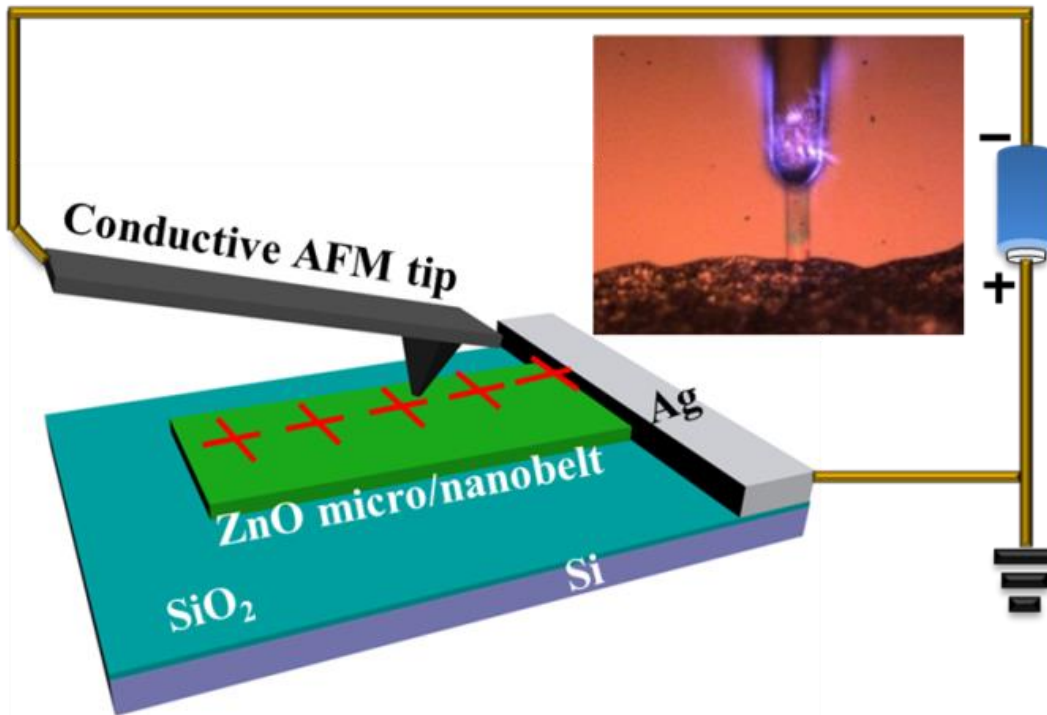


**Figure 3.1.** The schematic diagram of ZnO MB/NB measurement setting up using C-AFM (the inset photo is the optical image when the AFM tip performs the measurement).

### 3.3. Results and discussion

#### 3.3.1. Crystal structure characterization

Figure 3.2(a) shows that the ZnO MB/NB has a regular shape and one end is fixed on the nonconductive substrate by silver paste. In our experiment, the relatively large size of the belt was chosen to perform the characterization for the sake of easy manipulation to fabricate measurable device. The HRTEM of the selected area in the Figure 3.2(b) shows the inter planer spacing of 0.28 nm between two adjacent  $(10\bar{1}0)$  planes of ZnO MB/NB in Figure 3.2(c). After further analyzing its SAED pattern (the inset of Figure 3.2(c)) in  $[0001]$  electron beam direction, which is a typical hexagon close packed pattern, we can confirm that the ZnO MB/NB is a single crystal with wurtzite hexagonal structure and the preferred growth direction is  $[01\bar{1}0]$  rather than along the c-axis  $[0001]$  direction of most ZnO MB/NB.<sup>95-99</sup>

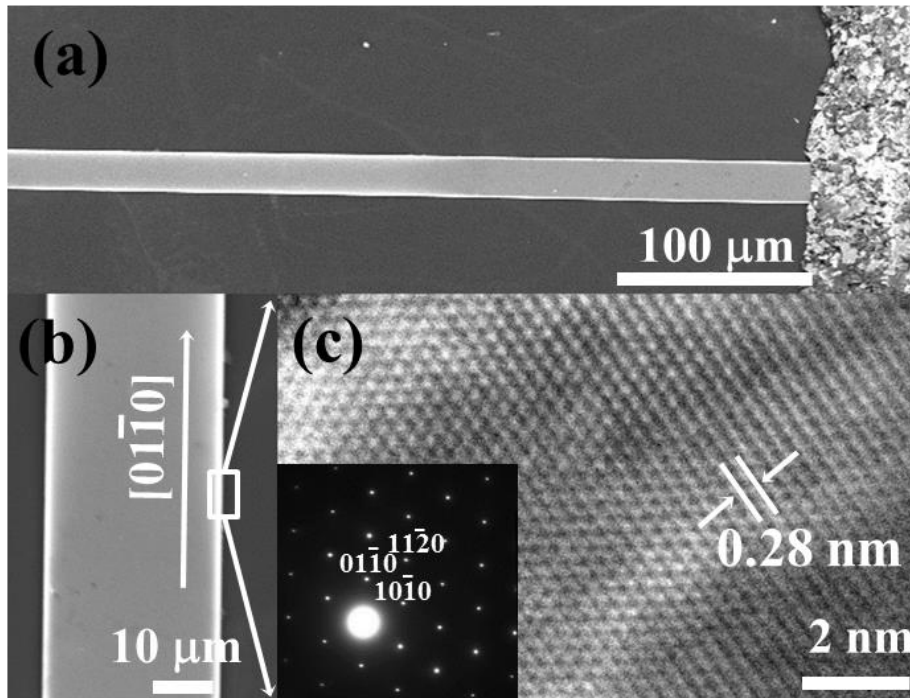


**Figure 3.2.** (a) Field emission SEM image of ZnO MB/NB device revealing the flat top surface of the belt laying on nonconductive flat substrate. (b) The part of belt was chosen to do TEM measurement (c) HRTEM image of ZnO MB/NB on the area indicated in Figure 3.2(b) (Inserted figure is the diffraction pattern of the sample showing the growth direction is  $[01\bar{1}0]$ ).

### 3.3.2. C-AFM data acquisition

Figure 3.3(b) is the 3D ZnO MB/NB topography image which was obtained by scanning AFM in tapping mode, illustrating that it is about 30  $\mu\text{m}$  wide and 1.5  $\mu\text{m}$  thick. The surface of the sample appeared to be very flat. Physical contact was established between the MB/NB top surface and Pt AFM conductive tip through AFM contact mode, allowing a close electrical circuit configuration to perform I-V curve measurements. Furthermore, tip loading position can be directly selected on the ZnO MB/NB topographical image, which is a convenient feature of the AFM. A constant normal force was kept for every measurement to minimize system error. Figure 3.3(c) shows a series of I-V curves under the reversed bias according to the positions schematically marked with crosses in Figure 3.3(a), which started from the interface of the MB/NB and the fixed electrode toward to the free end of the belt. The colored curves in Figure 3.3(c) are the corresponding I-V curves acquired through the same belt with different length connected in the measuring circuit. All the I-V curves show asymmetry rectifying shape and the forward bias is negative potential relative to the ground indicated in Figure 3.1. Moreover, the conductance decreases as the length of the MB/NB increases. However, there is no direct conclusion that can be drawn from these curves and the quantificational relationship between the resistance of a single crystal MB/NB and its length requires further investigation by processing the measured data mathematically. The asymmetry rectifying shape I-V curve is because of the ZnO MB/NB based device possesses a metal-semiconductor-metal structure which has a resistor composed of semiconducting belt and Schottky contact formed by the Pt AFM tip and ZnO MB/NB. On the other end of the MB/NB, the contact between silver paste and ZnO MB/NB is Ohmic<sup>100</sup> and the resistance is small enough to be reasonably neglected. The equivalent circuit of this measurement system is shown in the inset of Figure 3.3(c). From the I-V curves acquired by

this design, the typical rectifying nonlinear I-V characteristic<sup>101</sup> is obvious due to the dominating value of the Schottky barrier comparing with the resistance of the ZnO MB/NB. Since the resistance of Schottky contact is identical during all the acquisitions of the I-V curves with different length of the same ZnO MB/NB included in the measuring circuit (see the following deduction), the electrical resistance of the MB/NB itself can be derived from the total resistance in the circuit by subtracting the Schottky barrier which is the measured resistance when the conductive AFM tip acquires I-V curve on the MB/NB with zero length included.

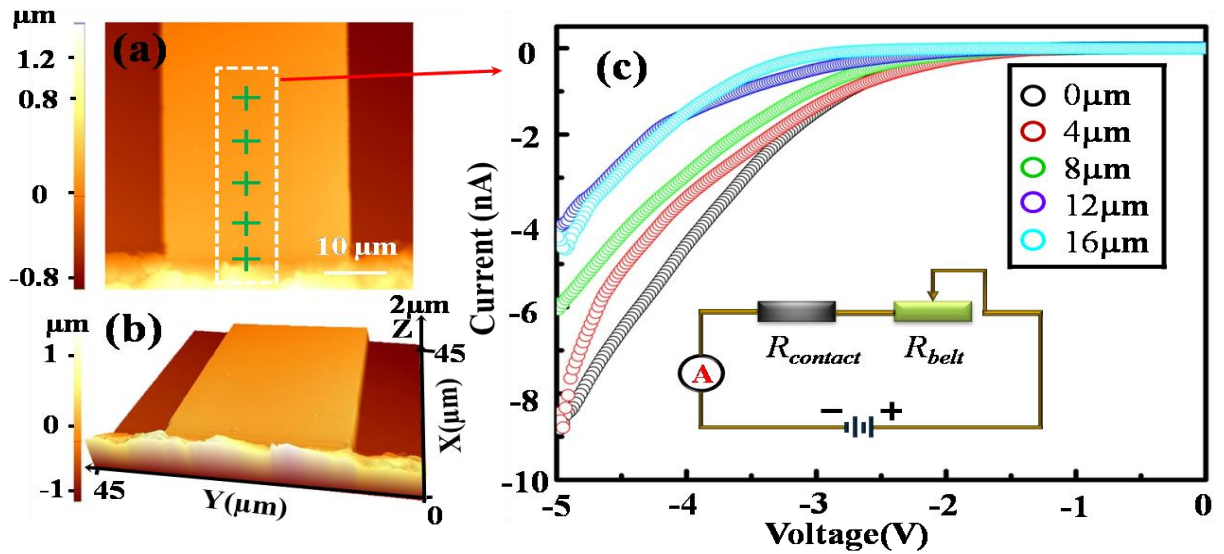


**Figure 3.3.** (a) Topography image obtained through scanning AFM in tapping mode. AFM tip presses the positions, schematically marked by green crosses to acquire I-V curves for different length of the same ZnO MB/NB included between AFM tip and silver electrode. (b) AFM 3D topography of the ZnO MB/NB device revealing the flat surfaces. (c) I-V curves of ZnO MB/NB with different lengths connected in the measuring circuit. Inset is the equivalent circuit of the measurement.

As the equivalent circuit in the inset of Figure 3.3(c) indicated, the total electrical resistance of the circuit is the sum of Schottky contact resistance ( $R_{contact}$ ) and the resistance of the ZnO MB/NB ( $R_{belt}$ ), thus the total potential can be expressed as

$$V = V_{contact} + V_{belt} = (R_{contact} + R_{belt})I \quad (3.1)$$

$V$  is the applied voltage and  $I$  is the corresponding current in the circuit. For a Schottky contact the current density ( $J_s$ ) governed by thermionic emission over the barrier is given by<sup>102</sup>

$$J_s = A^* T^2 \exp\left(-\frac{2\phi_B}{KT}\right) \left[\exp\left(\frac{qV}{KT}\right) - 1\right] \quad (3.2)$$

Where  $A^*$  is Richardson's constant,  $\phi_B$  is the Schottky barrier height,  $T$  is temperature,  $K$  is Boltzmann constant,  $q$  is the electron charge,  $V$  is the applied voltage. The Schottky contact resistivity ( $\rho_C$ ) and resistance ( $R_{contact}$ ) can be calculated by the following two equations

$$\rho_C = \lim_{V \rightarrow 0} \left( \frac{dV_{contact}}{dJ} \right) = \frac{KT}{qJ_s} \quad (3.3)$$

$$R_{contact} = \frac{\rho_C}{A} = \lim_{V \rightarrow 0} \frac{KT}{qJ_s A} \quad (3.4)$$

Here  $J$  is the current density in the circuit,  $A$  is the Schottky contact area and  $V$  is the applied voltage. The Schottky contact resistance can be obtained by calculating the limitation value of  $\rho_C$ , so the electrical resistance of Schottky contact can be regarded as constant in all I-V curves acquiring processes for that its values will not change during the measurements.

### 3.3.3. Resistance determining

According to the analysis above, the electrical resistance of the belt verses its length can be derived by subtracting the constant Schottky contact resistance as the dot plots shown in Figure 3.4. The resistances are corresponding to the various lengths of the ZnO MB/NB connected in the measuring circuit as the green part of the ZnO MB/NB between AFM tip and electrode in the inset of Figure 3.4. By fitting the discrete ZnO MB/NB resistances ( $R_d$ ) with lengths ( $d$ ), an exponential curve with equation coefficients ( $a_1 = -0.5268$ ,  $a_2 = 0.3577$ ) could be obtained as shown in Figure 3.4 and expressed by

$$R_d = a_1 \exp(a_2 \times d) \quad (3.5)$$

The experimental data obviously shows ZnO MB/NB electrical resistance exponentially increases with its length, which is significantly different from the linear length independent resistance of bulk counterpart. In order to know the basic physics under the resistance of single crystal ZnO MB/NB, we expanded the exponential equation (3.5), which was obtained based on the experimental measurement, into polynomials and equation (3.6), the resistance ( $R_d$ ) of the single crystal ZnO MB/NB with measuring length ( $d$ ), could be rewritten as

$$R_d = \frac{0.9625 \times d}{1 - 0.0565 \times d} \quad (3.6)$$

From equation (3.6), the electrical behavior of this ZnO MB/NB is significantly different from the classic Ohm's law that the resistance of semiconductor is linear to its length.

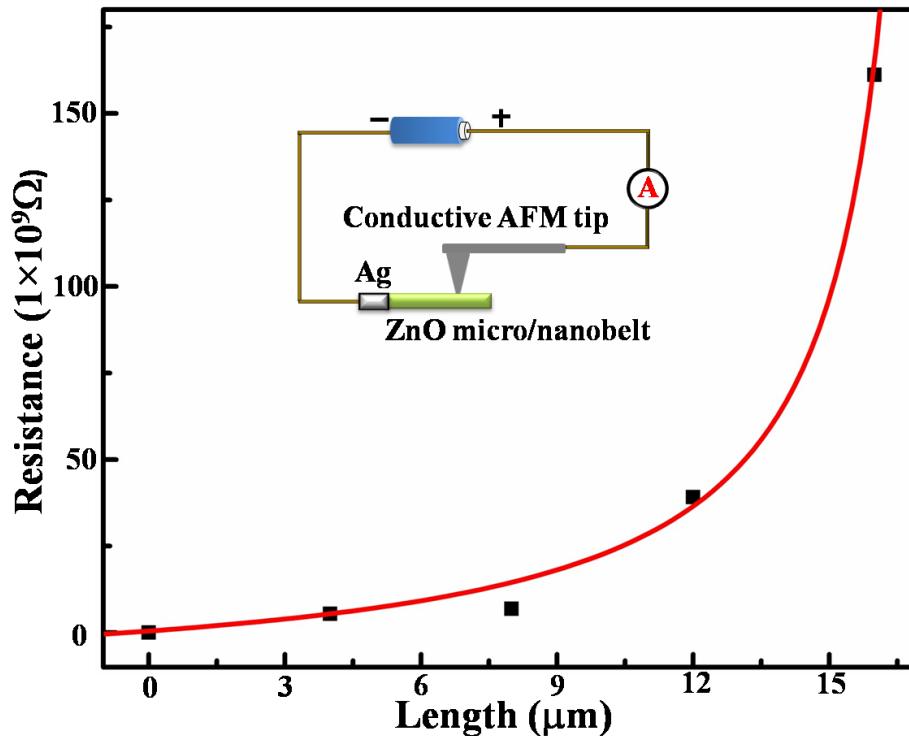


**Figure 3.4.** The measured resistances of the ZnO MB/NB with different lengths were connected in the measuring circuit. Red curve and black squares are the fitted curve and experimental results of the resistances versus ZnO MB/NB length, respectively. Inset is the scheme of the measurement.

### 3.3.4. Main conduction planes transportation mechanism

Normally, resistance comes from the impedance to the electrons that run through the materials under electrical field. In order to understand the detailed electrons transport process inside the MB/NB belt, we propose a model based on the crystal structure of the single crystal ZnO MB/NB to interpret its nonlinear length dependent resistance. Owing that the contributions to total electrical resistance from Schottky contacts keep constant and have no influence on the length dependent I-V curves acquisition, the affective factors leading to the non-linear electrical resistance must be from the intrinsic characteristic of MB/NB. Besides, Lee *et al.*<sup>103</sup> reported that the electrical conductivity along the  $ab$  plane ( $\sigma_{ab}$ ) was higher than that along the  $c$  axis ( $\sigma_c$ ) for the  $\text{CuAlO}_2$  crystal with structural anisotropy ( $\sigma_{ab} \geq 25\sigma_c$ ). Based on the anisotropic structure of ZnO single crystal, the similar crystal planes with much higher electrical conductivity rather than along the growth direction are expected to exist in ZnO MB/NB. Hence we can reasonably assume that electrons in ZnO MB/NB are mainly transported along these higher conduction lattice planes. If the electrical conductivity along the planes, which have an angle to the longitudinal direction of the MB/NB, is much larger than that of the planes parallel to the longitudinal direction, the overall conductivity of the MB/NB will mainly rely on the conductivity along the planes with highest conductivity. As shown in Figure 3.5(a), these main conduction planes inside ZnO MB/NB are not perpendicular or parallel to the longitudinal axis of ZnO MB/NB but with an angle of  $\frac{\pi}{2} - \theta$ , as the inclined strips indicated in the schematic

Figure 3.5. Electrons inside this belt have preferred crystal planes as transport path which has a much higher conducting capability than other directions, resulting that the electrons move to the anode along within these main conducting crystal planes (restricted in a small thickness less than the inter plane distance) under an longitudinal direction electrical field. Thus, the electron

carriers mostly run through the main conduction planes. Based on this understanding, the effective electrical resistance of the ZnO MB/NB can be simply inferred out by a geometrical approach as indicated in Figure 3.5(b):

$$R_d = \rho \times \frac{l}{s} = \frac{2 \times \rho_{ZnO}}{\sin 2\theta \times w \times h} \times \frac{d}{\left(1 - \frac{d}{w \times \tan \theta}\right)} \quad (3.7)$$

Where  $\rho$ ,  $s$  and  $l$  is the resistivity, cross section area and length of a given ZnO MB/NB respectively from the classic Pouillet's law.  $\rho_{ZnO}$  is the resistivity of ZnO MB/NB,  $w$  stands for the width,  $d$  represents the length,  $h$  is the thickness, and  $\theta$  is the complementary angle of main conduction planes with the longitude direction of the ZnO MB/NB. Comparing the equation (3.7) deduced from the model of electric conductivity of anisotropy lattice planes with equation (3.6), which is obtained from the experimental data, they are highly identified in term of

$\frac{c_1 \times d}{1 - c_2 \times d}$ , where  $c_1$  and  $c_2$  are constant coefficients for both expressions. By comparing equation

(3.7) obtained from the theoretical model with equation (6), the experimental deduction, we can get  $\theta = 30^\circ$  which is corresponding to  $(11\bar{2}0)$ ,  $(\bar{1}\bar{1}20)$ ,  $(\bar{1}2\bar{1}0)$ ,  $(1\bar{2}10)$  planes in ZnO MB/NB with  $\rho = 174 \Omega \cdot \text{cm}$ .  $(11\bar{2}0)$  and  $(\bar{1}\bar{1}20)$  planes are the stripes described in Figure 3.5 and  $(\bar{1}2\bar{1}0)$ ,  $(1\bar{2}10)$  planes are the mirror image of stripes in the belt which are also satisfied with our model, according to the crystal structure analysis in Figure 3.2. The detailed crystal model is shown in Figure 3.6.

With increasing the length of the MB/NB, the resistance will increase exponentially. When the length of the MB/NB connected in the circuit is very short, all the main conduction planes are connected with the electrodes (as indicated by the gold lines in Figure 3.5(a)), resulting in a good conductance. As the length of the ZnO MB/NB increases along the longitude direction, some of

the main conduction planes become losing connections with the electrodes and the conducting channel becomes narrow as indicated in Figure 3.5(b). When the length of the ZnO MB/NB is increased too long enough for all the main conduction planes lost connections with the electrodes, as shown in Figure 3.5(c), the resistance increases abruptly. The resistance of the single crystal ZnO NB/NB not only relies on the length of the main conduction plane but also the number of them, which are connected within the measurement circuit. In brief, the resistance of the single crystal ZnO NB/MB exponentially increases with the length due to the anisotropic high conduction lattice planes, in contrary to the linear Ohm's law in classic physics.

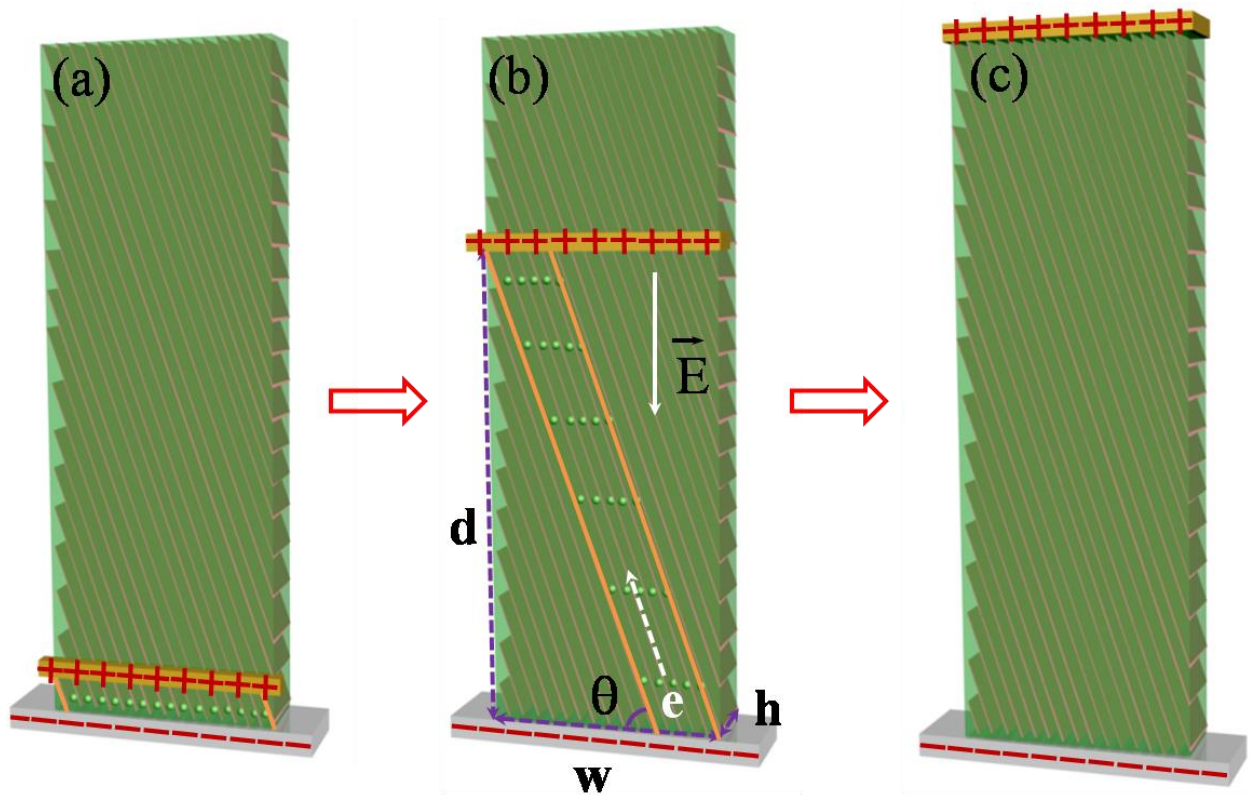


**Figure 3.5.** The schematic model of the electron transport channel change in the ZnO MB/NB with the length change of the belt between the two electrodes. Stripes are the favorite conducting planes, along which the electrons have much faster moving speed under electric field. (a) Large volume of the conduction planes connected with the electrodes when short length of the ZnO MB/NB is connected within the measuring circuit. (b) Reduced volume of the conduction planes connected with the electrodes when longer length of the ZnO MB/NB is connected within the measuring circuit. (c) All the conduction planes loose contact with the electrodes when the length of the ZnO MB/NB is larger enough, resulting in a sharp increase of the resistance.

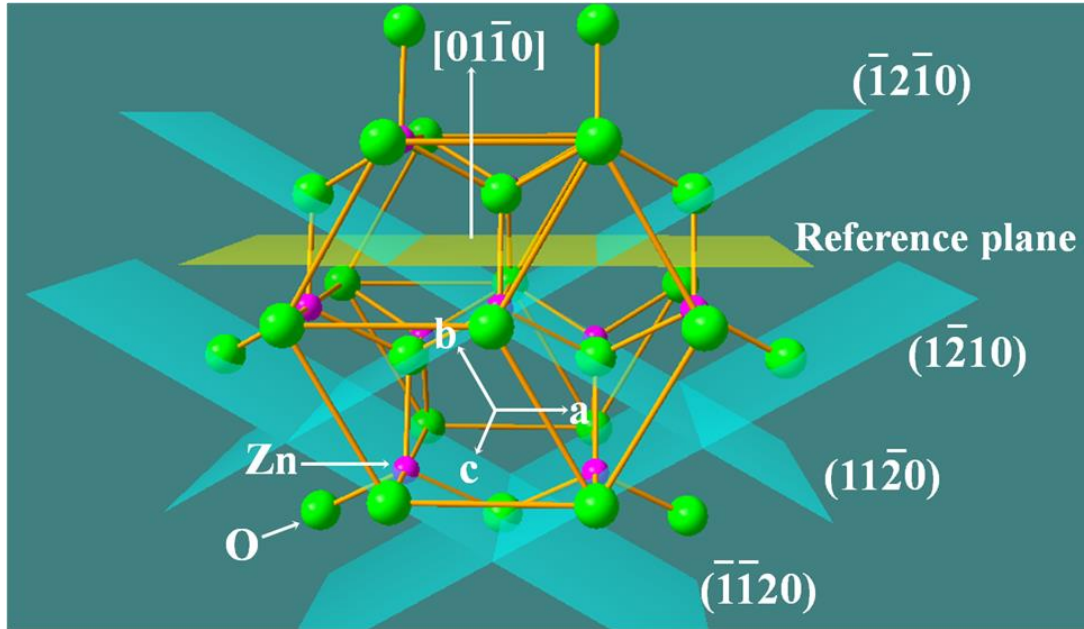


**Figure 3.6.** Crystal structure of the ZnO MB/NB with main conduction planes.

### 3.3.5. Verified experiment

Furthermore, from the schematic figures in Figure 3.5, there is a conductance cut off length, beyond which all the main conduction planes lose contact with the electrodes and carrier electrons have no fast transport path, resulting in an inflexion point in the resistance-length curve. On the other hand, based on the theoretical equation (3.7), a cut off length is calculated to be about  $17.5 \mu\text{m}$  for a ZnO MB with a width of  $30 \mu\text{m}$ . Proof experiments have been carried by acquiring I-V curves on the positions covered the cut off length and the corresponding I-V curves are shown in Figure 3.7. From the slopes of the I-V curves, we could clearly tell the resistance increase with the length. When the length of the ZnO MB reaches cut off length of about  $17.7\mu\text{m}$ , the resistance tends to be extremely large as shown by the pink I-V curve in Figure 3.7, indicating all the main conduction planes lost connections with the electrodes. Those measurements further prove the conduction plane model proposed in the report for the single crystal ZnO NB/MB.

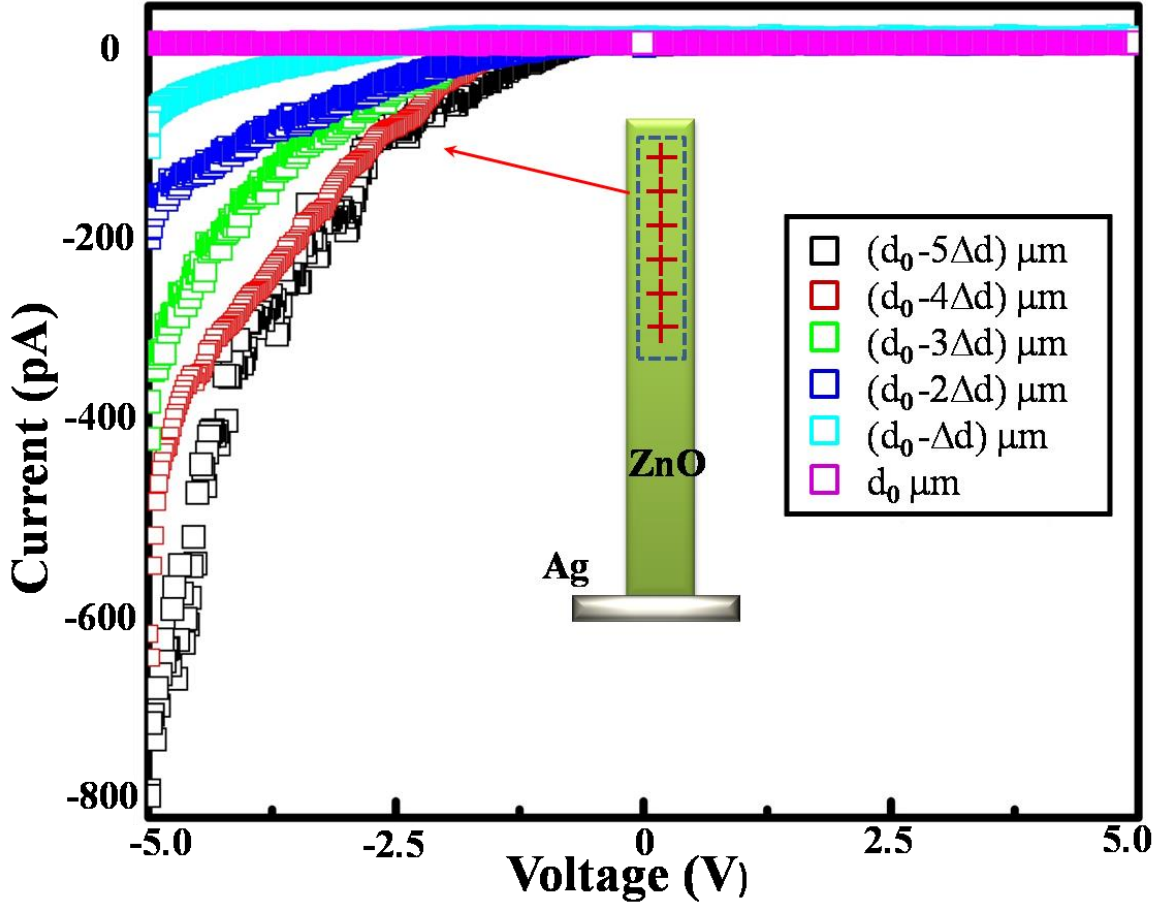


**Figure 3.7.** I-V curves of ZnO MB/NB measured near the cut off length  $d_0$  ( $d_0 \approx 17.7 \mu\text{m}$ ) from the fixing end, displaying a fast drop of the conductance.

### 3.3.6. Additional measurements on other sample with the same growth direction

Based on the same data processing approach and assuming mechanism model in this chapter, we can obtain  $R_d = a_1 \exp(a_2 \times d)$  with coefficients ( $a_1 = 0.2883$ ,  $a_2 = 0.4289$ ) as showing in Figure 3.8(c). This equation can be rewritten as polynomials,  $R_d = \frac{0.4865 \times d}{1 - 0.064 \times d}$ . Hence, we can deduct the corresponding main conduction planes are  $(10\bar{1}0)$ ,  $(\bar{1}100)$ ,  $(\bar{1}010)$  and  $(1\bar{1}00)$  planes with  $\theta = 60^\circ$  in equation (3.7) in this chapter. The same conclusion in this chapter can be achieved here.

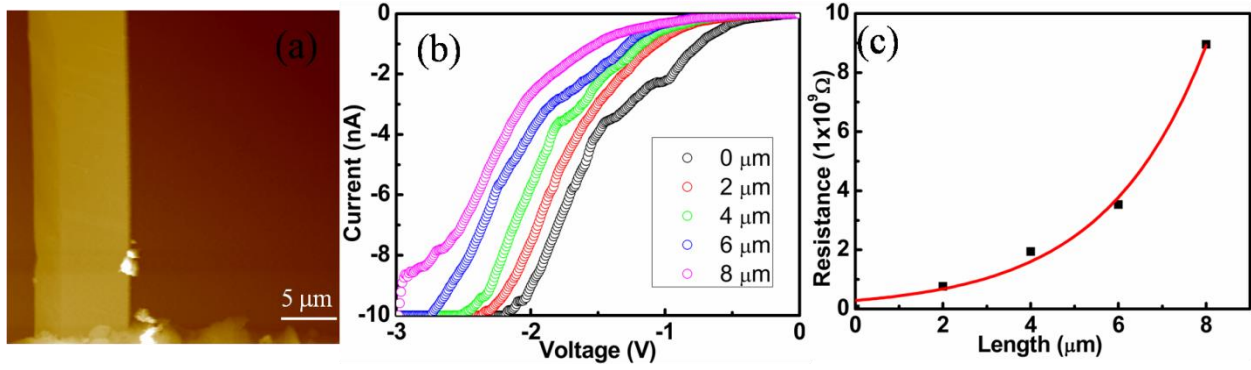


**Figure 3.8.** C-AFM measurement of ZnO MB/NB.(a) Topography of ZnO MB/NB acquired by AFM in tapping mode;(b) I-V curves of ZnO MB/NB with different lengths connected in the measuring circuit.(c) The measured resistances of the ZnO MB/NB with different lengths were connected in the measuring circuit.

3.3.7. Measurements on ZnO MW/NWs along [0001] growth direction

The comparing measurement result of hexagon ZnO MW/NW showing that its resistances are linear with respect to its length. Furthermore, our mechanism model in this chapter can perfectly explain ZnO MW/NWs growth along [0001] direction. For free standing ZnO NWs growth along c axis, the main conducting planes would be {01-10} planes that are parallel to the longitude direction of the ZnO MW/NW, the angle  $\theta$  in the equation (3.7) is 90 degree so that the resistance is proportional to the length.

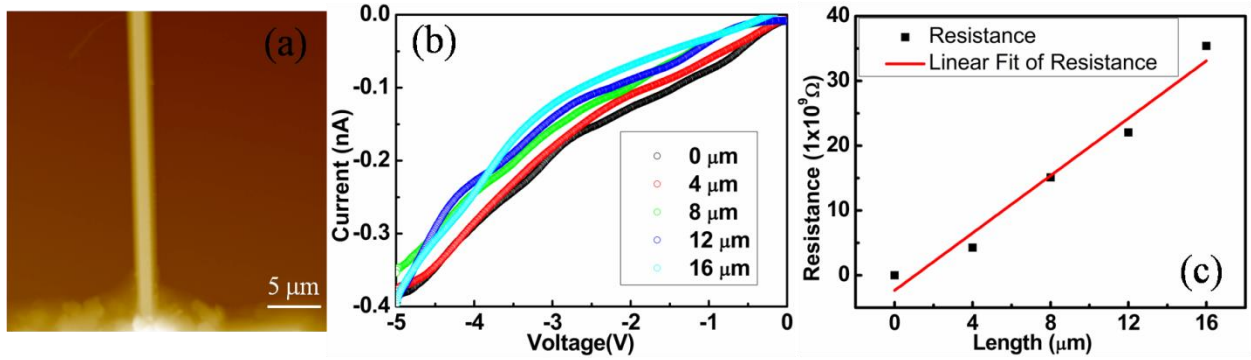


**Figure 3.9.** C-AFM measurement of ZnO MW/NW.(a) Topography of ZnO MW/NW acquired by AFM in tapping mode;(b) I-V curves of ZnO MW/NW with different lengths connected in the measuring circuit.(c) The measured resistances of the ZnO MW/NW with different lengths were connected in the measuring circuit.

### 3.4. Conclusions

In summary, the nonlinear length dependent electrical resistance of a single crystal ZnO MB/NB is from the anisotropic conduction planes inside the crystal. The physical model based on the main conduction planes well explains the nonlinear electron transportation mechanism of single crystal semiconductor materials in micro/nanoscale, and it is possibly to make an applicable use of this knowledge in the next generation micro/nano-electromechanical devices or electrical circuit designs.

## CHAPTER 4 PHYSICAL MODEL CONSTRUCTION FOR ELECTRICAL ANISOTROPY OF SINGLE CRYSTAL ZINC OXIDE MICRO/NANOBELT USING FEM

### 4.1. Introduction

With the progress of science and technology, materials which serve as the basis for constructing any objects are required to be more precisely characterized to satisfy the ever increasing advanced device design demands. Undoubtedly, electrical property is one of the most important basic properties of materials, especially for semiconducting materials, which play key role in semiconducting industry. Furthermore, many materials synthesized in nanoscale exhibit novel and exceptional properties<sup>1, 2, 56</sup> comparing with their bulk counterparts, primarily ascribed to quantum confinement effect and extra-high surface energy at ultra-small size.<sup>4, 104</sup> Electrical property of nanomaterials is also significantly different with its bulk counterparts.<sup>3, 34</sup> The relevant electrical property research on nanomaterial not only improves the scientific understanding of charge carrier transport with nanoconfinement but also guides the nanodevice design and performance.

Our previous experimental result shows that electrical resistance is nonlinear length dependence in the semiconducting single crystal ZnO MB/NB.<sup>3</sup> In this chapter, we report the progress result of the intrinsic electrical anisotropy caused nonlinear resistance-length relation of single crystal ZnO MB/NB via FEM based on C-AFM experimental result. By building 3D model with same parameters as in experiment, a detailed electrical transport mechanism in single crystal ZnO MB/NB has been revealed. By comparing of ECD distribution in different nanocrystallography, the proposed interpretative model that anisotropic conductivity caused the

main transportation channels along specific crystal planes inside MB/NB is well coincided with the experimental measurement. This work was published in *Appl. Phys. Lett.* 2014, 104, 153109.<sup>39</sup>

#### 4.2. Experimental section

As schematically described in Figure 4.1(a), the fundamental C-AFM measurement on single crystal ZnO MB/NB is as following: one end of a single crystal ZnO MB/NB (synthesized by CVD approach<sup>28,60</sup>) was embedded in silver electrode on the insulated silicon oxide layer of an intrinsic silicon wafer substrate. Silver contacting one end of the single crystal ZnO MB/NB formed Ohmic contact<sup>105</sup>, while Pt coated conductive AFM tip acted as Schottky contact.<sup>106</sup> The C-AFM measurement procedure contains two parts: topography image of the ZnO MB/NB was firstly scanned in tapping mode to obtain the whole interested area information, and then to acquire I-V curve in contact mode at different positions as the cross points indicated in Figure 4.1(a), which started from the interface of the ZnO MB/NB and the fixed silver electrode as the zero point of length toward to the free end of the belt (see arrow indicated in Figure 4.1(a)). As what shown in Figure 4.1(b), the corresponding representative I-V curve acquired from one interested position in belt connected in the measuring circuit shows an asymmetry rectifying shape and the forward bias is negative potential relative to the ground indicated in Figure 4.1(a). Similarly, a series of I-V curves under the reversed bias conditions according to the trace schematically marked by the crosses in Figure 4.1(a) can be obtained. The asymmetry rectifying shape I-V curve is resulted from the metal-semiconductor-metal structure composed of ZnO MB/NB-silver electrode Ohmic contact and ZnO MB/NB-Pt AFM tip Schottky contact and the value of the Schottky barrier dominates the typical rectifying nonlinear I-V characteristic<sup>101</sup> rather than the Ohmic contact. The resistance of Schottky contact is identical during all I-V curve

acquisitions, and the quantificational expression of the resistance change with belt length (subtracted Schottky resistance) still preserves a nonlinearly exponential relationship as plotted in Figure 4.1(c), which is contrary to the classic Ohm's law. Clearly, this exceptional nonlinear electrical conductivity behavior is correlated to the intrinsic electrical property of ZnO micro/nanostructure.

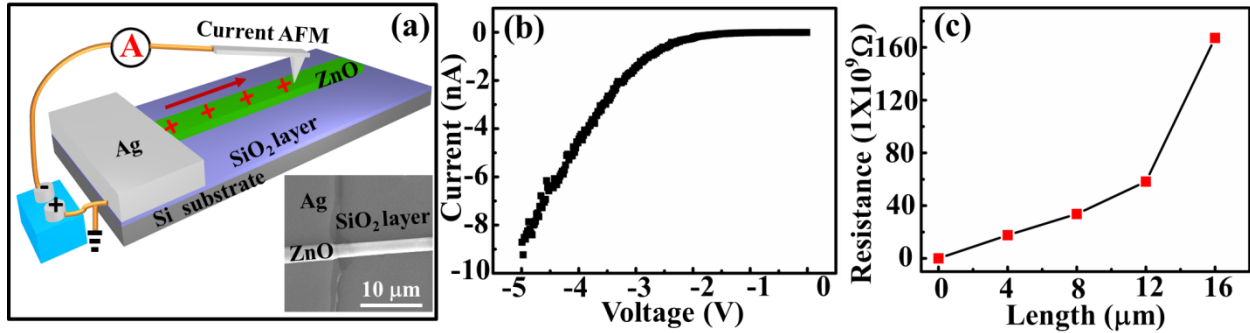


**Figure 4.1.** (a) C-AFM setup for measuring electrical property of anisotropic ZnO MB/NB with different length connected in the circuit, inserted is the SEM image of ZnO MB/NB with one end covered by silver electrode. (b) The representative I-V characteristic by C-AFM acquisition indicated in Figure 4.1(a). (c) The corresponding length dependent nonlinear electrical resistance of ZnO MB/NB.

### 4.3. Model setup

Although this unusual electrical behavior of nonlinear length dependent resistance has been measured and conformed by experiments, further study by simulation approaches is necessary to explore the basic conductivity principles of ZnO MB/NB in micro/nanoscale. Herein, FEM simulation is employed to visually and concretely reveal electrical conductivity distribution inside ZnO MB/NB with the anisotropic conducting mechanism. Figure 4.2(a) shows the scheme of the simulation which is composed by a ZnO MB/NB fixed at its base and along y axis, the bottom is grounded and the top is biased with negative electric potentials. The 3D model is built by Hypermesh software as indicated in Figure 4.2(b) and the same geometric parameters as in experiment.<sup>3</sup> Then, Abaqus software is employed to run analysis, choosing thermoelectric

element type and room temperature, which is capable of achieving desired isotropic and anisotropic characterizations. Finally, a series of electrical current distributions under various conditions are obtained. As a common approximation, the current density simply is proportional to the electric field and can be as expressed by

$$J = \sigma E \quad (4.1)$$

Where  $E$  is the electric field and  $\sigma$  is the electrical conductivity. It reasonably agrees that ECD is proportional to the electrical conductivity if the conductor is under a stable and uniform field. Herein, the change of electrical conductivity can be reflected by changes of current density.

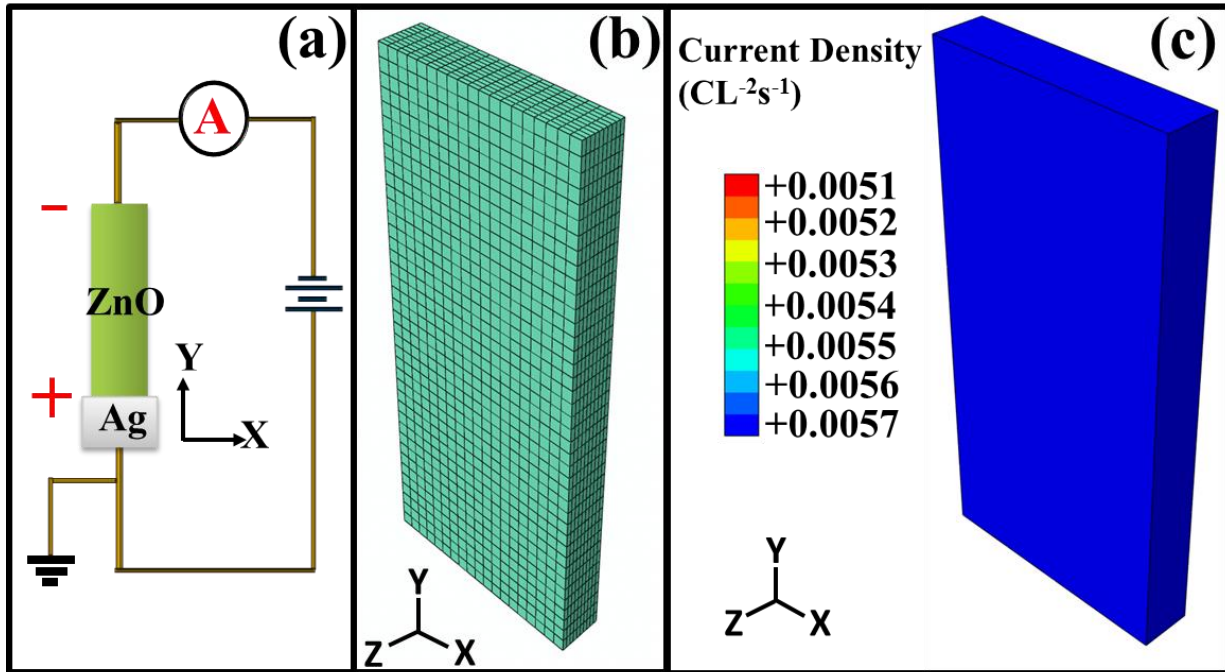


**Figure 4.2.** (a) The scheme of simulation is composed by a ZnO MB/NB grounded and fixed at its bottom end and along y axis, biased electric potential applied at both ends. (b) The meshed MB/NB model built by Hypermesh software according to the conditions presented in Figure 4.2(a). (c) ECD distribution along y axis for an isotropic ZnO MB/NB in simulation.

## 4.4. Results and discussion

### 4.4.1. Electrical isotropy simulation

Figure 4.2(c) tells the ECD distribution along longitudinal direction ( $y$  direction) of ZnO MB/NB with isotropic electrical conductivity. It can be obviously seen that current density distribution keeps constant inside the belt body and uniformly distributes, so does the electrical conductance in the ZnO MB/NB, which satisfactorily meets with the classic theory that conductance is distributed uniformly in the isotropic materials.

### 4.4.2. Electrical anisotropy simulation

By substituting electrical data from experiment and previous literatures<sup>3, 107</sup>, it is interesting to find that ECD distribution of anisotropic ZnO MB/NB along  $y$  direction displayed in Figure 4.3(a) reveals the existence of parallel main conducting planes which have the larger current density or higher electrical conductivity than those planes in other directions. Furthermore, the geometric relationship between conducting planes and MB/NB dimensions is revealed in Figure 4.3(b). Therefore, it is possible to conduct a generic formula quantitatively describing the electrical anisotropy of ZnO MB/NB, particularly resistance-length characteristic from FEM simulation result.

Here, the tensor algebra is used to describe the electrical anisotropy of ZnO MB/NB. Since the anisotropic electrical conductivity ( $\sigma$ ) is a 2-rank Cartesian tensor and ZnO has the six folds symmetry hexagonal crystal structure with space group of  $P6_3mc$ , the off-diagonal elements of the tensor are zero<sup>108</sup>, so the anisotropic tensor of electrical conductivity can be written as

$$\sigma_{ij} = \begin{pmatrix} \sigma_{11} & 0 & 0 \\ 0 & \sigma_{22} & 0 \\ 0 & 0 & \sigma_{33} \end{pmatrix} \quad (4.2)$$

While here we can assume both electrical resistance ( $\vec{R} = R_x \vec{i} + R_y \vec{j} + R_z \vec{k}$ ) and the effective transportation length of conducting planes  $\vec{l} = l_x \vec{i} + l_y \vec{j} + l_z \vec{k}$  which are directional vectors in the Cartesian coordinate as shown in Figure 4.3(b). Herein, the total electrical resistance of ZnO MB/NB can be expressed as

$$\vec{R} = \frac{\vec{l}}{\sigma_{ij}s} = \begin{pmatrix} R_x \\ R_y \\ R_z \end{pmatrix} = \frac{1}{s} \bullet \begin{pmatrix} \frac{1}{\sigma_{11}} & 0 & 0 \\ 0 & \frac{1}{\sigma_{22}} & 0 \\ 0 & 0 & \frac{1}{\sigma_{33}} \end{pmatrix} \bullet \begin{pmatrix} l_x \\ l_y \\ l_z \end{pmatrix} = \frac{1}{s} \bullet \begin{pmatrix} \frac{l_x}{\sigma_{11}} \\ \frac{l_y}{\sigma_{22}} \\ \frac{l_z}{\sigma_{33}} \end{pmatrix} \quad (4.3)$$

As shown in Figure 4.3(b), we have  $\vec{l} = l_x \vec{i} + l_y \vec{j}, l_z = 0$ , the resistance component in y direction is determined by

$$R_y = \frac{1}{s} \times \frac{l_y}{\sigma_{22}} = \frac{d}{\frac{1}{2} \sigma_{22} \times h \times w \times \sin 2\theta \times (1 - \frac{d}{w \times \tan \theta})} \quad (4.4)$$

From the classic Pouillet's law, here  $\sigma$ ,  $s$ ,  $d$ ,  $w$ ,  $h$  and  $\theta$  are electrical conductivity, cross sectional area, length, width, thickness of a given ZnO MB/NB and the complementary angle of main conduction planes with the longitudinal direction of the ZnO MB/NB, respectively. Considering the anisotropic ECD distribution and from equation (4.4), we can obtain the length-resistance curve of anisotropic ZnO MB/NB at  $\theta=50^\circ$  as shown in Figure 4.3(c), which exactly matches with the experimental measurement of resistance-length relation.<sup>3</sup>

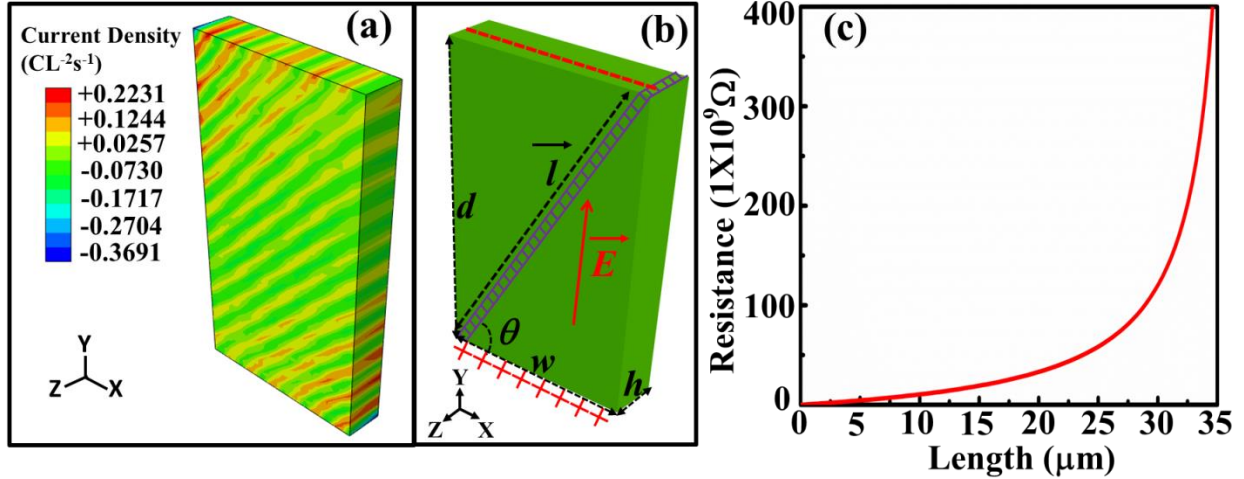


**Figure 4.3.** (a) ECD distribution along y axis for anisotropic ZnO MB/NB. (b) The principle model describing favorite conducting planes of the electron transport channel with larger moving current density has an angle  $\theta$  with electric field along y axis (potential applied on the ZnO MB/NB across top and bottom ends). (c) The corresponding nonlinear length dependent resistance plot.

#### 4.4.3. Case study

As a specific case, it is predicable to obtain  $\theta$  by  $(\frac{\pi}{2} - \theta)$  rotation of ZnO MB/NB along z axis with keeping the same electric field (see Figure 4.4(a)) in FEM simulation, then main conducting planes will be perpendicular to the electric field which is equivalent to the case of ZnO MB/NB grown along [0001] direction. Figure 4.4(b) shows the current density distribution in y direction after rotating the favorite conduction planes to parallel y axis, revealing that the current is mainly transported from top end to bottom in a longitudinal direction also the growth direction, which was supported by our experiment measured result that c axis grown ZnO MB/NB has linear I-V characterization.<sup>3</sup> Furthermore, it also clearly corresponds to the situation that  $\theta=90^\circ$  in equation (4.4), and that the resistance is linearly proportional to the material length as Ohm's law predicted as shown in Figure 4.4(c).

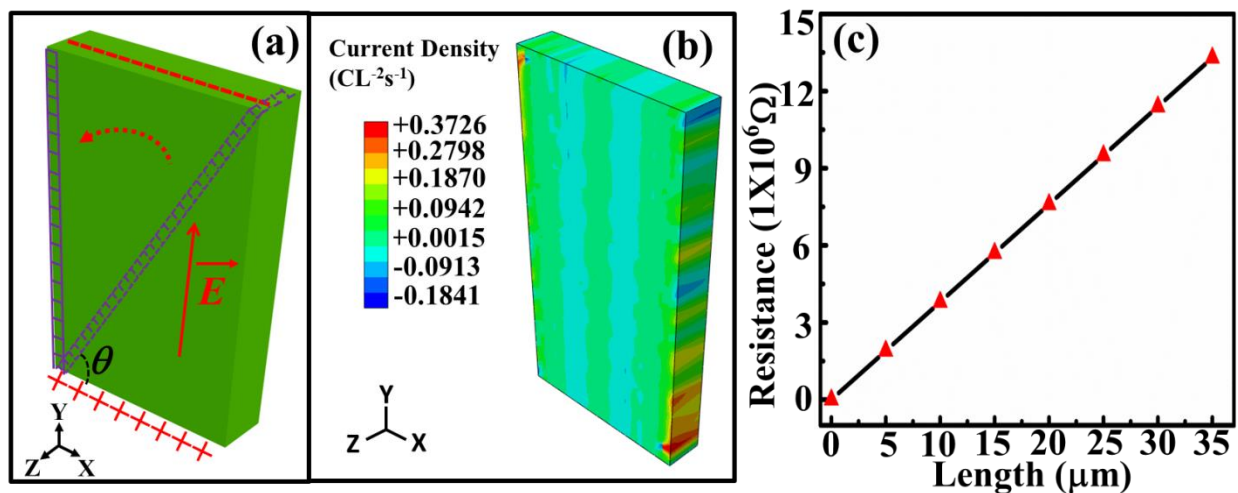


**Figure 4.4.** (a) Schematic situation of the conducting planes rotates ( $\pi/2 - \theta$ ) and becomes along z axis while keeping the same applied potential on the both ends. (b) ECD distribution for anisotropic ZnO MB/NB model built in Figure 4.3 after ( $\pi/2 - \theta$ ) rotation along z axis. (c) The corresponding linear length independent resistance plot from simulation.

Moreover, For ZnO MB/NB grown in different direction with anisotropic electrical conductivity  $\sigma$ , equation (4.3) can directly give quantitative expression of its electrical property toward three coordinate directions. Those outcomes further verify the accuracy of supposed interpretation model that anisotropic conductivity and induced main conducting planes lead to the nonlinear length dependent resistance behavior of ZnO MB/NB. As to other semiconducting materials, the approach can be likewise applied to further understand the fundamental electrical properties.

#### 4.5. Conclusions

In conclusion, FEM simulation has been used to investigate the intrinsic electrical property of single crystal ZnO MB/NB and successfully predicted the detailed ECD distribution inside the ZnO MB/NB. The simulation result is perfectly fitted with experimental data that nonlinear length dependent resistance is associated with its electrical anisotropy of materials and hence the appearance of main conducting planes. This research favors the understanding of basic electrical

transportation mechanism among isotropic and anisotropic semiconducting materials in fine confinements, especially with nanoscale confinement.

## CHAPTER 5 PHOTOELECTRIC PROPERTY MODULATION BY NANOCONFINEMENT IN THE LONGITUDE DIRECTION OF SHORT SEMICONDUCTING NANORODS

### 5.1. Introduction

1D nanomaterials, like NRs, NWs, and NTs have been widely investigated for their extraordinary mechanical, electric, piezoelectric, and photoelectrical properties<sup>38, 109, 110</sup>, which origin from the ultra-high surface to volume ratio and quantum effects. Additionally, nanodevices with superior performance have been made possible by 1D nanomaterials.<sup>111-119</sup> Correspondingly, photoelectric property, one of the most important characteristics of semiconductors, undergoes significant change in 1D nanomaterials. For instance, the exposure of ZnO surfaces to light irradiation induces photodesorption of oxygen molecules from the surface, which leads to a rise of conductivity.<sup>120</sup> As the photoelectric property of ZnO is heavily affected by material surface, it experiences significant change as material size reduces into nanoscale.<sup>40</sup> There are a great number of studies on photoelectric property of 1D and 0D (i.e., nanoparticle) nanomaterials.<sup>40, 121</sup> Further, photoelectric property should undergo significant change due to the appearance of the nanoconfinement in the third dimension (longitude direction) as the 1D nanomaterials reduce length to size in between 1D and 0D (aka 0.5D nanomaterial). However, few studies have been carried out on photoelectric property of 0.5D nanomaterial besides our recent publication work.<sup>37</sup> In that publication, we first defined 0.5D nanomaterials and studied photoelectric property change with 0.5D nanomaterial diameter and length. Nevertheless, photoelectric property is the photo-induced electric property change of semiconducting materials and it should heavily rely on the illuminating light intensity besides nanomaterial's size.<sup>122, 123</sup>

Thus, it is highly desired to study the photoelectric property change of 0.5D nanomaterials with light intensity and the third nanoconfinement in longitude direction.

In this chapter, we focus on the origin of photoelectric property by studying light illumination-induced photoelectron density change in ZnO NR with length variance covering 0.5D nanomaterial range. The photoelectric property of 0.5D ZnO nanomaterials as function of illuminating light density and the third dimensional nanoconfinement is systematically studied by both characterizing photoelectric current through C-AFM and measuring photo-induced surface potential change via SKPM technique. Those experiments invariably show the photo-induced electron density is significantly modulated by light intensity and the appearance of nanoconfinement in the longitude direction. Furthermore, photo-induced free electron density distribution in 0.5D semiconducting materials is simulated through (FDTD) method by a new theoretical model with quantum corrections, which fits the measured experimental results well. Undoubtedly, results of this study are critical for improving the basic understandings of semiconducting nanomaterials in intermediate scale and developing 3D nanodevices, like high sensitive photodetectors, ultra-high resolution digital image sensors, and more.<sup>124</sup> This work was published in *ACS Appl. Mater. Interfaces* 2016, 8, 11001-11007.<sup>125</sup>

## 5.2. Experimental section

### 5.2.1. Synthesis of 0D, 0.5D and 1D ZnO nanomaterials

The 0D, 0.5D and 1D ZnO nanomaterials used in the experiment were obtained by controlling the heights of ZnO NR arrays, and the synthesis process followed the generic wet chemical method.<sup>24, 126</sup> In detail, conductive substrates (n-type gallium nitride, or n-type silicon) were placed facing down and floating on the mixed solution of 0.05 M hexamethylenetetramine and 0.05 M zinc nitrate hexahydrate (volume ratio 1:1) in a beaker; the reaction temperature was kept

at 90 °C. The growth duration controls the height of NRs so as to synthesize 0D, 0.5D and 1D nanomaterials.

#### 5.2.2. Characterization of 0D, 0.5D, and 1D nanomaterials

The morphologies and topographies of the as-grown ZnO nanomaterials with different heights were characterized by FESEM ( JEOL 7000) and AFM (Park Systems XE-70) in non-contact mode, respectively. The TEM ( TECNAI F20) with an accelerating voltage of 200 kV was used to characterize ZnO NR and analyze its crystal structure.

#### 5.2.3. Photoelectric property measurements with C-AFM

The I-V data acquisitions were carried out by the C-AFM (Park Systems XE-70) with a Pt-coated AFM tip (ANSCM-PC, Applied Nanostructures, Inc.), a 355 nm laser with tunable power supply (PSU-H-LED, Cnilaser) worked as the illumination source from side. Figure 5.1(a) shows the experimental setup for the measurements, when the C-AFM tip contacted on the top of the ZnO NR, the current throughout the NR could be acquired with an applied bias in dark or under illuminating conditions.

#### 5.2.4. Photoelectric property measurements with SKPM

Similarly, the same light illumination in C-AFM characterization was used in SKPM ( Park Systems XE-70) measurement. The SKPM tip for surface potential testing was Pt-coated conductive AFM tip (PtProm 1M\_T, Park Systems). Unlike C-AFM to directly applying a DC bias, SKPM characterized the ZnO nanomaterials' surface potential by external AC field modulation and lock-in amplifying technique.

### 5.3. Results and discussion

#### 5.3.1. Measurement setup and materials characterization

Photoelectric property C-AFM characterization setup is schematically shown in Figure 5.1(a). Semiconducting ZnO nanomaterial arrays at a fixed diameter are grown on substrate with relatively low density. Conductive AFM tip touches the top of a nanomaterial to form a close circuit for characterizing I-V curve in dark or under light illumination. Such a design significantly reduces the complicated sample manipulation and electrodes fabrication in addition to the convenience of choosing a nanomaterial with a specific height. The well aligned ZnO nanomaterial arrays with constant diameter of 100 nm but different heights in the experiments were grown on conductive gallium nitride substrate by wet chemical method.<sup>24, 126</sup> The upper of Figure 5.1(b) shows the TEM image of the as-grown ZnO nanomaterial under low magnification; lower part of Figure 5.1(b) is the HRTEM image, revealing growth direction is [0001]. Through growing duration, well aligned ZnO nanomaterial arrays with a constant diameter of 100 nm but different heights are successfully synthesized as shown in the SEM images in Figure 5.1(c)-1(h), which serve as the material platform covering 1D, 0.5D, to 0D nanomaterials. Insets in Figure 5.1(c)-1(h) are the topography images scanned by noncontact mode AFM, revealing the ZnO nanomaterial's height decreases in sequence. It has to be pointed out that the density of the ZnO nanomaterial arrays should be lower enough so that the AFM tip can specifically contact the targeted ZnO nanomaterial without touching others. Additionally, all ZnO nanomaterials are controllably grown with a diameter of ~100 nm and nanomaterials selected and characterized in this work have the same diameter of 100 nm to guarantee the constant two-dimensional (2D) confinements along the radial direction, leaving the height as the only variable in the third dimension.

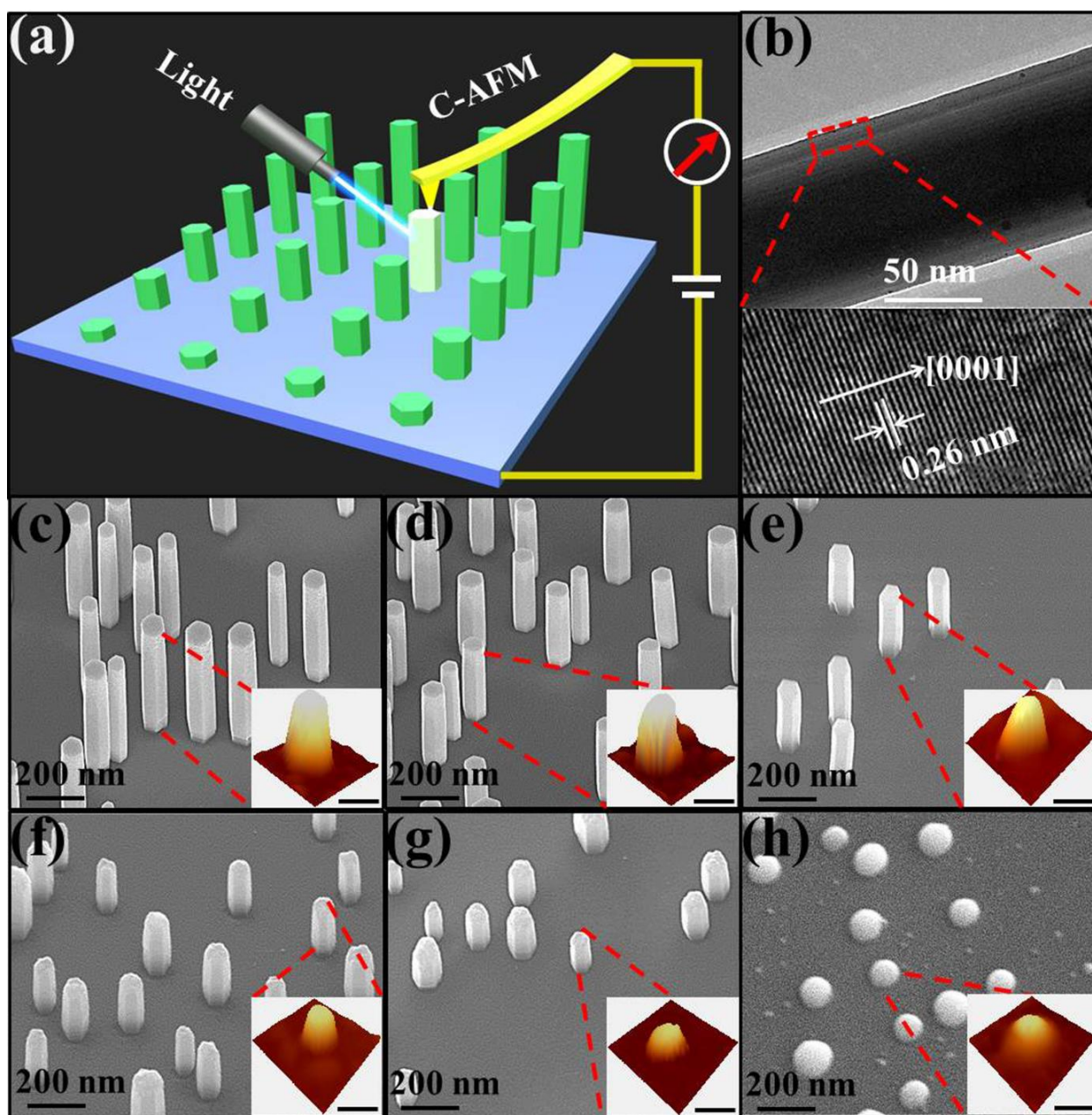


**Figure 5.1.** (a) Schematic diagram of C-AFM setup for measuring photoelectric property of ZnO nanomaterials. (b) Low magnification TEM and HRTEM images of the as-synthesized ZnO NRs. (c)-(h) SEM images of ZnO nanomaterials within constant diameter of 100 nm but varied height ranging from 1D to 0D (insets are the corresponding AFM topographies, scale bars are 200 nm).

### 5.3.2. C-AFM direct I-V acquisition

Figure 5.2(a) is the acquired I-V profiles of a randomly selected ZnO nanomaterial with height in 0.5D nanomaterial range (as shown in the SEM image inset) under dark and light illumination

(70 mW/cm<sup>2</sup>). In this experiment, a 355 nm laser with tunable power (PSU-H-LED, Cnilaser) is used to stimulate ZnO nanomaterials (see the inserted emission spectrum of the laser in Figure 5.2(a)). I-V curves are acquired in dark and illumination separately by contacting the top of the nanomaterial with a conductive AFM tip after locating the target nanomaterial by the topography of the sample obtained via AFM in non-contact mode. The 0.5D ZnO nanomaterial is sensitive to UV light illumination through a dramatic current increase from the dark current, and the I-V curves have an asymmetry rectifying shape due to the Schottky contact formed by Pt AFM tip and n-type semiconducting ZnO nanomaterial.<sup>3</sup> Figure 5.2(b) shows the acquired I-V curves of the same ZnO nanomaterial as in Figure 5.2(a) under illumination with four different light intensities of 1, 33, 67, and 100 mW/cm<sup>2</sup>, respectively. It is obvious that electrical conductance increases as the intensity goes up and the ZnO NR has detectable photoelectric response even with a very weak UV light illumination. Furthermore, a quantitative data acquisition of the I-V curves has been conducted for ZnO NRs with different heights (cover 0D, 0.5D, and 1D ZnO nanomaterials) under the same four different light intensities illuminations. As the data shown in Figure 5.2(c), with a constant intensity light illumination, 0D ZnO nanomaterials have indistinguishable photoresponse  $\Delta I$  (the current difference between under illumination and dark) between in dark or under light illumination; the photoresponses of 0.5D nanomaterials are proportional to the height; but when the height of ZnO nanomaterials (constant diameter of 100 nm) continues raising and approaching to conventional 1D scale, the photoresponse will stop at a peak value then begin dropping slightly, which indicates reaching supersaturate state. Figure 5.2(d) is the 3D contour plot of photo-induced electron density ( $n$ ) of the ZnO nanomaterials as a function of light intensity ( $I_{\text{light}}$ ) and height (diameter is constant 100 nm), which is generated from more than 300 experimental characterizations and smoothed by Matlab software.

Apparently, 0D nanomaterial is insensitive to UV light illumination, which is obviously different from 0.5D and 1D NRs. Similarly, electron densities are also modulated by nanoconfinement in the third dimension, which results in the significant photo-induced electron density change in 0.5D and 1D ZnO nanomaterials. In addition, at a fixed height, photocurrent of ZnO nanomaterial obeys a power law to external illumination light intensity as observed in previous literatures.<sup>115, 127</sup> As the UV light intensity continues increasing, the photocurrent of ZnO will not

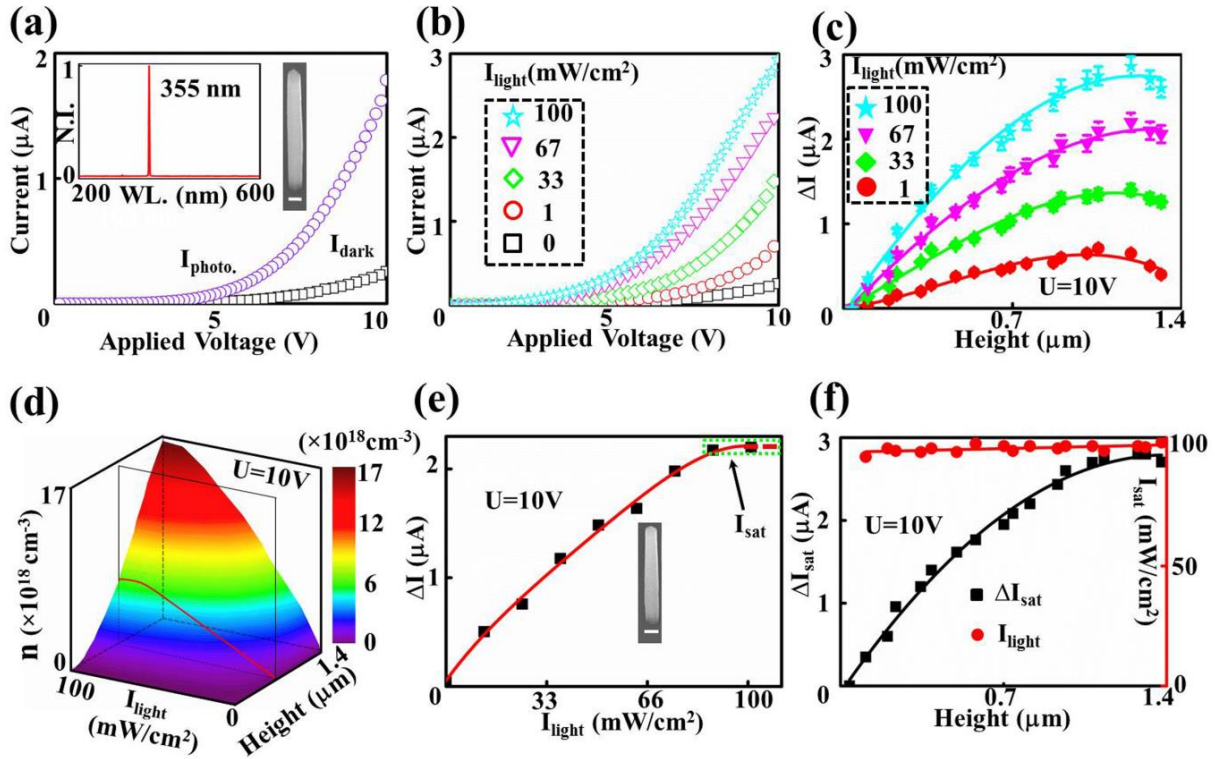


**Figure 5.2.** (a) I-V curves of a 0.5D ZnO NR acquired by C-AFM in dark and under light illumination (inserted emission spectrum shows the wavelength of the monochromatic light source used in the measurements and inserted SEM image is the selected ZnO NR with the scale bar of 100 nm). (b) I-V curves for the same NR tested in Figure 5.2(a) upon five different light illumination intensities. (c) Quantitative plot of ZnO nanomaterial photoresponse with height (the third dimensional confinement) upon four different light illuminations acquired by C-AFM. (d) The measured corresponding 3D contour plot of the photo-induced electron density as a function of ZnO nanomaterial height and light illumination intensity. (e) Under 10 V bias, the photoresponse versus illuminating light intensity for a randomly selected 0.5D ZnO nanomaterial showing the photoresponse increases with light intensity till to saturation (scale bar of the inset SEM image is 100 nm). (f) The plots of the saturated photoresponse (left) of ZnO nanomaterial changes with height ranging from 0D to 1D and the corresponding light intensity at current saturation (right).

infinitely increase but reach a stable and constant state, called light saturation.<sup>128</sup> The curve in Figure 5.2(e) shows a typical photoresponse vs light intensity of a 0.5D ZnO nanomaterial at a fixed height of 650 nm (as the intercept indicated in Figure 5.2(d)), revealing that photoresponse is exponential to the light illumination intensity and then becomes saturated as the light intensity approaching 90-100 mW/cm<sup>2</sup>. In Figure 5.2(f), every red dot is the saturated light intensity of the ZnO nanomaterial with different height but a fixed diameter of 100 nm, and black dots are the corresponding saturated photoresponse. It can be seen that saturated light intensities are almost the same for the ZnO nanomaterials at a constant diameter.

### 5.3.3. SKPM surface potential mapping

Alternatively, we also studied the sample with SKPM characterization to reveal photoelectrons change in ZnO nanomaterials with constant diameter of 100 nm. When ZnO material is exposed to light illumination, surface potential (absolute value) decreases due to the photo-induced free electrons<sup>129</sup> and material surface potential could be characterized by SKPM.<sup>130, 131</sup> Figure 5.3(a) is the topography of vertical ZnO nanomaterials with constant diameter of 100 nm, which is obtained by scanning AFM in non-contact mode. Figure 5.3(b) and 3(c) are the corresponding images of the same sample area scanned by the same AFM in SKPM module in dark and under 80 mW/cm<sup>2</sup> light illumination, respectively. Clearly, sample surface potential reduces as it exposed to UV light illumination, which is confirmed by the brighter SKPM image of the sample under illumination than in dark condition. Selecting a scan line across ZnO nanomaterials with different height as the green lines indicated in Figure 5.3(a), 3(b), and 3(c), the profiles of the corresponding scan lines for the same scanning position are shown in Figure 5.3(d). Heights of two typical ZnO NRs with constant diameter of 100 nm that have been scanned are marked (1,230 nm and 685 nm) in the topography scan profile and the corresponding surface potentials

of the NRs can be directly read from the SKPM scanning profiles as 1.61 V and 1.50 V under illumination and 1.92 V, 1.83 V in dark, respectively. Similarly, by plotting surface potential of ZnO nanomaterials with different heights ranging from 0D to 1D as shown in Figure 5.3(e), the surface potential of nanomaterial in dark (black square) is always higher than that of it under illumination (red dot). Since the surface potential originates from the electrostatic potential energy of charges confined on surface and stands for the amount of confined electrostatic carriers, like electrons here, the higher is the surface potential, the greater is the electron concentration on the surface. As to ZnO nanomaterials, in dark, oxygen molecules are adsorbed on the whole surface and capture electrons from the material forming a low conductivity depletion layer.<sup>132, 133</sup> If with UV light illumination, photo-generated holes will migrate and accumulate to the surface by band bending so as to discharge the adsorbed oxygen ions, which reduces the electron density on the surface and lowers surface potential.<sup>128</sup> In such a scenario, photo-induced electron density ( $n_{s \rightarrow v}$ ) from surface oxygen ions dissociation under illumination can be expressed as

$$n_{s \rightarrow v} = \frac{S(\sigma_{dark} - \sigma_{light})}{V} \quad (5.1)$$

Where  $S$  is the nanomaterial surface area,  $\sigma$  stands for the surface charge density,  $V$  represents the volume of nanomaterial. Surface charge density can be directly deduced from surface potential, which can be effectively characterized by SKPM. Thus, electron density change that is caused by photo-induced electrons from materials surface as a function of light intensity and nanomaterial height is characterized as in Figure 5.3(f). The 3D plot is generated from the measurements of more than 100 ZnO nanomaterials scanned by SKPM under different light intensities and further smoothed by Matlab software. Clearly, photo-induced electron density change from surface oxygen ion reduction increases as illuminating light intensity and decreases

with ZnO nanomaterial's height, indicating 0D and 0.5D ZnO nanomaterials have strong surface photoresponse.

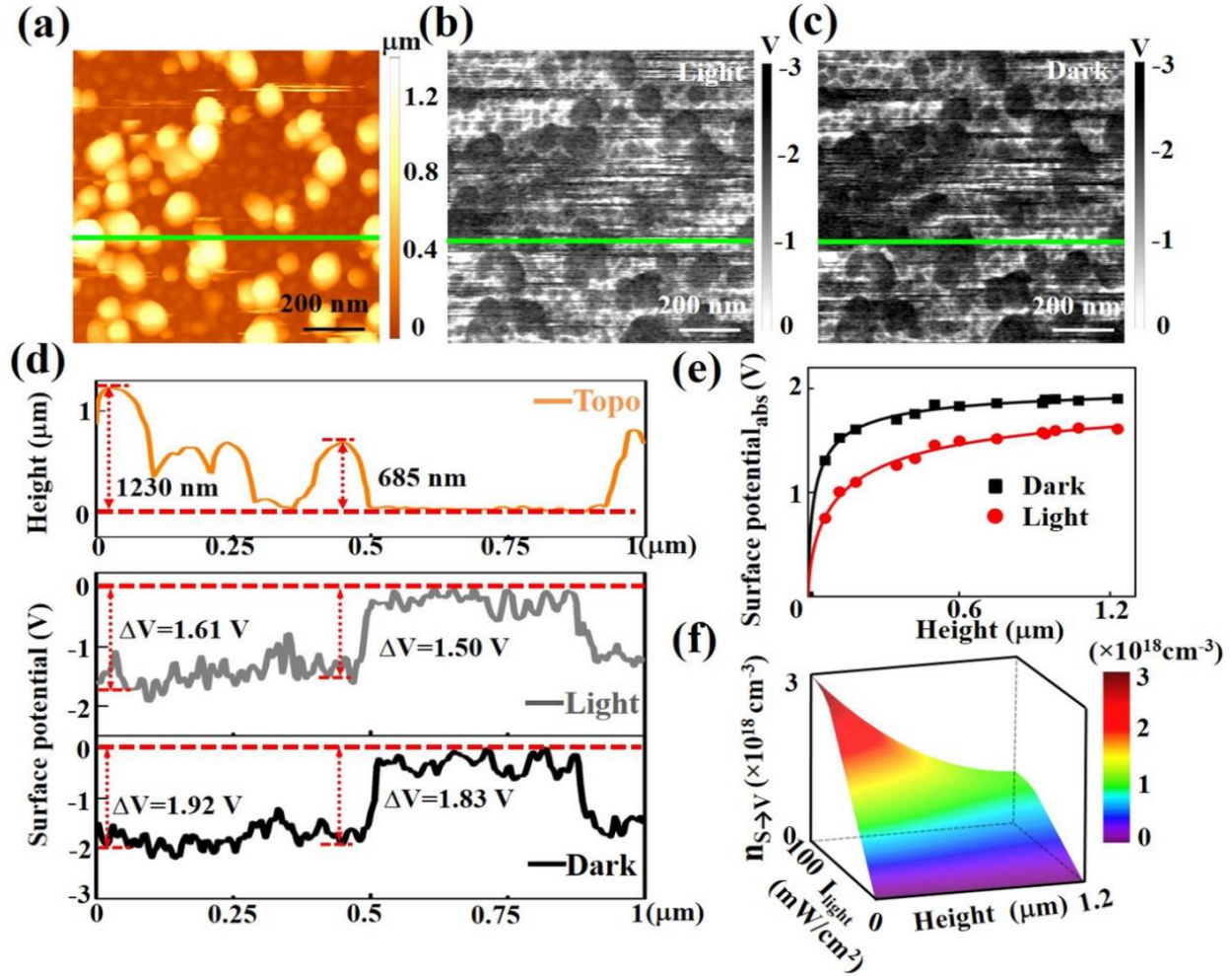


**Figure 5.3.** (a) AFM topography of a sample with vertical ZnO nanomaterials ranging from 0D to 1D scanned in non-contact mode. (b)-(c) The corresponding surface potential 2D mappings for vertical ZnO nanomaterials shown in Figure 5.3(a) under light and in dark conditions by SKPM measurement. (d) Scan line profiles for the same sample position from Figure 5.3(a)-3(c) (green line), showing the potential difference of the same ZnO nanomaterial in dark and under illumination. (e) The surface potential plot of ZnO nanomaterials changes with height ranging from 0D to 1D in dark and under light illumination. (f) The 3D contour plot of the measured photo-induced electron density change from surface as a function of ZnO nanomaterial height and light illumination intensity.

#### 5.3.4. Theoretical model propose and interpretation

Based on the two experimental methodologies, we carry out simulation by proposing theoretical mode for photoelectric property of 0.5D nanomaterial. It is well known that

photoelectric property of bulk/microscale semiconductors follows ohm's law<sup>37</sup>: with a constant diameter, as the height of the photoelectric material increases its photocurrent decreases under a fixed bias. However, when the material size falls into nanoscale, only 1D semiconducting nanomaterials follows this principle, while the 0D and 0.5D nanomaterials behave differently as in the foregoing experiments. By classical theory, the free electrons distribution is uniformly distributed in the 0.5D ZnO nanomaterials, as the Lumerical FDTD simulation result shown in Figure 5.4(a). The corresponding photo-induced electron density as function of illumination power and ZnO nanomaterial (fixed diameter of 100 nm) height is calculated as in Figure 5.4(b). It is clear that photo-induced electron density is independent on the geometric size of nanomaterial, only affected by the stimulated light intensity, which is obviously deviated from the experimental results obtained by C-AFM I-V curve characterization. Based on classical model, there is no surface effect contributing to material's photoresponse, so the photo-induced electron density change from the surface is zero as shown in Figure 5.4(c). Furthermore, quite a few literatures reported the photoelectric property of nanomaterials is size related.<sup>134, 135</sup> Herein, in order to understand photoelectric properties of nanomaterials ranging from 0D to 1D, especially to 0.5D, quantum effect, size effect, and surface effect have to be taken into account to build a new accurate model. Stemming from the model of our previous work that photoelectric property of 0.5D nanomaterial is a function of material's diameter and length<sup>37</sup>, a much more precise model of the photo-induced electron density  $n$  inside ZnO nanomaterials under external illumination is deduced as

$$n = (n_{thermal} + n_{pe}) - (1 - \frac{r_b}{R_{rod}})(n_{thermal} + \frac{2\lambda_{mfp}n_{ne}}{h_{rod}}) \quad (5.2)$$

Here  $n_{thermal}$  stands for the thermal electron density;  $n_{pe}$  means the electrons density from light excitation;  $r_b$  is the Bohr radius for ZnO<sup>136</sup>;  $\lambda_{mfp}$  is the mean free path for ZnO NR<sup>137</sup>;  $n_{ne}$  is the

non-equilibrium electron density;  $R_{\text{rod}}$  and  $h_{\text{rod}}$  is the radius and height of the ZnO NR, respectively. Figure 5.4(d) is the simulated free electron density in the cross-section of a 0.5D ZnO nanomaterial based on equation (5.2), in which electron density is not uniform but higher in the core and lower close to the outer surface. While the excited electron density can be written as<sup>138</sup>

$$n_{pe} = \frac{N_C A}{V} = \frac{\eta I_d \lambda A}{V h c} \quad (5.3)$$

Where  $N_C$  is total electrons number generated per square meter,  $V$  is the material volume,  $A$  is the photo illuminated area,  $\eta$  is the quantum efficiency,  $I_d$  is the light illumination intensity,  $\lambda$  is the light wavelength,  $h$  is the Boltzmann constant, and  $c$  is the light speed in vacuum. Therefore, by combining equation (5.2) and (5.3), in which only nanomaterial's height  $h_{\text{rod}}$  and illumination light intensity  $I_d$  are variables, a 3D contour plot of the photo-induced electron density as function of light intensity and materials height can be calculated as shown in Figure 5.4(e). Obviously, the result based on the new model fits the C-AFM characterization well. In addition, according to the oxygen molecules absorption-adsorption process, the amount of reduced electrons which were previously captured by oxygen molecules on the surface equal to the holes generated by photo excitation. Thus, the photo-induced electron density from surface effect can be achieved by the following expression

$$n_{S \rightarrow V} = \frac{\alpha S n_{pe}}{V} \quad (5.4)$$

Where  $\alpha$ ,  $S$ ,  $n_{pe}$ ,  $V$  is the recombination coefficient, material surface area, excited electron density, and volume of nanomaterial, respectively. Thus, the photo-induced electron density from surface effect can be calculated as shown in Figure 5.4(f). Clearly, photo-induced electron density change from surface depends on light intensity and nanomaterial's height, which agrees

well with the experimental characterization by SKPM method (Figure 5.3(f)). So, the new model together with the methodology could be applied to more accurately predict photoelectric property of other semiconducting nanomaterials in 0.5D.

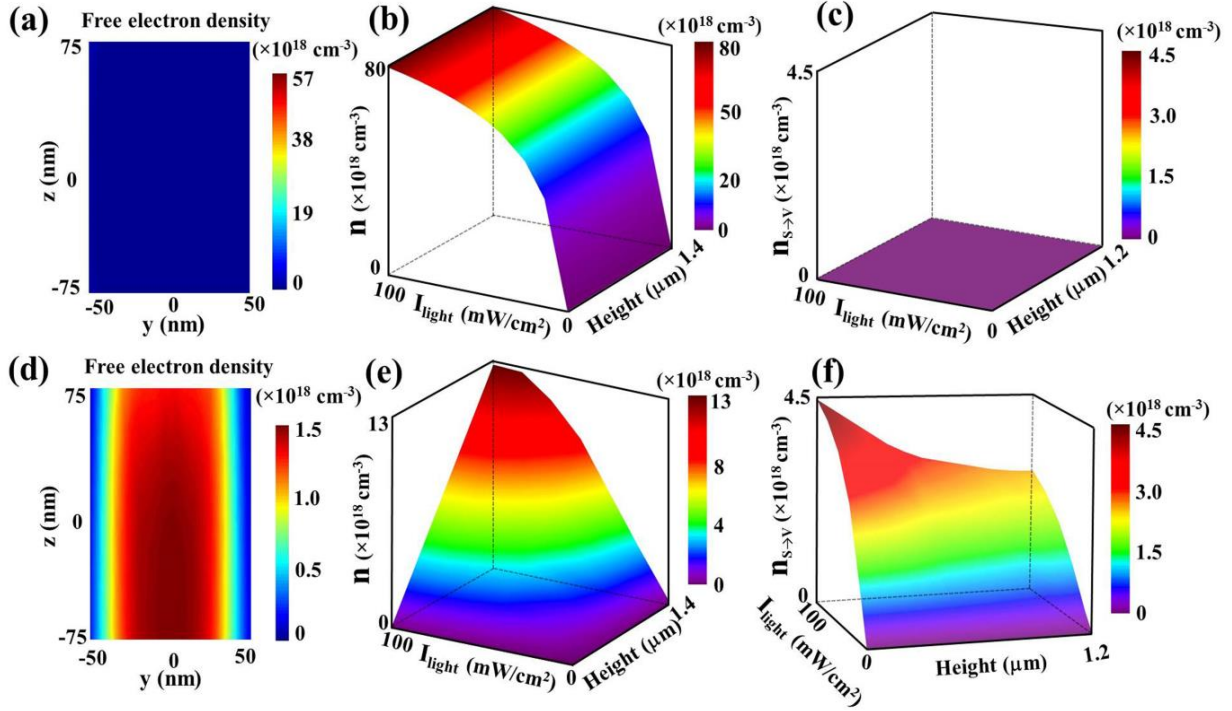


**Figure 5.4.** (a) FDTD simulation of free electron distribution inside a 0.5D ZnO nanomaterial upon light illumination of  $20 \text{ mW/cm}^2$  based on classical theory. (b) The corresponding 3D contour plot of photo-induced electron density as a function of the light illumination intensity and the ZnO nanomaterial height based on classical theory. (c) The calculated corresponding 3D contour plot of the photo-induced electron density from surface as a function of ZnO nanomaterial height and light illumination intensity. (d) FDTD simulated free electron distribution of a 0.5D ZnO nanomaterial under light illumination of  $20 \text{ mW/cm}^2$  by the new model with quantum corrections. (e) The calculated corresponding 3D contour plot of photo-induced electron density of ZnO nanomaterial as a function of light illumination intensity and the material height by the new model with quantum corrections. (f) The calculated corresponding 3D contour plot of photo-induced electron density from surface of ZnO nanomaterial as a function of light intensity and the material height by the new model.

#### 5.4. Conclusion

In summary, the photoelectric property of 0.5D ZnO nanomaterial is systematically studied. Photo-induced electron density exceptionally changes with 0.5D nanomaterial's height and the

illuminating light intensity, which has been experimental characterized by two independent methods: C-AFM I-V acquisition and SKPM surface potential scanning. A new model by considering surface effect, quantum effect, and light intensity effect has been proposed to describe the electron density distribution in 0.5D nanomaterial and well fits the experimental measurements. The results reported here reveal the unique photoelectric property of 0.5D semiconducting nanomaterials and further could be used to predict the photoelectric performance of 0.5D semiconducting nanomaterials, which would have potential impact on 3D photo-electronics, optical computations, and more.

## CHAPTER 6 PERFORMANCE ENHANCED FLEXIBLE NANO-MEMORY DEVICE

### 6.1. Introduction

Up to date, memory devices such as flash memory devices or mass storage devices like magnetic hard disks have improved greatly over the past several decades no matter in academic field or industrial application.<sup>139, 140</sup> However, with the development of new technology and high demand in multiple purpose applications, especially like to have memory device with flexible characteristic for special applications like robots, implantable intellectual system, biosensing system, etc, our current memory devices with rigid silicon substrate obviously don't satisfy the requirements.<sup>141, 142</sup> Thus, it is urgent to develop novel flexible memory device. Nevertheless, although some resistive memory devices based on flexible substrates have been reported<sup>143-149</sup>, there are coming with amount of drawbacks like low memory density, slow switching speed, and poor reliability that need more improvements. Meanwhile, numerous devices based on 1D nanomaterials have been created recently demonstrating unique capabilities for developing next generation electronic memory and switching devices that go beyond the conventional inherent limitations.<sup>150-154</sup> In particular, our previous publication introduced a study that the screening polar charges induce electric hysteresis loop in a Schottky-Ohmic contacted ZnO NW/MW memory device, which makes it possible to fabricate new logic circuits and memory devices on ultra-flexible substrate with ultrahigh storage density due to the size of the NWs both in diameter and length, and fast data storage/erasing by working at high frequency up to GHz theoretically because of Schottky barrier.<sup>7</sup>

Herein in this work, we introduced a nano-memory device with ultra-thin flexible substrate that works under a totally novel memory mechanism of asymmetric Schottky-semiconductor-Ohmic contacts and polar charges screening effect. The device is made of single crystal ZnO NR arrays on ultra-thin flexible substrate. A detailed memory performance analysis of the device including AC I-V curve, write-read-ease-read pulse test, endurance characteristics, time retention test and cumulative probability was conducted, and followed by the flexibility and reliability under various bending tests. All presented results demonstrated the superiority of this flexible nano-memory device in memory performance and mechanical stability. Furthermore, simulation and theoretical calculation were carried out to prove that mechanical deformation on the flexible nano-memory device will increase the performance a little instead of deteriorating, stemming from the unique characteristic of polar charges screening effect memory mechanism. This discovery provides an alternative path to create new flexible memory device with high-density, fast writing/erasing data storage capacity and ultra-flexible for next generation in biomedical applications.

## 6.2. Device fabrication

As schematically described in Figure 6.1(a), the memory device with an ultra-thin flexible substrate is proposed with architecture design of 3D nanostructures in order to fully use the benefits of nanostructure and newly found memory mechanism. It is made of single crystal ZnO NR arrays on the ultra-thin flexible substrate, there is a very thin metal layer between NR arrays and substrate as conductive contact, the top is usually gold electrode that has fully capped each NR array to form the basic memory unit, and the additional isolation layer is filled between top-bottom electrode to avoid forming short circuit. The optical image inset in Figure 6.1(a) shows

the prototype device. Figure 6.1(b) and (c) present the device under compressive and tensile bending conditions, which provides the merit of high flexibility of our device.

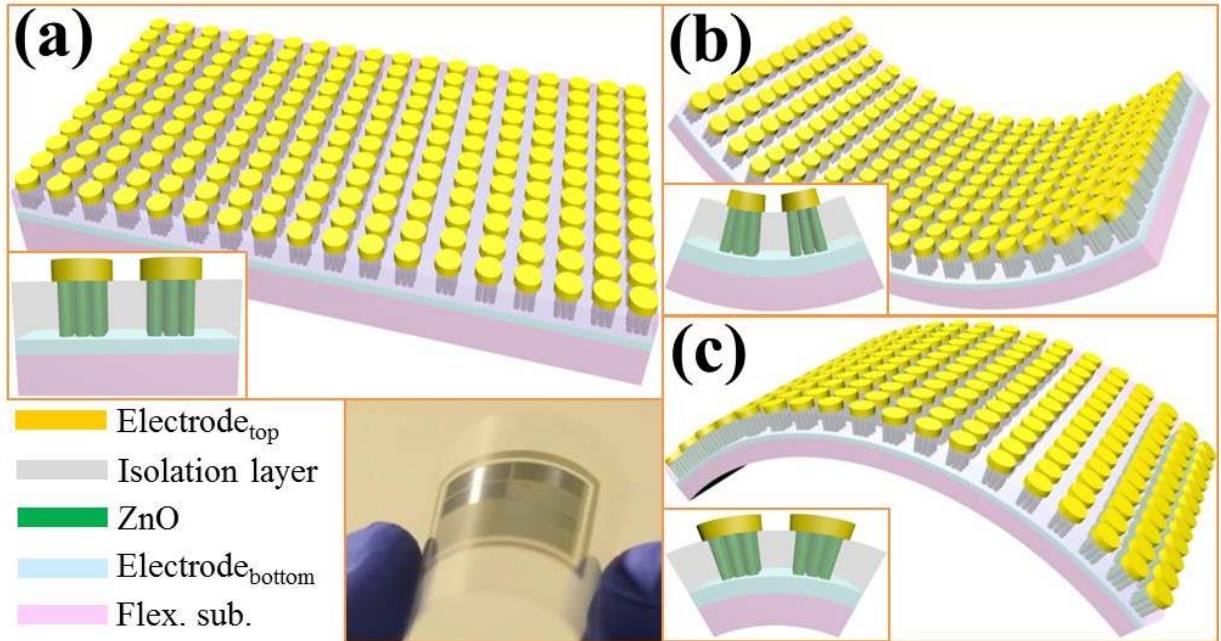


**Figure 6.1.** (a) Schematic diagram of the architecture design of the flexible nano-memory device. (b) The illustration of the device under compressive bending. (c) The illustration of the device under tensile bending.

### 6.3. Results and discussion

#### 6.3.1. Morphology characterization

Figure 6.2(a) shows the patterned single crystal ZnO NR arrays grown on a flexible substrate, each floor-like unit has a width of 2  $\mu\text{m}$ , and they are uniformly distributed on the substrate. SEM images in Figure 6.2(b) show the top surface of the device, the optical image in Figure 6.1(c) shows the basic units of the flexible nano-memory device, ZnO NR arrays' head are covered with gold electrodes, and there is a transparent isolative layer between top and bottom electrodes.

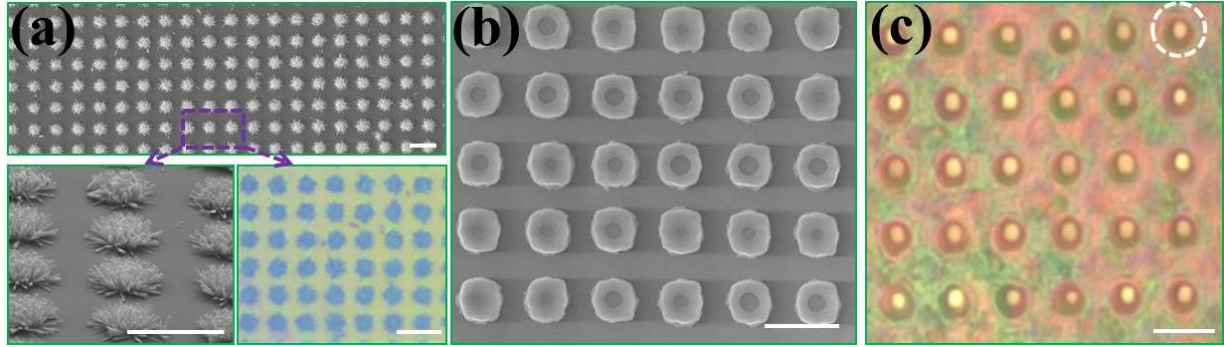


**Figure 6.2.** (a) SEM images of the ZnO NR arrays grown on the flexible substrate (right lower inset is the optical image). (b) SEM images of the top morphology of the as-fabricated device. (c) Optical image of gold topped nano-memory device (scale bar is 5  $\mu\text{m}$ ).

### 6.3.2. Memory characteristics

A typical I-V characteristics of as prepared nano-memory device acquired at 150 Hz is shown in Figure 6.3(a), which were fabricated with ZnO NR arrays as active layers with gold top and bottom aluminum electrodes. As can be seen in the figure, Reversible bistable resistance switching between a HRS (i.e., OFF state) and a LRS (i.e., OFF state) was observed. The device initially exhibits an OFF state when a negative voltage applied, after reaching a certain reversed voltage, the device undergoes the “SET” process in the memory storage operation, then the current abruptly increases to  $2 \times 10^{-8}$  A around -4.5 V, which indicates the device reached switching resistance state from OFF to ON state. Once the device has reached the ON state, it remains there. The device is capable of being switched to OFF state by the application of a forward voltage sweeping, after reaching a certain positive voltage, the device undergoes the “RESET” process in the memory storage operation, then the current abruptly decreases to  $3 \times 10^{-10}$  A around 1 V, indicating that the device undergoes a sharp electrical transition from the ON state to the OFF state. The ON/OFF current ratios of the devices depend on the level of the reading voltage, a lower reading voltage results in a higher ON/OFF current ratio. These results indicate that the memory device unit based on ZnO NR arrays exhibits excellent unipolar ON

and OFF switching behavior in the device. Figure 6.3(b) shows the corresponding band diagram of basic memory unit consisting of a ZnO NR embedded by gold and aluminum electrodes on both ends, in consideration of the work function of the metal electrode and the electron affinity of ZnO, an asymmetric Schottky-ZnO-Ohmic contact would be formed to induce the electric hysteresis loop, which is another essential condition for the appearance of electric hysteresis. We further investigated the devices' ability to write, read, and erase data, which is required for the production of memory devices. Figure 6.3(c) presents a representative result of write-read-erase cycle tests conducted on the devices for several hours, which was measured for a memory device based on ZnO NR arrays with Au and Al electrodes. In the write-read-erase cycle, the "write" is made by applying a negative voltage pulse whose amplitude (-5 V) is higher than the  $V_{\text{read}}(\text{ON})$ , and the "erase" is achieved through erasing the ON state by applying a positive voltage pulse with an amplitude (5.0 V) higher than the  $V_{\text{read}}(\text{OFF})$  (the upper part of Figure 6.3(c)). A small probe voltage (2 V) pulse is employed to read the ON and OFF states of the device. As can be seen in the lower part of Figure 6.3(c), the device current changes with the voltages applied during the write-read-erase cycle. The probe current in the ON state is several orders of magnitude higher than that in the OFF state. The device has been cycled such write-read-erase operation many times as shown in Figure 6.3(c). These results confirm that the devices have excellent rewritability for memory device applications. Endurance and retention tests of the flexible nano-memory devices were systematically performed. Figure 6.3(d) shows the current values of the flexible nano-memory devices with 100 cycling endurance tests under repeated write-read(ON)-erase-read(OFF) pulses and read at 2 V. Obviously, there is no decay for current values under both states during 100 repeated switching cycles measurements. In order to confirm the data storage ability in both states further, the retention characteristics of the flexible nano-

memory device under ambient conditions was investigated as shown in Figure 6.3(e). As can be seen in the figure, both the ON and OFF state can retain without any degradation for  $10^4$  second and even longer. Apparently, this flexible memory unit exhibited a stable retention property up to

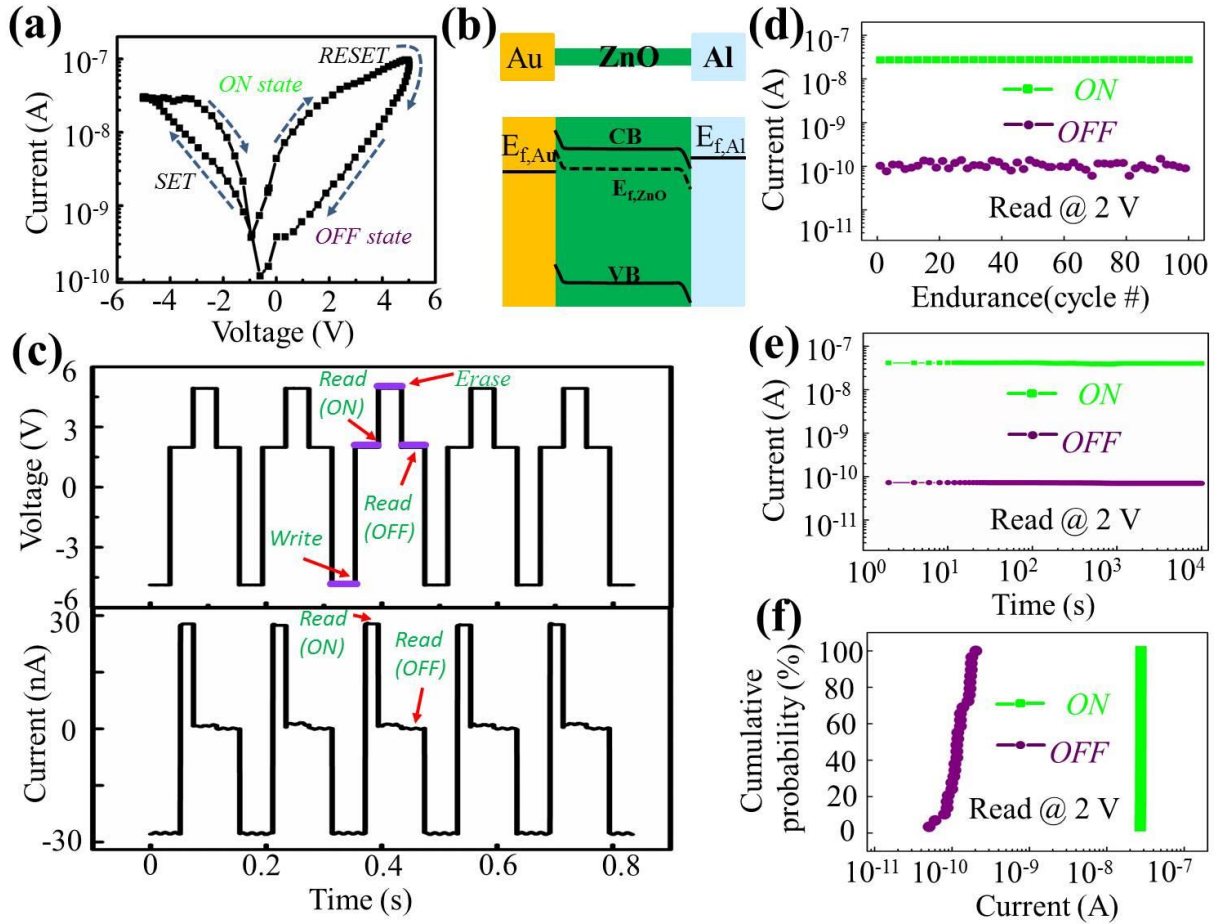


**Figure.6.3.** Memory characteristics of the flexible nano-memory device. (a) Typical I-V curve of the device plotted on a semilogarithmic scale. (b) The band diagram of the nano-memory unit showing an asymmetric Schottky-semiconductor-Ohmic contact. (c) Write-read-erase cycles of the nano-memory device. The top and bottom curves are the applied voltage and the corresponding current response, respectively. The ON-state has been induced by 'write' at -5 V, while the OFF-state has been reinstated by 'erase' at 5 V. Between switching the states ('read') have been probed by device current under 2 V. (d) Endurance characteristics of the nano-memory device during 100 repeated cycles with the readout voltage is 2 V. (e) Time retention test of the nano-memory device on the plastic substrate. (f) Cumulative probability of current state distributions from 50 different units.

at least  $10^4$  s at room temperature, ensuring excellent reliability of the flexible nano-memory devices on the plastic substrate. To demonstrate the reproducibility and uniformity of the flexible

nano-memory devices during switching operations, 50 different were chosen and analyzed statistically. The cumulative probability distribution data in Figure 6.3(f) shows highly uniform distributions of both ON state and OFF state at the read voltage (purple circles for OFF, green circles for ON). The ratio between ON and OFF values was maintained without current overlap at the reading voltage of 2.0 V.

### 6.3.3. Bending test

Next, we evaluated the flexibility of the present flexible nano-memory device under various bending conditions on a bending stage machine. As shown in Figure 6.4(a), we measured current at the ON and OFF state in situ while the device was gradually bent. Figure 6.4(b) shows the collected currents as a function of bending radius ranging from 50 mm to 10 mm, or corresponding strain from 0.1% to 0.5%. Similar to endurance and retention tests, the readout voltage chose 2 V. Both of the ON (green squares) and OFF (purple circles) state currents were kept stable without any degradations regardless of bending. To examine the mechanical reliability of the device, we further statistically analyzed the performance of flexible nano-memory device with 1000 bending cycles and at a fixed bending radius of 10 mm to take current measurements. As shown in Figure 6.4(c), in both ON and OFF state currents showed a consistent and constant  $I_{ON}/I_{OFF}$  ratio with negligible fluctuations even up to 1000 bending cycles, indicating the excellent stability and flexibility characters of the flexible nano-memory devices for retaining memory function regardless of the magnitude or change of the bending radius during the mechanical durability test, which strongly prove that our flexible nano-memory device is highly stable and compatible with flexible electronic applications.

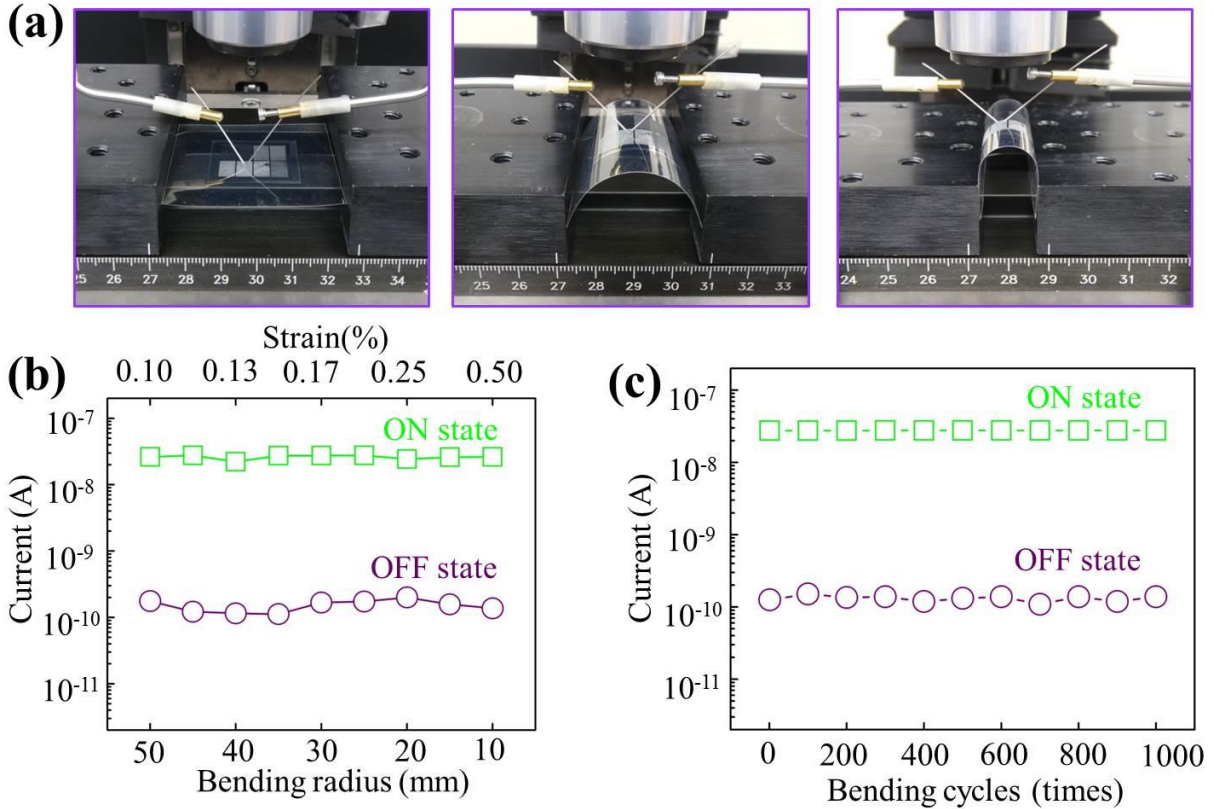


**Figure 6.4.** (a) Photograph of the device in bending and unbending states on a bending stage machine. (b) “ON” and “OFF” state currents as a function of curvature radius. The data is collected from I-V curves performed at each curvature radius. (c) “ON” and “OFF” currents as a function of bending cycles. Bending radius of 10 mm is utilized. The data is collected from I-V curves performed at each bending cycles.

#### 6.3.4. Performance enhanced mechanism

As indicated in the memory test and previous publication<sup>7</sup>, the mechanism for memory devices is due to the polar surfaces of ZnO NW/MW, especially the top-end polar surface of the NR is responsible for the memory formation. As the wurtzite structure schematically shown in Figure 6.5(a), Stack layers of  $Zn^{2+}$  and  $O^{2-}$  build the wurtzite ZnO. Owing to the unique wurtzite crystal structure of ZnO, strong polar surfaces form at the two ends of the single crystal ZnO NR grown along c-axis direction and are terminated with  $Zn^{2+}$  cations and  $O^{2-}$  anions, respectively. In this case, an internal electrical field along c-direction will be generated between both top and bottom polar surfaces. At ambient environment and without external bias, the polar surfaces are likely to

be screened or neutralized by surface adsorbents to keep charge neutrality, so that in ZnO-Au contact, the free electrons from Au will migrate to interface and screen the polar charges in a very short time. With the applied bias in a circuit, if the applied electric field is large enough, it can easily drive the electrons away from the contact interface of Au and ZnO, but the polar charges are still there. In such a scenario, the transient current depends on both the applied electric field and the previous polar charges remaining. As to I-V characterization, it induces a hysteresis loop under fast applied potential switching. Thus, the function of this memory device in the circuit can be described as the combination of resistor, Schottkey diode and electrons reservoir as shown in lower part of Figure 6.5(a), which is similar to the operation mechanism of random-access memory. Figure 6.5(b) gives the illustration of flexible nano-memory device under tensile stress and the corresponding volumetric strain distribution when it is bent. Obviously, plastic isolation layer and flexible substrate absorbed the main deformation energy, the stress/strain effect on the ZnO NRs and electrodes were negligible, because the elastic moduli of other materials are not comparable to that of ZnO, and metals like gold and aluminum has a good ductility. Similarly, when the flexible nano-memory device is under compressive bending, it will achieve the same result. As shown in Figure 6.5(c), when the ZnO is compressed in the c- direction although the strain is very small, it may still affect the polar charges on the end terminals. Presumably more  $\text{Zn}^{2+}$  ions are exposed to the surface and increase the screen charges correspondingly after bending, resulting in the increase of total electric field inside the ZnO by adding the polarization electric field a little bit. Furthermore, this raise of electric field will slightly increase the hysteresis loop size as presented in Figure 6.5(d), which means the mechanical deformation on our flexible nano-memory devices will not deteriorate the performance rather than increase a little bit due to polar charges memory mechanism. By

considering analysis above, we can achieve a conclusion that this flexible nano-memory device possesses unprecedented merits of both no damage protections from device architecture design and performance stability due to the unique memory mechanism.

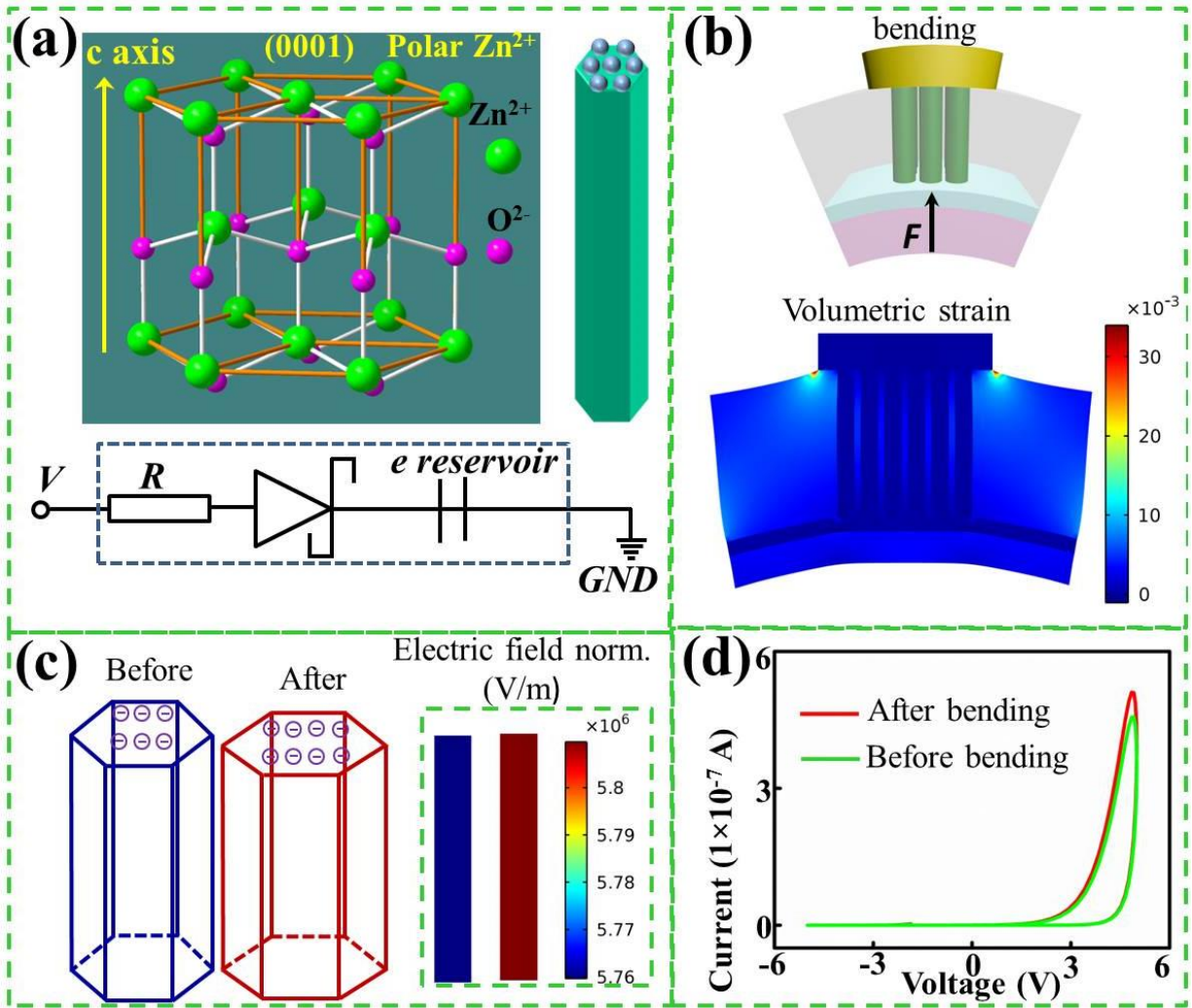


**Figure 6.5.** (a) Crystal structure of wurtzite ZnO. The top end with Zn<sup>2+</sup> ion layer attracting free electrons. Lower part is the digital circuit of flexible nano-memory unit. (b) Illustration of device under bending and related volumetric strain distribution of the device by COMSOL Multiphysics. (c) schematic diagram of device after bending, causing a slight increase of electric field in nano-memory unit by COMSOL Multiphysics simulation after bend. (d) Calculation of corresponding I-V curves before and after bending, showing a little bit larger hysteresis loop after bend.

#### 6.4. Conclusions

In summary, a novel flexible nano-memory device based on ZnO NR arrays has been successfully fabricated and investigated, which has unique memory mechanism of NR polar surface induced I-V hysteresis loop. By taking the advantage of 3D nanostructures, this flexible nano-memory device demonstrates high-density with memory unit size down to nanoscale and ultrafast operation speed up to gigahertz. Furthermore, the unique structure of NR bundle memory unit and soft substrate enable the entire device ultra-flexible for realizing fully flexible memory technique.

## CHAPTER 7 CONCLUSIONS AND FUTURE WORK

### 7.1. Conclusions

In this dissertation, a comprehensive study on the flexible nano-memory device by semiconducting ZnO NR arrays has been performed, which covers the basic nanomaterial synthesis, related nano-properties characterization, and the design and performance evaluation of nano-memory device with flexibility.

Starting with the synthesis methodologies of 1D ZnO NW/NR, a detailed study in the role of the substrate roughness in ZnO NW arrays hydrothermal growth shows that average diameters and number densities of ZnO NW arrays are inversely proportional to the increasing substrate roughness. Furthermore, the nucleation theory based on the Gibbs free energy reveals the relations that substrate roughness versus average NW diameter, NW number density matched well with experimental results. By fully understanding this key factor and combining other already known parameters, like growth temperature, precursor concentration, solution PH value and substrate, it is possible to precisely control synthesis of ZnO NR/NW so as to provide desired nanomaterials and nanostructures for fabricating flexible nano-memory device.

Intrinsic electrical property characterizations of 1D ZnO MB/NB by C-AFM show that the resistance of the single crystalline ZnO MB/NB is exponentially dependent on the length of the MB/NB, which is well interpreted and fitted by a simple model based on the anisotropic velocity of the carries in the crystal planes. This nonlinear length dependent electrical resistance in the semiconducting single crystal MB/NB is significantly different with the bulk ZnO. Further FEM simulations verify the results and make it possible to identify the crystal growth direction of

single crystal semiconducting or crystallography of the anisotropic semiconducting nanomaterial easily. Understanding such property could definitely improve the design and the performance of flexible nano-memory devices.

When nanomaterials with a height-diameter ratio are in between 0D and 1D, its photoelectric properties do not obey Ohm's law for the additional nanoconfinement from the third dimension. Systematic investigation via two independent techniques of C-AFM direct I-V acquisition and SKPM surface potential mapping shows that photoelectric property of 0.5D semiconducting nanomaterials changes as a function of illumination light intensity and materials geometry, behaviors of which apparently differ from the bulk/micro/1D nanomaterial counterparts. A proposed model by considering surface effect, quantum effect, and illumination effect fits the experimental results very well and further can accurately predict the photoelectric characteristics of 0.5D semiconducting nanomaterials.

Rely on those solid fundamental studies, a flexible nano-memory device based on ZnO NR arrays is fabricated via wet chemical growth, which has unique memory mechanism by NR polar surface induced I-V hysteresis loop. Nano-memory device has high-density with memory unit size of nanoscale and ultrafast operation speed up to gigahertz. More important, the unique NR bundle memory unit structure enables the entire device ultra-flexible for realized fully-flexible memory technique.

## 7.2. Future work

There are still many related research need to be further carried out.

1. The achieved flexible nano-memory device is made of bundles of flower-like ZnO NR arrays. It can be predicted that device with well-aligned single NR arrays will have better performance.

2. Research presented here is limited by individual and separated nano-memory units, which is still hard to be directly used in integrated circuit for memory function. Engineering design and integration about top and bottom electrodes for addressing memory units would be performed for real application of the nano-memory device.

3. It is expected to extend the flexible nano-memory devices design to other materials and other stretchable substrates, which can broaden the applications in and biomedical and other fields.

## REFERENCES

- [1]. Hu, J. T.; Ouyang, M.; Yang, P. D.; Lieber, C. M. Controlled growth and electrical properties of heterojunctions of carbon nanotubes and silicon nanowires. *Nature* 1999, 399, 48-51.
- [2]. Wang, J. F.; Gudiksen, M. S.; Duan, X. F.; Cui, Y.; Lieber, C. M. Highly polarized photoluminescence and photodetection from single indium phosphide nanowires. *Science* 2001, 293, 1455-1457.
- [3]. Tang, C. L.; Jiang, C. M.; Lu, W. Q.; Song, J. H. Nonlinear length dependent electrical resistance of a single crystal zinc oxide micro/nanobelt. *Phys. Chem. Chem. Phys.* 2013, 15, 8222-8227.
- [4]. Fu, Z. D.; Cui, Y. S.; Zhang, S. Y.; Chen, J.; Yu, D. P.; Zhang, S. L.; Niu, L.; Jiang, J. Z. Study on the quantum confinement effect on ultraviolet photoluminescence of crystalline ZnO nanoparticles with nearly uniform size. *Appl. Phys. Lett.* 2007, 90, 263113.
- [5]. Dong, Y. J.; Yu, G. H.; McAlpine, M. C.; Lu, W.; Lieber, C. M. Si/a-Si core/shell nanowires as nonvolatile crossbar switches. *Nano Lett.* 2008, 8, 386-391.
- [6]. Standley, B.; Bao, W. Z.; Zhang, H.; Bruck, J.; Lau, C. N.; Bockrath, M. Graphene-Based Atomic-Scale Switches. *Nano Lett.* 2008, 8, 3345-3349.
- [7]. Song, J. H.; Zhang, Y.; Xu, C.; Wu, W. Z.; Wang, Z. L. Polar Charges Induced Electric Hysteresis of ZnO Nano/Microwire for Fast Data Storage. *Nano Lett.* 2011, 11, 2829-2834.
- [8]. [http://en.wikipedia.org/wiki/Flash\\_memory](http://en.wikipedia.org/wiki/Flash_memory)
- [9]. [http://en.wikipedia.org/wiki/Hard\\_disk\\_drive](http://en.wikipedia.org/wiki/Hard_disk_drive)
- [10]. Pearton, S. J.; Norton, D. P.; Ip, K.; Heo, Y. W.; Steiner, T. Recent progress in processing and properties of ZnO. *Prog. Mater. Sci.* 2005, 50, 293-340.
- [11]. Lyu, S. C.; Zhang, Y.; Ruh, H.; Lee, H. J.; Shim, H. W.; Suh, E. K.; Lee, C. J. Low temperature growth and photoluminescence of well-aligned zinc oxide nanowires. *Chem. Phys. Lett.* 2002, 363, 134-138.
- [12]. Xu, L. F.; Guo, Y.; Liao, Q.; Zhang, J. P.; Xu, D. S. Morphological control of ZnO nanostructures by electrodeposition. *J. Phys. Chem. B* 2005, 109, 13519-13522.

- [13]. Mahalingam, T.; Lee, K. M.; Park, K. H.; Lee, S.; Ahn, Y.; Park, J.-Y.; Koh, K. H. Low temperature wet chemical synthesis of good optical quality vertically aligned crystalline ZnO nanorods. *Nanotechnology* 2007, 18, 035606.
- [14]. Xu, S.; Wang, Z. L. One-dimensional ZnO nanostructures: Solution growth and functional properties. *Nano Res.* 2011, 4, 1013-1098.
- [15]. Yang, P. D.; Yan, H. Q.; Mao, S.; Russo, R.; Johnson, J.; Saykally, R.; Morris, N.; Pham, J.; He, R. R.; Choi, H. J. Controlled growth of ZnO nanowires and their optical properties. *Adv. Funct. Mater.* 2002, 12, 323-331.
- [16]. Versteegh, M. A. M.; Vanmaekelbergh, D.; Dijkhuis, J. I. Room-Temperature Laser Emission of ZnO Nanowires Explained by Many-Body Theory. *Physical Review Letters* 2012, 108, 157402.
- [17]. Bercu, B.; Geng, W.; Simonetti, O.; Kostcheev, S.; Sartel, C.; Sallet, V.; Lerondel, G.; Molinari, M.; Giraudet, L.; Couteau, C. Characterizations of Ohmic and Schottky-behaving contacts of a single ZnO nanowire. *Nanotechnology* 2013, 24, 415202.
- [18]. Li, M.; Zhang, H. Y.; Guo, C. X.; Xu, J. B.; Fu, X. J. The research on suspended ZnO nanowire field-effect transistor. *Chinese Phys. B* 2009, 18, 1594-1597.
- [19]. Sun, B. Q.; Siringhaus, H. Surface tension and fluid flow driven self-assembly of ordered ZnO nanorod films for high-performance field effect transistors. *J. Am. Chem. Soc.* 2006, 128, 16231-16237.
- [20]. Ju, S. Y.; Facchetti, A.; Xuan, Y.; Liu, J.; Ishikawa, F.; Ye, P. D.; Zhou, C. W.; Marks, T. J.; Janes, D. B. Fabrication of fully transparent nanowire transistors for transparent and flexible electronics. *Nat. Nanotechnol.* 2007, 2, 378-384.
- [21]. Chen, X.; Mao, S. S. Titanium dioxide nanomaterials: Synthesis, properties, modifications, and applications. *Chem. Rev.* 2007, 107, 2891-2959.
- [22]. Xia, Y. N.; Yang, P. D.; Sun, Y. G.; Wu, Y. Y.; Mayers, B.; Gates, B.; Yin, Y. D.; Kim, F.; Yan, Y. Q. One-dimensional nanostructures: Synthesis, characterization, and applications. *Adv. Mater.* 2003, 15, 353-389.
- [23]. Fan, Z. Y.; Lu, J. G. Zinc oxide nanostructures: Synthesis and properties. *J. Nanosci. Nanotechnol.* 2005, 5, 1561-1573.
- [24]. Greene, L. E.; Law, M.; Tan, D. H.; Montano, M.; Goldberger, J.; Somorjai, G.; Yang, P. D. General route to vertical ZnO nanowire arrays using textured ZnO seeds. *Nano Lett.* 2005, 5, 1231-1236.
- [25]. Park, W. I.; Yi, G. C.; Kim, M. Y.; Pennycook, S. J. ZnO nanoneedles grown vertically on Si substrates by non-catalytic vapor-phase epitaxy. *Adv. Mater.* 2002, 14, 1841-1843.

- [26]. Laudise, R. A.; Ballman, A. A. Hydrothermal Synthesis of Zinc Oxide and Zinc Sulfide. *J. Phys. Chem.* 1960, 64, 688-691.
- [27]. Zeng, H. B.; Cui, J. B.; Cao, B. Q.; Gibson, U.; Bando, Y.; Golberg, D. Electrochemical Deposition of ZnO Nanowire Arrays: Organization, Doping, and Properties. *Sci. Adv. Mater.* 2010, 2, 336-358.
- [28]. Pan, Z. W.; Dai, Z. R.; Wang, Z. L. Nanobelts of semiconducting oxides. *Science* 2001, 291, 1947-1949.
- [29]. Heo, Y. W.; Varadarajan, V.; Kaufman, M.; Kim, K.; Norton, D. P.; Ren, F.; Fleming, P. H. Site-specific growth of ZnO nanorods using catalysis-driven molecular-beam epitaxy. *Appl. Phys. Lett.* 2002, 81, 3046-3048.
- [30]. Sun, Y.; Fuge, G. M.; Ashfold, M. N. R. Growth of aligned ZnO nanorod arrays by catalyst-free pulsed laser deposition methods. *Chem. Phys. Lett.* 2004, 396, 21-26.
- [31]. Xu, S.; Lao, C.; Weintraub, B.; Wang, Z. L. Density-controlled growth of aligned ZnO nanowire arrays by seedless chemical approach on smooth surfaces. *J. Mater. Res.* 2008, 23, 2072-2077.
- [32]. Amin, G.; Asif, M. H.; Zainelabdin, A.; Zaman, S.; Nur, O.; Willander, M. Influence of pH, Precursor Concentration, Growth Time, and Temperature on the Morphology of ZnO Nanostructures Grown by the Hydrothermal Method. *J. Nanomater.* 2011, 269692.
- [33]. Qin, Y.; Yang, R. S.; Wang, Z. L. Growth of Horizontal ZnO Nanowire Arrays on Any Substrate. *J. Phys. Chem. C* 2008, 112, 18734-18736.
- [34]. Andriotis, A. N.; Menon, M.; Chernozatonskii, L. Nonlinear resistance dependence on length in single-wall carbon nanotubes. *Nano Lett.* 2003, 3, 131-134.
- [35]. Blomers, C.; Lu, J. G.; Huang, L.; Witte, C.; Grutzmacher, D.; Luth, H.; Schapers, T. Electronic Transport with Dielectric Confinement in Degenerate InN Nanowires. *Nano Lett.* 2012, 12, 2768-2772.
- [36]. Wang, X. D.; Song, J. H.; Wang, Z. L. Nanowire and nanobelt arrays of zinc oxide from synthesis to properties and to novel devices. *J. Mater. Chem.* 2007, 17, 711-720.
- [37]. Jiang, C.; Song, J. Significant Photoelectric Property Change Caused by Additional Nano-confinement: A Study of Half-Dimensional Nanomaterials. *Small* 2014, 10, 5042-5046.
- [38]. Jiang, C. M.; Lu, W. Q.; Song, J. H. Shear Modulus Property Characterization of Nanorods. *Nano Lett.* 2013, 13, 111-115.
- [39]. Yu, G.; Tang, C.; Song, J.; Lu, W. Physical model construction for electrical anisotropy of single crystal zinc oxide micro/nanobelt using finite element method. *Applied Physics Letters* 2014, 104, 153109.

- [40]. Kind, H.; Yan, H. Q.; Messer, B.; Law, M.; Yang, P. D. Nanowire ultraviolet photodetectors and optical switches. *Adv. Mater.* 2002, 14, 158-160.
- [41]. Huang, C. T.; Song, J. H.; Tsai, C. M.; Lee, W. F.; Lien, D. H.; Gao, Z. Y.; Hao, Y.; Chen, L. J.; Wang, Z. L. Single-InN-Nanowire Nanogenerator with Upto 1 V Output Voltage. *Adv. Mater.* 2010, 22, 4008-4013.
- [42]. Chang, H.; Tsai, M. H. Synthesis and characterization of ZnO nanoparticles having prism shape by a novel gas condensation process. *Reviews on Advanced Materials Science* 2008, 18, 736-745.
- [43]. Stankovich, S.; Piner, R. D.; Chen, X. Q.; Wu, N. Q.; Nguyen, S. T.; Ruoff, R. S. Stable aqueous dispersions of graphitic nanoplatelets via the reduction of exfoliated graphite oxide in the presence of poly(sodium 4-styrenesulfonate). *J. Mater. Chem.* 2006, 16, 155-158.
- [44]. Busbee, B. D.; Obare, S. O.; Murphy, C. J. An Improved Synthesis of High-Aspect-Ratio Gold Nanorods. *Adv. Mater.* 2003, 15, 414-416.
- [45]. Wang, Z. L.; Song, J. H. Piezoelectric nanogenerators based on zinc oxide nanowire arrays. *Science* 2006, 312, 242-246.
- [46]. Xi, Y.; Song, J.; Xu, S.; Yang, R.; Gao, Z.; Hu, C.; Wang, Z. L. Growth of ZnO nanotube arrays and nanotube based piezoelectric nanogenerators. *J. Mater. Chem.* 2009, 19, 9260-9264.
- [47]. Wang, X. D.; Song, J. H.; Wang, Z. L. Single-crystal nanocastles of ZnO. *Chem. Phys. Lett.* 2006, 424, 86-90.
- [48]. Ko, S. H.; Lee, D.; Kang, H. W.; Nam, K. H.; Yeo, J. Y.; Hong, S. J.; Grigoropoulos, C. P.; Sung, H. J. Nanoforest of Hydrothermally Grown Hierarchical ZnO Nanowires for a High Efficiency Dye-Sensitized Solar Cell. *Nano Lett.* 2011, 11, 666-671.
- [49]. Caddeo, C.; Mallocci, G.; De Angelis, F.; Colombo, L.; Mattoni, A. Optoelectronic properties of (ZnO)<sub>60</sub> isomers. *Phys. Chem. Chem. Phys.* 2012, 14, 14293-14298.
- [50]. Song, J. H.; Xie, H. Z.; Wu, W. Z.; Joseph, V. R.; Wu, C. F. J.; Wang, Z. L. Robust optimization of the output voltage of nanogenerators by statistical design of experiments. *Nano Res.* 2010, 3, 613-619.
- [51]. Wang, H. L.; Dai, H. J. Strongly coupled inorganic-nano-carbon hybrid materials for energy storage. *Chem. Soc. Rev.* 2013, 42, 3088-3113.
- [52]. Chang, J. A.; Rhee, J. H.; Im, S. H.; Lee, Y. H.; Kim, H. J.; Seok, S. I.; Nazeeruddin, M. K.; Gratzel, M. High-Performance Nanostructured Inorganic-Organic Heterojunction Solar Cells. *Nano Lett.* 2010, 10, 2609-2612.

- [53]. Li, F.; Ding, Y.; Gao, P.; Xin, X.; Wang, Z. L. Single-Crystal Hexagonal Disks and Rings of ZnO: Low-Temperature, Large-Scale Synthesis and Growth Mechanism. *Angewandte Chemie*. 2004, 116, 5350-5354.
- [54]. Chiang, I. C.; Chen, D. H. Preparation and Photoluminescence of ZnO Nanocrystals by a High-temperature Organometallic Route. *Chem. Lett.* 2008, 37, 928-929.
- [55]. Wang, L. S.; Zhang, X. Z.; Zhao, S. Q.; Zhou, G. Y.; Zhou, Y. L.; Qi, J. J. Synthesis of well-aligned ZnO nanowires by simple physical vapor deposition on c-oriented ZnO thin films without catalysts or additives. *Applied Physics Letters* 2005, 86, 024108.
- [56]. Huang, M. H.; Mao, S.; Feick, H.; Yan, H. Q.; Wu, Y. Y.; Kind, H.; Weber, E.; Russo, R.; Yang, P. D. Room-temperature ultraviolet nanowire nanolasers. *Science* 2001, 292, 1897-1899.
- [57]. Law, M.; Greene, L. E.; Johnson, J. C.; Saykally, R.; Yang, P. D. Nanowire dye-sensitized solar cells. *Nat. Mater.* 2005, 4, 455-459.
- [58]. Fang, H.; Wu, W. Z.; Song, J. H.; Wang, Z. L. Controlled Growth of Aligned Polymer Nanowires. *J. Phys. Chem. C* 2009, 113, 16571-16574.
- [59]. Li, S.; Zhang, X. Z.; Yan, B.; Yu, T. Growth mechanism and diameter control of well-aligned small-diameter ZnO nanowire arrays synthesized by a catalyst-free thermal evaporation method. *Nanotechnology* 2009, 20, 495604.
- [60]. Lu, W. Q.; Jiang, C. M.; Caudle, D.; Tang, C. L.; Sun, Q.; Xu, J. J.; Song, J. H. Controllable growth of laterally aligned zinc oxide nanorod arrays on a selected surface of the silicon substrate by a catalyst-free vapor solid process - a technique for growing nanocircuits. *Phys. Chem. Chem. Phys.* 2013, 15, 13532-13537.
- [61]. Song, J. H.; Wang, X. D.; Riedo, E.; Wang, Z. L. Systematic study on experimental conditions for large-scale growth of aligned ZnO nanowires on nitrides. *J. Phys. Chem. B* 2005, 109, 9869-9872.
- [62]. Kim, J. Y.; Cho, J. W.; Kim, S. H. The characteristic of the ZnO nanowire morphology grown by the hydrothermal method on various surface-treated seed layers. *Mater. Lett.* 2011, 65, 1161-1164.
- [63]. Bin Lee, J.; Kwak, S. H.; Kim, H. J. Effects of surface roughness of substrates on the c-axis preferred orientation of ZnO films deposited by r.f. magnetron sputtering. *Thin Solid Films* 2003, 423, 262-266.
- [64]. Yoshino, Y.; Inoue, K.; Takeuchi, M.; Makino, T.; Katayama, Y.; Hata, T. Effect of substrate surface morphology and interface microstructure in ZnO thin films formed on various substrates. *Vacuum* 2000, 59, 403-410.

- [65]. Kim, Y. J.; Yoo, J.; Kwon, B. H.; Hong, Y. J.; Lee, C. H.; Yi, G. C. Position-controlled ZnO nanoflower arrays grown on glass substrates for electron emitter application. *Nanotechnology* 2008, 19, 315202.
- [66]. Jiang, C. Y.; Sun, X. W.; Lo, G. Q.; Kwong, D. L.; Wang, J. X. Improved dye-sensitized solar cells with a ZnO-nanoflower photoanode. *Applied Physics Letters* 2007, 90, 263501.
- [67]. Shi, R. X.; Yang, P.; Zhang, S.; Dong, X. B. Growth of flower-like ZnO on polyhedron CuO fabricated by a facile hydrothermal method on Cu substrate. *Ceram. Int.* 2014, 40, 3637-3646.
- [68]. Wang, Q.-H.; Tang, C.-L.; Jiang, C.-M.; Du, D.-F.; Wang, F.; Song, J.-H. Role of Substrate Roughness in ZnO Nanowire Arrays Growth by Hydrothermal Approach. *Acta Metallurgica Sinica (English Letters)* 2016, 29, 237-242.
- [69]. Han, Y. G.; Yu, X. G.; Wang, D.; Yang, D. R. Formation of Various Pyramidal Structures on Monocrystalline Silicon Surface and Their Influence on the Solar Cells. *J. Nanomater.* 2013, 716012.
- [70]. Choudhury, B. D.; Abedin, A.; Dev, A.; Sanatinia, R.; Anand, S. Silicon micro-structure and ZnO nanowire hierarchical assortments for light management. *Opt. Mater. Express* 2013, 3, 1039-1048.
- [71]. Greene, L. E.; Yuhas, B. D.; Law, M.; Zitoun, D.; Yang, P. D. Solution-grown zinc oxide nanowires. *Inorg. Chem.* 2006, 45, 7535-7543.
- [72]. Swain, P. S.; Lipowsky, R. Contact angles on heterogeneous surfaces: A new look at Cassie's and Wenzel's laws. *Langmuir* 1998, 14, 6772-6780.
- [73]. Zhang, Y.; Wang, M.; Lin, X.; Huang, W. D. Effect of Substrate Surface Microstructure on Heterogeneous Nucleation Behavior. *J. Mater. Sci. Technol.* 2012, 28, 67-72.
- [74]. Laurenti, M.; Cauda, V.; Gazia, R.; Fontana, M.; Rivera, V. F.; Bianco, S.; Canavese, G. Wettability Control on ZnO Nanowires Driven by Seed Layer Properties. *Eur. J. Inorg. Chem.* 2013, 2520-2527.
- [75]. Balkenende, A. R.; van de Boogaard, H. J. A. P.; Scholten, M.; Willard, N. P. Evaluation of different approaches to assess the surface tension of low-energy solids by means of contact angle measurements. *Langmuir* 1998, 14, 5907-5912.
- [76]. Liu, X.; Wu, X. H.; Cao, H.; Chang, R. P. H. Growth mechanism and properties of ZnO nanorods synthesized by plasma-enhanced chemical vapor deposition. *J. Appl. Phys.* 2004, 95, 3141-3147.
- [77]. Polsongkram, D.; Chamninok, P.; Pukird, S.; Chow, L.; Lupan, O.; Chai, G.; Khallaf, H.; Park, S.; Schulte, A. Effect of synthesis conditions on the growth of ZnO nanorods via hydrothermal method. *Physica. B* 2008, 403, 3713-3717.

- [78]. Lu, M. P.; Song, J.; Lu, M. Y.; Chen, M. T.; Gao, Y.; Chen, L. J.; Wang, Z. L. Piezoelectric Nanogenerator Using p-Type ZnO Nanowire Arrays. *Nano Lett.* 2009, 9, 1223-1227.
- [79]. Zhu, G.; Wang, A. C.; Liu, Y.; Zhou, Y. S.; Wang, Z. L. Functional Electrical Stimulation by Nanogenerator with 58 V Output Voltage. *Nano Lett.* 2012, 12, 3086-3090.
- [80]. Arnold, M. S.; Avouris, P.; Pan, Z. W.; Wang, Z. L. Field-effect transistors based on single semiconducting oxide nanobelts. *J. Phys. Chem. B* 2003, 107, 659-663.
- [81]. Fan, Z. Y.; Lu, J. G. Electrical properties of ZnO nanowire-field effect transistors characterized with scanning probes. *Appl. Phys. Lett.* 2005, 86, 032111.
- [82]. He, J. H.; Hsin, C. L.; Liu, J.; Chen, L. J.; Wang, Z. L. Piezoelectric gated diode of a single ZnO nanowire. *Adv. Mater.* 2007, 19, 781-784.
- [83]. Lu, C. Y.; Chang, S. P.; Chang, S. J.; Hsueh, T. J.; Hsu, C. L.; Chiou, Y. Z.; Chen, C. ZnO Nanowire-Based Oxygen Gas Sensor. *IEEE Sens. J.* 2009, 9, 485-489.
- [84]. Sakurai, M.; Wang, Y. G.; Uemura, T.; Aono, M. Electrical properties of individual ZnO nanowires. *Nanotechnology* 2009, 20, 155203.
- [85]. Liu, C. H.; Yiu, W. C.; Au, F. C. K.; Ding, J. X.; Lee, C. S.; Lee, S. T. Electrical properties of zinc oxide nanowires and intramolecular p-n junctions. *Appl. Phys. Lett.* 2003, 83, 3168-3170.
- [86]. Chiu, S. P.; Lin, Y. H.; Lin, J. J. Electrical conduction mechanisms in natively doped ZnO nanowires. *Nanotechnology* 2009, 20, 015203.
- [87]. Lin, X.; He, X. B.; Yang, T. Z.; Guo, W.; Shi, D. X.; Gao, H. J.; Ma, D. D. D.; Lee, S. T.; Liu, F.; Xie, X. C. Intrinsic current-voltage properties of nanowires with four-probe scanning tunneling microscopy: A conductance transition of ZnO nanowire. *Appl. Phys. Lett.* 2006, 89, 043103.
- [88]. Liao, L.; Zhang, Z.; Yang, Y.; Yan, B.; Cao, H. T.; Chen, L. L.; Li, G. P.; Wu, T.; Shen, Z. X.; Tay, B. K.; Yu, T.; Sun, X. W. Tunable transport properties of n-type ZnO nanowires by Ti plasma immersion ion implantation. *J. Appl. Phys.* 2008, 104, 076104.
- [89]. Zhang, Z. Y.; Jin, C. H.; Liang, X. L.; Chen, Q.; Peng, L. M. Current-voltage characteristics and parameter retrieval of semiconducting nanowires. *Appl. Phys. Lett.* 2006, 89, 073102.
- [90]. Wang, S. J.; Cheng, G.; Cheng, K.; Jiang, X. H.; Du, Z. L. The current image of single SnO<sub>2</sub> nanobelt nanodevice studied by conductive atomic force microscopy. *Nanoscale Res. Lett.* 2011, 6, 541.

- [91]. Navas, D.; Asenjo, A.; Jaafar, M.; Pirota, K. R.; Hernandez-Velez, M.; Sanz, R.; Lee, W.; Niesch, K.; Batallan, F.; Vazquez, M. Magnetic behavior of NixFe(100-x) ( $65 \leq x \leq 100$ ) nanowire arrays. *J. Magn. Magn. Mater.* 2005, 290, 191-194.
- [92]. Zhao, M. H.; Wang, Z. L.; Mao, S. X. Piezoelectric characterization of individual zinc oxide nanobelt probed by piezoresponse force microscope. *Nano Lett.* 2004, 4, 587-590.
- [93]. Li, M.; Su, Y. J.; Chu, W. Y.; Qiao, L. J.; Volinsky, A. A.; Kravchenko, G. Local piezoelectric effect on single crystal ZnO microbelt transverse I-V characteristics. *Appl. Phys. Lett.* 2011, 98, 082105.
- [94]. Chen, Y. Q.; Jiang, J.; He, Z. Y.; Su, Y.; Cai, D.; Chen, L. Growth mechanism and characterization of ZnO microbelts and self-assembled. *Mater. Lett.* 2005, 59, 3280-3283.
- [95]. Asthana, A.; Momeni, K.; Prasad, A.; Yap, Y. K.; Yassar, R. S. In situ probing of electromechanical properties of an individual ZnO nanobelt. *Appl. Phys. Lett.* 2009, 95, 172106.
- [96]. Ding, Y.; Wang, Z. L. Structure analysis of nanowires and nanobelts by transmission electron microscopy. *J. Phys. Chem. B* 2004, 108, 12280-12291.
- [97]. Wang, W. Z.; Zeng, B. Q.; Yang, J.; Poudel, B.; Huang, J. Y.; Naughton, M. J.; Ren, Z. F. Aligned ultralong ZnO nanobelts and their enhanced field emission. *Adv. Mater.* 2006, 18, 3275-3278.
- [98]. Hu, Y. F.; Gao, Y. F.; Singamaneni, S.; Tsukruk, V. V.; Wang, Z. L. Converse Piezoelectric Effect Induced Transverse Deflection of a Free-Standing ZnO Microbelt. *Nano Lett.* 2009, 9, 2661-2665.
- [99]. Lucas, M.; Wang, Z. L.; Riedo, E. Growth direction and morphology of ZnO nanobelts revealed by combining in situ atomic force microscopy and polarized Raman spectroscopy. *Phys. Rev. B* 2010, 81, 045415.
- [100]. Gao, Z. Y.; Zhou, J.; Gu, Y. D.; Fei, P.; Hao, Y.; Bao, G.; Wang, Z. L. Effects of piezoelectric potential on the transport characteristics of metal-ZnO nanowire-metal field effect transistor. *J. Appl. Phys.* 2009, 105, 113707.
- [101]. Yu, J.; Ippolito, S. J.; Wlodarski, W.; Strano, M.; Kalantar-Zadeh, K. Nanorod based Schottky contact gas sensors in reversed bias condition. *Nanotechnology* 2010, 21, 265502.
- [102]. Schroder, D. K. Semiconductor Material and Device Characterization, 3rd Ed., John Wiley & Sons, Inc., Hoboken, New Jersey 2006, Ch. 3.
- [103]. Lee, M. S.; Kim, T. Y.; Kim, D. Anisotropic electrical conductivity of delafossite-type CuAlO<sub>2</sub> laminar crystal. *Appl. Phys. Lett.* 2001, 79, 2028-2030.

- [104]. Dingreville, R.; Qu, J. M.; Cherkaoui, M. Surface free energy and its effect on the elastic behavior of nano-sized particles, wires and films. *J. Mech. Phys. Solids*. 2005, 53, 1827-1854.
- [105]. Brillson, L. J.; Lu, Y. C. ZnO Schottky barriers and Ohmic contacts. *J. Appl. Phys.* 2011, 109, 121301.
- [106]. Song, J. H.; Zhou, J.; Wang, Z. L. Piezoelectric and semiconducting coupled power generating process of a single ZnO belt/wire. A technology for harvesting electricity from the environment. *Nano Lett.* 2006, 6, 1656-1662.
- [107]. Kaga, H.; Kinemuchi, Y.; Yihnaz, H.; Watarl, K.; Nakano, H.; Nakano, H.; Tanaka, S.; Makiya, A.; Kato, Z.; Uernatsu, K. Orientation dependence of transport property and microstructural characterization of Al-doped ZnO ceramics. *Acta. Mater.* 2007, 55, 4753-4757.
- [108]. Wu, Y. F.; Yu, N. S.; Liu, D. P.; He, Y. Y.; Liu, Y. D.; Liang, H. W.; Du, G. T. Electrical anisotropy properties of ZnO nanorods analyzed by conductive atomic force microscopy. *Appl. Surf. Sci.* 2013, 265, 176-179.
- [109]. Luo, L.; Zhang, Y. F.; Mao, S. S.; Lin, L. W. Fabrication and characterization of ZnO nanowires based UV photodiodes. *Sens. Actuators, A* 2006, 127, 201-206.
- [110]. Wang, Z. L. ZnO nanowire and nanobelt platform for nanotechnology. *Mater. Sci. Eng. R* 2009, 64, 33-71.
- [111]. Goldberger, J.; Sirbully, D. J.; Law, M.; Yang, P. ZnO nanowire transistors. *J. Phys. Chem. B* 2005, 109, 9-14.
- [112]. Wan, Q.; Li, Q. H.; Chen, Y. J.; Wang, T. H.; He, X. L.; Li, J. P.; Lin, C. L. Fabrication and ethanol sensing characteristics of ZnO nanowire gas sensors. *Appl. Phys. Lett.* 2004, 84, 3654-3656.
- [113]. Jiang, C. M.; Tang, C. L.; Song, J. H. The Smallest Resonator Arrays in Atmosphere by Chip-Size-Grown Nanowires with Tunable Q-factor and Frequency for Subnanometer Thickness Detection. *Nano Lett.* 2015, 15, 1128-1134.
- [114]. Zhang, F.; Niu, S. M.; Guo, W. X.; Zhu, G.; Liu, Y.; Zhang, X. L.; Wang, Z. L. Piezophotronic Effect Enhanced Visible/UV Photodetector of a Carbon-Fiber/ZnO-CdS Double-Shell Microwire. *ACS Nano* 2013, 7, 4537-4544.
- [115]. Soci, C.; Zhang, A.; Xiang, B.; Dayeh, S. A.; Aplin, D. P. R.; Park, J.; Bao, X. Y.; Lo, Y. H.; Wang, D. ZnO nanowire UV photodetectors with high internal gain. *Nano Lett.* 2007, 7, 1003-1009.
- [116]. Lu, C. Y.; Chang, S. J.; Chang, S. P.; Lee, C. T.; Kuo, C. F.; Chang, H. M.; Chiou, Y. Z.; Hsu, C. L.; Chen, I. C. Ultraviolet photodetectors with ZnO nanowires prepared on ZnO : Ga/glass templates. *Appl. Phys. Lett.* 2006, 89, 153101.

- [117]. Yang, Q.; Guo, X.; Wang, W. H.; Zhang, Y.; Xu, S.; Lien, D. H.; Wang, Z. L. Enhancing Sensitivity of a Single ZnO Micro-/Nanowire Photodetector by Piezo-phototronic Effect. *ACS Nano* 2010, 4, 6285-6291.
- [118]. Hatch, S. M.; Briscoe, J.; Dunn, S. A Self-Powered ZnO-Nanorod/CuSCN UV Photodetector Exhibiting Rapid Response. *Adv. Mater.* 2013, 25, 867-871.
- [119]. Zhang, T. C.; Guo, Y.; Mei, Z. X.; Gu, C. Z.; Du, X. L. Visible-blind ultraviolet photodetector based on double heterojunction of n-ZnO/insulator-MgO/p-Si. *Appl. Phys. Lett.* 2009, 94, 113508.
- [120]. Takahashi, Y.; Kanamori, M.; Kondoh, A.; Minoura, H.; Ohya, Y. Photoconductivity of Ultrathin Zinc-Oxide Films. *Jpn. J. Appl. Phys. Lett.* 1994, 33, 6611-6615.
- [121]. Jin, Y.; Wang, J.; Sun, B.; Blakesley, J. C.; Greenham, N. C. Solution-Processed Ultraviolet Photodetectors Based on Colloidal ZnO Nanoparticles. *Nano Lett.* 2008, 8, 1649-1653.
- [122]. Shin, J. H.; Lee, J. S.; Hwang, C. S.; Park, S. H. K.; Cheong, W. S.; Ryu, M.; Byun, C. W.; Lee, J. I.; Chu, H. Y. Light Effects on the Bias Stability of Transparent ZnO Thin Film Transistors. *Etri. J.* 2009, 31, 62-64.
- [123]. Kurbanov, S. S.; Panin, G. N.; Kim, T. W.; Kang, T. W. Impact of visible light illumination on ultraviolet emission from ZnO nanocrystals. *Phys. Rev. B* 2008, 78, 045311.
- [124]. Jiang, C. M.; Song, J. H. An Ultrahigh-Resolution Digital Image Sensor with Pixel Size of 50 nm by Vertical Nanorod Arrays. *Adv. Mater.* 2015, 27, 4454-4460.
- [125]. Tang, C. L.; Jiang, C. M.; Bi, S.; Song, J. H. Photoelectric property modulation by nanoconfinement in the longitude direction of short semiconducting nanorods. *ACS Appl. Mater. Interfaces* 2016, 8, 11001-11007.
- [126]. Greene, L. E.; Law, M.; Goldberger, J.; Kim, F.; Johnson, J. C.; Zhang, Y. F.; Saykally, R. J.; Yang, P. D. Low-temperature wafer-scale production of ZnO nanowire arrays. *Angew. Chem. Int. Ed.* 2003, 42, 3031-3034.
- [127]. Dai, J.; Xu, C. X.; Xu, X. Y.; Guo, J. Y.; Li, J. T.; Zhu, G. Y.; Lin, Y. Single ZnO Microrod Ultraviolet Photodetector with High Photocurrent Gain. *ACS Appl. Mater. Interfaces* 2013, 5, 9344-9348.
- [128]. Bao, J. M.; Shalish, I.; Su, Z. H.; Gurwitz, R.; Capasso, F.; Wang, X. W.; Ren, Z. F. Photoinduced oxygen release and persistent photoconductivity in ZnO nanowires. *Nanoscale Res. Lett.* 2011, 6, 404.
- [129]. Koscheev, S. V.; Cherkashin, A. E. Variation of the Surface-Potential of Zinc-Oxide under Illumination. *React. Kinet. Catal. Lett.* 1980, 14, 129-134.

- [130]. Maragliano, C.; Lilliu, S.; Dahlem, M. S.; Chiesa, M.; Souier, T.; Stefancich, M. Quantifying charge carrier concentration in ZnO thin films by Scanning Kelvin Probe Microscopy. *Sci. Rep.* 2014, 4, 4203.
- [131]. Wang, Z. Z.; Gu, Y. S.; Qi, J. J.; Lu, S. N.; Li, P. F.; Lin, P.; Zhang, Y. Size dependence and UV irradiation tuning of the surface potential in single conical ZnO nanowires. *RSC Adv.* 2015, 5, 42075-42080.
- [132]. Razeghi, M.; Rogalski, A. Semiconductor ultraviolet detectors. *J. Appl. Phys.* 1996, 79, 7433-7473.
- [133]. Liu, K. W.; Sakurai, M.; Aono, M. ZnO-Based Ultraviolet Photodetectors. *Sensors* 2010, 10, 8604-8634.
- [134]. Chang, P. C.; Chien, C. J.; Stichtenoth, D.; Ronning, C.; Lu, J. G. Finite size effect in ZnO nanowires. *Appl. Phys. Lett.* 2007, 90, 113101.
- [135]. Ko, Y. H.; Nagaraju, G.; Yu, J. S. Fabrication and Optimization of Vertically Aligned ZnO Nanorod Array-Based UV Photodetectors via Selective Hydrothermal Synthesis. *Nanoscale Res. Lett.* 2015, 10, 323.
- [136]. Fonoberov, V. A.; Alim, K. A.; Balandin, A. A.; Xiu, F. X.; Liu, J. L. Photoluminescence investigation of the carrier recombination processes in ZnO quantum dots and nanocrystals. *Phys. Rev. B* 2006, 73, 165317.
- [137]. Baxter, J. B.; Schmuttenmaer, C. A. Conductivity of ZnO nanowires, nanoparticles, and thin films using time-resolved terahertz spectroscopy. *J. Phys. Chem. B* 2006, 110, 25229-25239.
- [138]. Kirkby, D. R. Picosecond optoelectronic cross correlator using a gain modulated avalanche photodiode for measuring the impulse response of tissue. Ph.D. Thesis, University College London, London, England, 1999.
- [139]. Burr, G. W.; Kurdi, B. N.; Scott, J. C.; Lam, C. H.; Gopalakrishnan, K.; Shenoy, R. S. Overview of candidate device technologies for storage-class memory. *IBM J. Res. Dev.* 2008, 52, 449-464.
- [140]. Strachan, J. P.; Strukov, D. B.; Borghetti, J.; Yang, J. J.; Medeiros-Ribeiro, G.; Williams, R. S. The switching location of a bipolar memristor: chemical, thermal and structural mapping. *Nanotechnology* 2011, 22, 254015.
- [141]. Son, D.; Lee, J.; Qiao, S.; Ghaffari, R.; Kim, J.; Lee, J. E.; Song, C.; Kim, S. J.; Lee, D. J.; Jun, S. W.; Yang, S.; Park, M.; Shin, J.; Do, K.; Lee, M.; Kang, K.; Hwang, C. S.; Lu, N. S.; Hyeon, T.; Kim, D. H. Multifunctional wearable devices for diagnosis and therapy of movement disorders. *Nat. Nanotechnol.* 2014, 9, 397-404.
- [142]. Reeder, J.; Kaltenbrunner, M.; Ware, T.; Arreaga-Salas, D.; Avendano-Bolivar, A.; Yokota, T.; Inoue, Y.; Sekino, M.; Voit, W.; Sekitani, T.; Someya, T. Mechanically

- Adaptive Organic Transistors for Implantable Electronics. *Adv. Mater.* 2014, 26, 4967-4973.
- [143]. Baek, S.; Lee, D.; Kim, J.; Hong, S. H.; Kim, O.; Ree, M. Novel digital nonvolatile memory devices based on semiconducting polymer thin films. *Adv. Funct. Mater.* 2007, 17, 2637-2644.
- [144]. Hahm, S. G.; Choi, S.; Hong, S. H.; Lee, T. J.; Park, S.; Kim, D. M.; Kwon, W. S.; Kim, K.; Kim, O.; Ree, M. Novel Rewritable, Non-volatile Memory Devices Based on Thermally and Dimensionally Stable Polyimide Thin Films. *Adv. Funct. Mater.* 2008, 18, 3276-3282.
- [145]. Kim, G. H.; Lee, J. H.; Ahn, Y.; Jeon, W.; Song, S. J.; Seok, J. Y.; Yoon, J. H.; Yoon, K. J.; Park, T. J.; Hwang, C. S. 32 x 32 Crossbar Array Resistive Memory Composed of a Stacked Schottky Diode and Unipolar Resistive Memory. *Adv. Funct. Mater.* 2013, 23, 1440-1449.
- [146]. Nagashima, K.; Yanagida, T.; Oka, K.; Kanai, M.; Klamchuen, A.; Kim, J. S.; Park, B. H.; Kawai, T. Intrinsic Mechanisms of Memristive Switching. *Nano Lett.* 2011, 11, 2114-2118.
- [147]. Yang, Y. C.; Pan, F.; Liu, Q.; Liu, M.; Zeng, F. Fully Room-Temperature-Fabricated Nonvolatile Resistive Memory for Ultrafast and High-Density Memory Application. *Nano Lett.* 2009, 9, 1636-1643.
- [148]. Son, D. I.; Kim, T. W.; Shim, J. H.; Jung, J. H.; Lee, D. U.; Lee, J. M.; Il Park, W.; Choi, W. K. Flexible Organic Bistable Devices Based on Graphene Embedded in an Insulating Poly(methyl methacrylate) Polymer Layer. *Nano Lett.* 2010, 10, 2441-2447.
- [149]. Song, S.; Cho, B.; Kim, T. W.; Ji, Y.; Jo, M.; Wang, G.; Choe, M.; Kahng, Y. H.; Hwang, H.; Lee, T. Three-Dimensional Integration of Organic Resistive Memory Devices. *Adv. Mater.* 2010, 22, 5048-5052.
- [150]. Karthik, K. R. G.; Prabhakar, R. R.; Hai, L.; Batabyal, S. K.; Huang, Y. Z.; Mhaisalkar, S. G. A ZnO nanowire resistive switch. *Appl. Phys. Lett.* 2013, 103, 123114.
- [151]. Meister, S.; Schoen, D. T.; Topinka, M. A.; Minor, A. M.; Cui, Y. Void Formation Induced Electrical Switching in Phase-Change Nanowires. *Nano Lett.* 2008, 8, 4562-4567.
- [152]. Park, J.; Lee, S.; Lee, J.; Yong, K. A Light Incident Angle Switchable ZnO Nanorod Memristor: Reversible Switching Behavior Between Two Non-Volatile Memory Devices. *Adv. Mater.* 2013, 25, 6423-6429.
- [153]. Yao, J.; Jin, Z.; Zhong, L.; Natelson, D.; Tour, J. M. Two-Terminal Nonvolatile Memories Based on Single-Walled Carbon Nanotubes. *ACS Nano* 2009, 3, 4122-4126.

- [154]. Sohn, J. I.; Choi, S. S.; Morris, S. M.; Bendall, J. S.; Coles, H. J.; Hong, W. K.; Jo, G.; Lee, T.; Welland, M. E. Novel Nonvolatile Memory with Multibit Storage Based on a ZnO Nanowire Transistor. *Nano Lett.* 2010, 10, 4316-4320.